THE UNIVERSITY OF CHICAGO

QUANTUM MATERIALS AND MULTIMODE PHOTONICS IN TWISTED OPTICAL CAVITIES

A DISSERTATION SUBMITTED TO
THE FACULTY OF THE DIVISION OF THE PHYSICAL SCIENCES
IN CANDIDACY FOR THE DEGREE OF
DOCTOR OF PHILOSOPHY

DEPARTMENT OF PHYSICS

BY
CLAIRE BAUM

CHICAGO, ILLINOIS
DECEMBER 2022

Dedicated to family, friends, and you, the reader!

TABLE OF CONTENTS

LIST OF FIGURES

LIST OF TABLES

ACKNOWLEDGMENTS

My first inkling of wanting to join the Simon Lab before I became a graduate student was while scrolling through the University of Chicago physics faculty online. Jon was the only faculty member wearing sunglasses in his department photo, and I remembered thinking "yeah, the Simon Lab seems like it would be the right vibe for me." It has been wonderful being advised by Jon as a member of the Simon Lab. There is no one quite like Jon—I have consistently been amazed at his creativity, actively supportive attitude, storytelling, practical approaches to science, and genuine care for his students. Jon challenged me, contributing greatly to my growth as both a person and a scientist.

My early years in the Simon Lab were spent primarily with Jia Ningyuan, Nathan Schine, and our postdoc Logan Clark in the multimode polariton lab. All three of these individuals are fantastic scientists and supported me in learning the ins and outs of our complex experiment. Jia's dedication, Nathan's deep creativity and clarity, and Logan's ability to somehow accomplish great feats in short amounts of time have all been tremendous scientific assets for the experiment and are qualities I've personally looked up to. Later on, Lukas Palm and our postdoc Matt Jaffe joined the group. They have been an absolute pleasure to work with and have really pushed the experiment to the next level. Lukas is simultaneously fearless and the life of the party in the lab—I think he is the only person I've known to casually make extraordinarily useful modifications to an experiment while referencing meme culture and playing throwback tunes. Matt Jaffe is an absolute machine. I'm amazed by his boundless efficiency and ability to clearly explain concepts in fun, intuitive, and precise ways seemingly effortlessly. Both Lukas and Matt are creative schemers, and the experiment and I have benefited hugely from their imaginative ideas, hard work, and care.

The Simon Lab as a whole has been full of brilliant, wonderful people who have helped me, taught me new things, challenged me, and given me some darn good laughs. In the hybrid quantum experiment next door, Lavanya Taneja is one of the deepest thinkers I know,

an excellent teacher, and a fantastic experimentalist. Her questions often spark ideas that had never even occurred to me. Our postdoc, Ash Kumar, is extremely hardworking and a similarly fantastic experimentalist. I've deeply appreciated his willingness to be my sounding board and also indulge in a questionably healthy amount of Starbucks with me. Our former graduate students Aziza Suleymanzade and Mark Stone were both immensely knowledgeable, helpful, and well-spoken. Chuan Yin has been blazing a trail in the load-lock experiment. I am so impressed at her ability to rapidly learn and and build a whole new experiment from the ground up. Danial Shadmany has joined Chuan in the load-lock experiment, and I am similarly impressed at his ability to learn about and implement crazy new cavity designs, particularly among the chaos of traveling back and forth across the country. I extend my additional deep thanks to Alex Georgakopoulos, Clai Owens, Tian-Xing Zheng, Alex Ma, Brendan Saxberg, Meg Panetta, Gabrielle Roberts, Andrei Vrajitoarea, Henry Ando, and our undergraduates Jasmine Kalia, Evan Mata, Carl Padgett, Joshua Wakefield, Lin Su, and Tingran Wang for making my experience in the Simon Lab so positive and educational.

The JFI staff have also been immensely helpful during my graduate experience. Our former and current building manager, John Phillips and Bentley Wall, have been so on the ball and friendly. Maria Jimenez has been the master of Simon Lab logistics, and has played an active role in making sure JFI events run smoothly along with Brenda Thomas. Luigi Mazzenga taught me invaluable machine shop skills and was always at the ready for any problem you threw at him. Additionally, Justin Jureller and the MRSEC facilities have been incredibly useful assets for making custom components.

Lastly, I thank my growing family—Jim, Jamil, Krista, Mark, Avery, Diane, Davis, and Maddie—and friends for their unconditional support, love, and fun.

ABSTRACT

In order to put novel condensed matter physics theories to the test, we turn to simulations and experiments. However, computer simulation is not always feasible due to inherent computational obstructions or the demand for excessive computational resources to calculate the dynamics of many particles, for example. Where computer simulators fail, we turn to "quantum simulators," or experimental model systems. Within these poke-able model systems, we need only set up the experimental conditions that mirrors the physics of interest, then glean information based on measurable quantities of the system. Examples of quantum simulation platforms include trapped ions, cold atoms in optical lattices, superconducting circuits, nitrogen-vacancy centers, and interacting photons in optical cavities—the platform of the work presented in this thesis.

This thesis describes the quantum simulation of topologically ordered quantum materials made of light using a twisted optical cavity and Rydberg polaritons. This platform—based in atoms and cavities—additionally enables studies based in the manipulation of atoms using light, leading to the optical mode conversion of photons at high efficiency. The work presented in this thesis provides broad prospects for the study of topologically-ordered states and spatiotemporal modulation of optical susceptibility as a tool for quantum information as well as atomic, molecular, and optical (AMO) systems.

CHAPTER 1

INTRODUCTION

1.1 What is a quantum material?

What are materials, fundamentally? In general, we think about materials as a collection of interacting particles that are described by some sort of order. In many cases, this order is well described by Landau's theory of phase transitions as we will discuss in Chapter 5, but not always. In the case of quantum materials—which are materials that are fundamentally quantum mechanical—the concept of topological order [1] arises, violating Landau's theory. Intuitively, topological order can be thought of as "dancing patterns" of long-range quantum entanglement [2], yielding strong correlations between particles and exotic properties that may be potentially harnessed for fault-tolerant quantum computation [3] and studied to understand and predict new phases of matter.

To me, I also often think of "topological" as meaning "insensitive to perturbations." In the stereotypical example of topology, a coffee cup is topologically equivalent to a donut. Perturb the donut to become a coffee cup, and really it's *still* a donut. Topological materials are "robust" in this sense. As a more concrete example, topological materials can host edge modes [4], or modes that are physically confined to the system edge. Upon perturbing the geometry of the edge, these edge modes *still* exist and are thus insensitive to the perturbation.

In order to fully realize the potential of topologically ordered quantum materials, we need to better understand topological order. To date, topological order has been primarily studied in electronic systems like graphene [5]. However, these systems can be quite difficult to probe and control on an individual particle level. In order to answer open questions regarding topics such as transitions between topological phases and discovering materials the exhibit different topological orders, we experimentalists seek platforms for simulating particle interactions—or "quantum simulators"—from the ground up in a controlled, quantum

mechanical environment. By doing so, we aim to realize and study topologically ordered states using real, model systems.

1.2 Quantum materials made of light

Across atomic, molecular, and optical (AMO) physics, a pattern arises in the choices of experimental platforms used to create synthetic quantum materials: some particle is used, it has some interaction with other like-particles, and its dispersion is controlled by its environment. We already know electronic systems have been utilized, where electrons interact via the Coulomb force and an ionic lattice influences their dispersion. However, electronic systems often come in the form of a bulk material comprised of many interacting particles—not so ideal for individual particle control and tunability. Instead, we might utilize interacting superconducting qubits [6] or perhaps ultracold atoms [7] that interact through the electromagnetic force in an optical lattice, which looks like a periodic potential to the atoms. The platform of ultracold atoms has demonstrated some success at creating topologically ordered states [8], but in the Simon Lab we opt to use interacting *photons* and influence their dispersion using an optical cavity [9, 10].

But wait... photons don't interact?! Well, not *directly*. In the presence of atoms—with which photons *do* interact—photons can undergo effective interactions as we will discuss in Chapter 5. Additionally, if we track the motion of a photon bouncing back and forth between two curved cavity mirrors in a given transverse plane of the cavity, it appears to oscillate as a massive harmonic oscillator! The intuition behind this choice of platform is that photons can act like interacting, massive particles while maintaining their convenient, unique qualities of speed, direct detectability, and manipulability with common optical elements. With this platform, we ultimately aim to create and probe topologically ordered quantum materials made of light. That said, this platform offers additional, interesting opportunities for research as we will see in Chapter 6.

1.3 Thesis overview

This thesis is intended primarily for budding AMO graduate students and those generally interested in the research of the Simon Lab.

As our platform boils down to atoms in a cavity, we will spend some quality time discussing each of these components individually in Chapter 2.

In Chapter 3, we will theoretically combine atoms and cavities, working our way through dealing with Hamiltonians of increasingly complex atom-cavity systems.

Chapter 4 will discuss our experimental setup used in the research of Chapters 5 and 6.

Chapters 5 and 6 contain the main results of this thesis. Chapter 5 describes our efforts in creating topologically ordered quantum materials made of light—namely, Laughlin states—and how our next generation cavity should enable topological few-body physics. Chapter 6 describes how the same platform used in Chapter 5 can be used to convert photons from one mode of the cavity to another at high efficiency.

Finally, Chapter 7 provides a brief outlook on future work.

CHAPTER 2

ATOMS AND CAVITIES

2.1 Atoms

The first step in working with atoms is understanding atoms. This section details properties of atoms, namely alkali metal atoms, from both an isolated and interacting standpoint.

2.1.1 The lone alkali metal atom

For a single atom, our mission is typically to compute the electronic 1) energies, and 2) wavefunctions. Why? From the experimentalist viewpoint, this information is needed to compute relevant quantities such as transition strengths and informs experimental choices like what lasers to buy. If the energy difference between two atomic levels you'd like to couple is 780 nm, you had best buy a 780 nm laser. When calculating the energies and wavefunctions of a system in general, the standard practice is to write down the system's Hamiltonian and finds its eigenvalues (energies) and eigenfunctions (wavefunctions).[1] For an atom with one valence electron, as in hydrogen and the alkali metals, we typically think of the system Hamiltonian in three parts:

(1) The unperturbed Hamiltonian, $H_0 = T + V$

(2) The fine structure Hamiltonian, $H_{\text{fs}} \propto \mathbf{L} \cdot \mathbf{S}$

(3) The hyperfine structure Hamiltonian, $H_{\text{hfs}} \propto \mathbf{I} \cdot \mathbf{J}$

The eigenvalues of H_0 gives us our energies, which are then modified by doing perturbation theory for the small correction terms H_{fs} and H_{hfs} using our wavefunctions. In practice,

1. This process is *equivalent* to solving the time-independent Schrödinger equation, which is in essence an eigenvalue problem ($H\Psi = E\Psi$)!

the more complex structure of alkali metal atoms makes this process quite difficult and we often rely on empirical observations and numerical computations to provide us with energies and wavefunctions. Nevertheless, this subsection will take a look at Hamiltonians for single hydrogen-like (namely, alkali metal) atoms.

The unperturbed Hamiltonian

The unperturbed Hamiltonian for an atom that has N electrons and nuclear charge Ze is [11]

$$H_0 = T + V \tag{2.1}$$

$$= \sum_{i=1}^{N} \left(-\frac{\hbar^2}{2m}\nabla_i^2 - \frac{Ze^2}{4\pi\epsilon_0 r_i} + \sum_{j>i}^{N} \frac{e^2}{4\pi\epsilon_0 r_{ij}} \right) \tag{2.2}$$

where $r_{ij} = |\mathbf{r}_i - \mathbf{r}_j|$, with $\mathbf{r}_i$ the position if the i^{th} electron. The kinetic term (T) is accounted for by the leftmost term in Equation 2.2, whereas the potential term (V) is accounted for by the middle and rightmost terms. V includes Coulomb potential contributions from both the positively charged nucleus and the many electrons about it.

The form of Equation 2.2 is somewhat inconvenient to work with, but we can make some simplifications using the central field approximation, which makes the assumption that electrons move independently in a central potential that depends only on the radial distance of an electron from the atomic nucleus:

$$H_0 = \sum_{i=1}^{N} \left(-\frac{\hbar^2}{2m}\nabla_i^2 + V(r_i) \right) \tag{2.3}$$

Now, this Hamiltonian is effectively N copies of the same form which is considerably more manageable. However, what exactly is $V(r)$ for each electron? For an electron close to the nucleus, we know it should "see" much of the nuclear charge. For an electron far from the nucleus, we know it should "see" a charge e as the nuclear charge is screened by the

remaining electrons. An example of a model $V(r)$ and its charge distribution $Z(r)$ is given in atomic units by [12]:

$$V(r) = -\frac{Z(r)}{r} - \frac{\alpha_c}{2r^4}(1 - e^{-(r/r_c)^6}) \tag{2.4}$$

$$Z(r) = 1 + (Z-1)e^{-a_1 r} - r(a_3 + a_4 r)e^{-a_2 r} \tag{2.5}$$

where α_c is the static dipole polarizability of the positive-ion core, r_c is a cutoff radius, and constants a_i where $i \in \{1, 2, 3, 4\}$ are atom-dependent and orbital angular momentum l-dependent parameters. Note that for large r, $V(r)$ approaches the familiar $1/r$ Coulomb potential. For those interested in doing calculations with this model potential, numerical tools are your friend and the values for α_c, r_c, and all the a_i are listed in [12].

The fine structure Hamiltonian

The fine structure Hamiltonian arises from the interaction between the spin magnetic moment of an atom's electron, $\boldsymbol{\mu}_S$, and the magnetic field experienced by the electron as a result of its orbit about a charged environment. The fine structure Hamiltonian is [13]

$$H_{\text{fs}} = -\boldsymbol{\mu}_S \cdot \mathbf{B} \tag{2.6}$$

$$= -\left(-\frac{\mu_B g_S}{\hbar}\mathbf{S}\right) \cdot \left(\frac{1}{mc^2 er}\frac{\partial V(r)}{\partial r}\mathbf{L}\right) \tag{2.7}$$

$$= \frac{\mu_B g_S}{mc^2 \hbar e r}\frac{\partial V(r)}{\partial r}\mathbf{L} \cdot \mathbf{S} \tag{2.8}$$

where $\mu_B = e\hbar/2m_e$ is the Bohr magneton, $g_S \approx 2$ is the electron g-factor, and $m = m_e m_n/(m_e + m_n)$ is the reduced mass (m_e is the mass of an electron, m_n is the mass of the nucleus of the atom in question). The expression for H_{fs} above excludes Thomas precession, a relativistic effect, which can be accounted for by replacing g_S with $g_S - 1$:

$$H_{\text{fs}} = \frac{\mu_B(g_S - 1)}{mc^2\hbar er}\frac{\partial V(r)}{\partial r}\mathbf{L}\cdot\mathbf{S} \tag{2.9}$$

$$\approx \frac{1}{2m^2c^2r}\frac{\partial V(r)}{\partial r}\mathbf{L}\cdot\mathbf{S} \tag{2.10}$$

Now Equation 2.10 is our fine structure Hamiltonian. In actuality, this Hamiltonian is still missing a term (the Darwin term), but we will stop here with just the spin-orbit contribution. In working with this Hamiltonian, you may find use of a simplified $V(r)$ from that in Equation 2.4 depending on your goal. For example, if computing the energy of high n and l level, the valence electron is far from the nucleus and "sees" a $1/r$ potential, which is considerably more simple to work with.

The hyperfine Hamiltonian

The hyperfine structure Hamiltonian arises from a similar $-\boldsymbol{\mu}\cdot\mathbf{B}$ interaction, except now we consider the interaction of the nuclear magnetic moment, $\boldsymbol{\mu}_I$, with the magnetic field generated by the electrons about the nucleus [13]:

$$H_{\text{hfs}} = -\boldsymbol{\mu}_I\cdot\mathbf{B} \tag{2.11}$$

$$= -\left(-\frac{\mu_B g_I}{\hbar}\mathbf{I}\right)\cdot(-b\mathbf{J}) \tag{2.12}$$

$$= \frac{A_{\text{hfs}}}{\hbar^2}\mathbf{I}\cdot\mathbf{J} \tag{2.13}$$

where A_{hfs} = magnetic dipole hyperfine constant. To slightly higher order including the electric quadrupole constant, B_{hfs},

$$H_{\text{hfs}} = \frac{A_{\text{hfs}}}{\hbar^2}\mathbf{I}\cdot\mathbf{J} + B_{\text{hfs}}\frac{\frac{3}{\hbar^2}(\mathbf{I}\cdot\mathbf{J})^2 + \frac{3}{2\hbar}(\mathbf{I}\cdot\mathbf{J}) - I(I+1)J(J+1)}{2I(2I-1)J(2J-1)} \tag{2.14}$$

Typically, constants A_{hfs} and B_{hfs} are measured experimentally.

Finding the energies and wavefunctions

So how do we acquire atomic energies and wavefunctions, specifically for alkali metal atoms? There are several paths:

(1) **Do it yourself from the bottom up.** By "the bottom up," I mean starting from a theoretical foundation. In other words, solve the Schrödinger equation numerically using the Hamiltonian(s) in this subsection with your favorite program.[2]

(2) **Do it yourself from the top down.** By "the top down," I mean starting from empirical formulae that do a pretty good job of approximation. This path is particularly useful for calculating the transition frequency between two atomic Rydberg levels ($n \gtrapprox 10$), for example, where hyperfine energy corrections matter less because the electron is, on average, further from the nucleus. One such empirical formula is a slightly modified Bohr formula with quantum defect δ_l,

$$E_0(n,l) = -\frac{\text{Ry}}{(n-\delta_l)^2} \tag{2.15}$$

where the mass-corrected Rydberg constant, Ry, is

$$\text{Ry} = \frac{1}{2}\frac{e^4 m_e m_n}{16\pi^2\epsilon_0^2\hbar^2(m_e+m_n)} \tag{2.16}$$

Equation 2.15 approximates the energy levels of alkali metal atoms using an empirical "fudge factor," δ_l, which is an actual number you should look up. You should think of $n-\delta_l$ as an effective principle quantum number. For $l \geq 3$, $\delta_l \approx 0$ as the electron wavefunction has most of it amplitude located outside the atomic core. Thus, most of

2. Reference [11] contains additional information about solving the Schrödinger equation numerically, including an exercise where the numerical solution is carried out using a spreadsheet!

the time the electron "sees" the core as a single proton, thereby reducing the energy formula to the hydrogen case. Another such formula is the Landé formula [14] for the fine structure energy corrections to $E_0(n, l)$,

$$\Delta E_{\text{fs}} = \frac{Z_i^2 Z_o^2}{(n - \delta_l)^3 l(l+1)} \alpha^2 \text{Ry} \tag{2.17}$$

where $\alpha = (e^2/4\pi\epsilon_0)/\hbar c \approx 1/137$ is the fine structure constant, Z_i is the "inner" atomic number for an electron close to the nucleus (Z), and Z_o is the "outer" atomic number for an electron far from the nucleus (1, for alkali metal atoms).

(3) **Look it up.** Literally, use Google. These resources have been tremendously helpful:

- **Alkali D Line Data**:
  https://steck.us/alkalidata/
- **ARC (Alkali.ne Rydberg Calculator)**:
  https://github.com/nikolasibalic/ARC-Alkali-Rydberg-Calculator

2.1.2 Atom-atom interactions

Generally speaking, two neutral atoms interact rather weakly when they are both in their ground states because each atom "sees" the other as, well, neutral, and neutral particles do not directly experience a Coulomb force. Neutral atoms may experience dipole-dipole forces, but for two neutral atoms in their ground states, the size of their dipoles is small compared to typical atomic separations and thus these dipolar forces are weak. In the ground state, electrons are separated from the nucleus by sub-nanometer length scales. This length scale is a fraction of the distances between atoms of a typical trapped gas. A high trapped gas density of 10^{14} atoms per cubic centimeter corresponds to a few hundreds of nanometers separation between atoms, still much larger than the electron-nucleus separation and hence why neutral ground state atoms are weakly interacting.

However, interactions between excited atoms are perhaps a bit more interesting. In an excited atom, the valence electron orbit is considerably further from the nucleus. In the presence of another excited atom, both atoms' valence electrons can now "see" a distinction between the other atoms' negatively charged valence electron and positively charge core as a result of the distant valence electron orbit from the nucleus, giving rise to stronger dipolar interactions between atoms.

This subsection will briefly overview the interactions between Rydberg atoms, where the principle quantum number $n \gtrapprox 10$, and the two primary interactions in the short range and long range limiting cases [15]:

(1) The resonant dipole-dipole interaction $\propto 1/R^3$ (short range)

(2) The van der Waals interaction $\propto 1/R^6$ (long range)

Pair state energies

Two atoms located at $\mathbf{R}_1$ and $\mathbf{R}_2$ interact via the dipole-dipole interaction [16, 17]:

$$V(\mathbf{R}) = \frac{1}{4\pi\epsilon_0}\left(\frac{\mathbf{d}_1 \cdot \mathbf{d}_2 - 3(\mathbf{d}_1 \cdot \mathbf{n})(\mathbf{d}_2 \cdot \mathbf{n})}{R^3}\right) \tag{2.18}$$

where $\mathbf{d}_i$ is the dipole matrix element for the first atom ($i = 1$) for some Rydberg to Rydberg state transition $|r_1\rangle \rightarrow |r_{1'}\rangle$ and second atom ($i = 2$) for some Rydberg to Rydberg state transition $|r_2\rangle \rightarrow |r_{2'}\rangle$, $\mathbf{R} = \mathbf{R}_2 - \mathbf{R}_1$, and $\mathbf{n} = \mathbf{R}/R$.

We know the Rydberg state energies for *individual* atoms from the previous subsection, but now we'd like to know: what is the energy for *pairs* of Rydberg atoms? Let's say the energy for some generic Rydberg state $|r\rangle$ is E_r for an individual atom. In the absence of dipole-dipole interactions, we call two of these Rydberg atoms a *pair state* $|r\rangle \otimes |r\rangle = |rr\rangle$ with energy $E_r + E_r = 2E_r$. Just to rephrase the previous sentence slightly more overtly, *pair states are defined in the absence of atom-atom (i.e. dipole-dipole) interactions.* As

soon as we include the dipole-dipole interaction from Equation 2.18 in our calculations, we perturb the pair states. The resulting eigenstates actually become admixtures of pair states, and the resulting eigenenergies deviate from the initial pair state energies. Only if our two atoms are sufficiently far apart do the eigenstates and eigenenergies approach pair states whose energies are the sum of individual Rydberg state energies, and this is because the dipole-dipole interaction goes to zero with large R meaning the atoms no longer interact!

So how do we calculate the eigenstates and eigenenergies of two Rydberg atoms shoved together? Let's revisit the parameters defined shortly after Equation 2.18. Let the energies for the individual atom Rydberg states $|r_1\rangle$, $|r_{1'}\rangle$, $|r_2\rangle$, and $|r_{2'}\rangle$ be E_1, $E_{1'}$, E_2, and $E_{2'}$, respectively. Since we are considering the $|r_1\rangle \rightarrow |r_{1'}\rangle$ transition for the first atom and the $|r_2\rangle \rightarrow |r_{2'}\rangle$ for the second atom, this means we ought to consider the pair states $|r_1 r_2\rangle$ with energy $E_1 + E_2$ and $|r_{1'} r_{2'}\rangle$ with energy $E_{1'} + E_{2'}$. We can find how $V(\mathbf{R})$ mixes this pair states by solving for the eigenvalues and eigenvectors of the Hamiltonian [18]

$$H = \begin{pmatrix} 0 & V(\mathbf{R}) \\ V(\mathbf{R}) & \Delta \end{pmatrix} \tag{2.19}$$

where Δ is called the "energy defect" [19] and is given by the difference in pair state energies:

$$\Delta = E_{1'} + E_{2'} - E_1 - E_2 \tag{2.20}$$

Conceptually, this Hamiltonian says "there are two states: one at zero energy and one at energy Δ, and they are coupled by the interaction $V(\mathbf{R})$."[3] So, solving for the (normalized) eigenvectors ($\mathbf{\Psi}_\pm$) and eigenvalues ($\lambda_\pm$) of this Hamiltonian give the eigenstates and eigenenergies of the two interacting Rydberg atoms:

3. In reality, we have set the energy of the $|r_1 r_2\rangle$ state, $E_1 + E_2$, equal to zero for simplicity. If you want to calculate energy shifts on an absolute scale, note that you will need to add $E_1 + E_2$ to the eigenenergies you solve for at the end!

$$\mathbf{\Psi}_{\pm} = \begin{bmatrix} \frac{-\Delta \pm \sqrt{\Delta^2 + 4V(\mathbf{R})^2}}{V(\mathbf{R})\sqrt{8 + \frac{2\Delta}{V(\mathbf{R})^2}\left(\Delta \mp \sqrt{\Delta^2 + 4V(\mathbf{R})^2}\right)}} \\ \frac{2}{\sqrt{8 + \frac{2\Delta}{V(\mathbf{R})^2}\left(\Delta \mp \sqrt{\Delta^2 + 4V(\mathbf{R})^2}\right)}} \end{bmatrix} \tag{2.21}$$

$$\lambda_{\pm} = \frac{\Delta \pm \sqrt{\Delta^2 + 4V(\mathbf{R})^2}}{2} \tag{2.22}$$

Note that the top entry and bottom entry of $\mathbf{\Psi}_{\pm}$ give the amplitude contribution of the $|r_1 r_2\rangle$ state and $|r_{1'} r_{2'}\rangle$ state to the overall eigenstate, respectively. In this form, these eigenstates and eigenenergies do not provide a ton of intuition. However, these expressions are simplified considerably in limiting cases.

The resonant dipole-dipole interaction

In the limit $V(\mathbf{R}) \gg \Delta$, the eigenstates and eigenenergies become

$$\mathbf{\Psi}_{\pm} = \begin{bmatrix} \frac{\pm 1}{\sqrt{2}} \\ \frac{1}{\sqrt{2}} \end{bmatrix} \tag{2.23}$$

$$\lambda_{\pm} = \pm V(\mathbf{R}) \tag{2.24}$$

This limit is also considered the "short range" limit where the distance between atoms $\mathbf{R}$ is small, meaning $V(\mathbf{R})$ is large. In this limit, the eigenstates are mixtures of our original pair states: $|\Psi_{\pm}\rangle = \pm\frac{1}{\sqrt{2}}|r_1 r_2\rangle + \frac{1}{\sqrt{2}}|r_{1'} r_{2'}\rangle$. The eigenenergies $\lambda_{\pm} = \pm V(\mathbf{R}) = \pm C_3/R^3$. The coefficient C_3 is called a dispersion coefficient that scales like n^4 where n is the principle quantum number. This limit is additionally known as the resonant dipole-dipole regime. As $V(\mathbf{R}) \gg \Delta$, we can think of our initial pair states as nearly degenerate, or "resonant."

The van der Waals interaction

In the limit $V(\mathbf{R}) \ll \Delta$, the eigenstates and eigenenergies become

$$\boldsymbol{\Psi}_+ \approx \begin{bmatrix} 0 \\ 1 \end{bmatrix} \qquad \boldsymbol{\Psi}_- \approx \begin{bmatrix} -1 \\ 0 \end{bmatrix} \tag{2.25}$$

$$\lambda_+ = \Delta + \frac{V(\mathbf{R})^2}{\Delta} \qquad \lambda_- = -\frac{V(\mathbf{R})^2}{\Delta} \tag{2.26}$$

This limit is also considered the "long range" limit where the distance between atoms $\mathbf{R}$ is large, meaning $V(\mathbf{R})$ is small. In this limit, the eigenstates are nearly our original pair states (up to a phase). The eigenenergies both scale like $V(\mathbf{R})^2/\Delta = C_6/R^6$ as a result of *induced* dipole-dipole interactions, where C_6/R^6 is called the van der Waals interaction and often pops up as a potential term when dealing with interacting Rydberg atoms. The coefficient C_6 is also called a dispersion coefficient, and it scales like n^{11}. Wow! This scaling is one of the reason why we like Rydberg atoms—they interact strongly!

Rydberg blockade

The strong interactions between Rydberg atoms leads to an effect that is a foundational pillar of the work presented in this thesis: Rydberg blockade. Conceptually, Rydberg blockade can be boiled down to the following definition: if you've excited one atom to a Rydberg state, you can't excite a second atom to a Rydberg state within a certain radius of the first atom. In other words, Rydberg blockade occurs when atom-atom interactions are sufficiently strong to energetically shift the two-Rydberg state out of resonance with the excitation drive. Mathematically, this statement means the energy shift of the two-Rydberg state, C_6/R^6 (assuming the van der Waals regime), must exceed the larger of either $\hbar\Gamma_r$ or $\hbar\Omega$, where Γ_r is the natural linewidth of the Rydberg state and Ω is the excitation linewidth [20].[4]

4. This Ω is the same as the Rabi frequency of the excitation drive, which we will talk about in the next subsection!

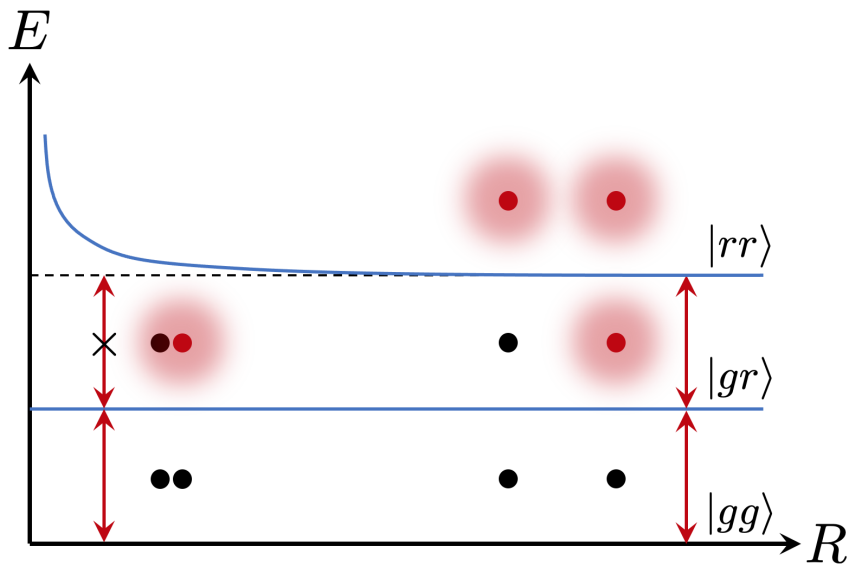

Figure 2.1: **Rydberg blockade.** Assuming the van der Waals regime and some drive depicted by red arrows, a pair state of two Rydberg atoms $|rr\rangle$ is allowed only if they are sufficiently separated. As the interatomic distance, R, decreases, the energy E of the pair state $|rr\rangle$ shifts appreciably by C_6/R^6 such that the drive is no longer in resonance with exciting two Rydberg atoms! This effect is Rydberg blockade. Take note of two items that are not depicted here: (1) $|rg\rangle$ is the same energy as $|gr\rangle$, but has been omitted for simplicity, and (2) the drive and the atomic states have linewidths, so in reality the red arrows and blue lines are "fuzzy." This fuzziness means that Rydberg blockade radius isn't a hard radius per say, and there is a chance two Rydberg atoms could still be excited.

Figure 2.1 depicts a pictorial representation of Rydberg blockade. Often times, $\Omega > \Gamma_r$ as Rydberg states are quite narrow, or long-lived. Thus, the Rydberg blockade radius R_b within which additional Rydberg excitations are suppressed is

$$R_b = \left(\frac{C_6}{\hbar\Omega}\right)^{\frac{1}{6}} \tag{2.27}$$

This radius can be more than 10 microns, which is humongous compared to the size of a ground state atom (sub-nanometer) and convenient for introducing nonlinearities into atomic gases that are experimentally practical in size.

Pair state calculation tools

In reality, there are many pair states that need to be considered when carrying out pair state calculations. Fortunately, there are resources to make life easier in terms of calculating eigenstates and eigenenergies as a function of the interatomic distance, C_3 and C_6 dispersion coefficients, and more. One such resource is listed below.

- **Pairinteraction - A Rydberg Interaction Calculator** [21]:
  https://www.pairinteraction.org/pairinteraction/sphinx/html/index.html

2.1.3 Atom-field interactions

Atoms have multiple, controllable degrees of freedom that make them a widely appealing platform for atomic, molecular, and optical physicists. Most of this control is enabled by the interactions of atoms with electromagnetic fields, for which we have even more tools to control! After an overview of some relevant terminology, this subsection will detail several key atom-field interactions:

(1) The AC Stark effect

(2) The DC Stark effect

(3) The DC Zeeman effect

The language of light-matter interactions

The dipole approximation. This approximation applies to atoms in an oscillating electric field $\mathbf{E}(t)$, such as that of light, with wavelength λ. The approximation is that λ is much greater than the size of the atom, thereby removing any spatial dependence from the interaction between the atom and $\mathbf{E}(t)$, leaving only temporal dependence. This approximation is also called "the electric dipole approximation."

Rabi frequency. The Rabi frequency, typically represented by the symbol Ω, is an angular frequency that describes the state probability oscillation in a two-level system driven on resonance. For example, an atom driven between some state $|a\rangle$ and some state $|b\rangle$ with a laser of frequency ω and electric field $\mathbf{E}(t) = \mathbf{E}_0 \cos \omega t$ will oscillate between $|a\rangle$ and $|b\rangle$. This oscillation is called Rabi flopping. Assuming the atom initially began in $|a\rangle$ and the $|a\rangle \rightarrow |b\rangle$ transition is driven on resonance, the probability of finding the atom in $|b\rangle$ is $\sin^2(\Omega t/2)$. Here, the Rabi frequency is defined as

$$\Omega = \langle a| e\mathbf{r} \cdot \mathbf{E}_0 |b\rangle /\hbar = (\mathbf{d} \cdot \mathbf{E}_0)/\hbar \tag{2.28}$$

where $\mathbf{E}_0 = E_0 \hat{\boldsymbol{e}}$ is the electric field vector, $\mathbf{d} = \langle a| e\mathbf{r} |b\rangle$ is the transition dipole matrix element between the states $|a\rangle$ and $|b\rangle$, e is the charge of the electron, and $\mathbf{r}$ is the position of the atom's valence electron relative to the atom's center of mass. Note that $e\mathbf{r}$ is an electric dipole moment, which is why the approximation in the previous paragraph is called the "dipole" approximation. Additionally note that 1) the greater the laser intensity, the larger the Rabi frequency as it depends on the electric field amplitude, 2) Ω is a coupling term and is typically found in the off-diagonal entries of Hamiltonians to represent a coupling between two orthogonal states, 3) Ω can be a complex number, and 4) you may see Ω quoted as 2π times some number in frequency units (e.g. MHz) to expressly convey Ω is an angular frequency. The mathematics in this paragraph and the concept of the Rabi frequency will be revisited in greater detail in Chapter 3.

π and $\pi/2$ pulses. The previous paragraph explained an example where the probability of finding an atom in a state $|b\rangle$ is $\sin^2(\Omega t/2)$. Therefore, the probability of finding an atom in a state $|a\rangle$ is $\cos^2(\Omega t/2)$ as the total probability of finding the atom in some state must be 1 (i.e. $\sin^2(\Omega t/2) + \cos^2(\Omega t/2) = 1$ at all times t. A π pulse is the application of a drive for some time t_π such that $\Omega t_\pi = \pi$. This pulse prepares the atom in the state

$\cos(\pi/2)|a\rangle + \sin(\pi/2)|b\rangle = |b\rangle$. In this case, a π pulse completely "flips" the state of the atom from $|a\rangle$ to $|b\rangle$. A $\pi/2$ pulse is the application of a drive for some time $t_{\pi/2}$ such that $\Omega t_{\pi/2} = \pi/2$. This pulse prepares the atom in the state $\cos(\pi/4)|a\rangle + \sin(\pi/4)|b\rangle = \frac{1}{\sqrt{2}}(|a\rangle + |b\rangle)$. In this case, a $\pi/2$ pulse prepares the atom in an equal superposition state of $|a\rangle$ and $|b\rangle$.

Linewidth. Atomic states, cavities, and lasers all have "linewidths." In the case of atomic states, the linewidth of the state is typically represented by the symbol Γ and is the rate of spontaneous decay in free space in units of angular frequency. The energy distribution of an atomic state is a Lorentzian function with a full width at half maximum (FWHM) of Γ. If viewing an atomic level diagram, this is why "broad" or short-lived states are typically depicted as thicker lines, and "narrow" or long-lived states are typically depicted as thinner lines. Γ can be found by summing over Einstein A coefficients, where a single Einstein A coefficient is the decay rate between two atomic levels $|nl\rangle \rightarrow |n'l'\rangle$. The Einstein A coefficient is defined as

$$A_{nl\rightarrow n'l'} = \frac{4e^2\omega_{nl,n'l'}^2}{3\hbar c^3}\frac{\max(l,l')}{2l+1}|\langle n'l'|\, r\, |nl\rangle|^2 \tag{2.29}$$

where $\omega_{nl,n'l'}$ is the frequency difference between states $|nl\rangle \rightarrow |n'l'\rangle$ and $\langle n'l'|\, r\, |nl\rangle$ is the radial matrix element. The linewidth of a state $|nl\rangle$ is then given by the sum over all decay channels:

$$\Gamma_{nl} = \sum_{n'l'<nl} A_{nl\rightarrow n'l'} \tag{2.30}$$

where the lifetime of state $|nl\rangle$ is given by $1/\Gamma_{nl}$. Tools such as ARC as mentioned in Subsection 2.1.1 can be used to calculate atomic state linewidths via the formulae above.[5]

5. A note particularly about spontaneous decay: so far we've claimed that there are many atomic states that are eigenstates of the atomic Hamiltonians in Subsection 2.1.1. Then shouldn't an excited state atom stay excited forever because eigenstates don't evolve in time? Well, we have disregarded interactions of the

Scattering. When an atom absorbs a photon, the photon imparts momentum to the atom, then the atom eventually spontaneously emits or "scatters" a photon into any direction (i.e. a solid angle of 4π steradians). Absorption of many photons will on average cause atoms to change momentum significantly. This effect can be utilized to cool atoms, as in the case of creating a magneto-optical trap (MOT), or heat atoms, as in the case of aligning laser beams to atomic clouds in which we will sometimes "blow the atoms away" by essentially blasting them with resonant or near-resonant light via the path we want to align. Assuming a single two-level atom driven by a laser with Rabi frequency Ω and detuning Δ, the rate Γ_{sc} at which photons are scattered is the probability that an atom is excited times the natural linewidth, Γ, of the excited state [11]:

$$\Gamma_{sc} = \frac{\Gamma}{2} \frac{\Omega^2/2}{\Delta + \Omega^2/2 + \Gamma^2/4} \tag{2.31}$$

The detuning, Δ, is related to the laser frequency, ω, and atomic resonance frequency, ω_0, by $\Delta = \omega - \omega_0$. The scattering rate Γ_{sc} is extremely relevant when imaging atoms. If you know how many you photons you've collected in a given time period along with Γ_{sc}, then you can back out useful experimental quantities like the atom number and density. These experimental ideas will be revisited in more detail in Subsection **??**. The absorption cross section of the atom, $\sigma(\omega)$, is

$$\sigma(\Delta) = \frac{3\pi c^2}{2\omega_0^2} \frac{\Gamma^2}{\Delta^2 + \Gamma^2/4} \tag{2.32}$$

As with both Γ_{sc} and $\sigma(\omega)$, atoms can scatter and absorb photons off-resonance because atomic states have non-zero linewidths. When the laser is resonant with the atom ($\Delta = 0$), the above expression reduces to

---

atom with the electromagnetic field *even in the absence of a drive*. In other words, we have disregarded interactions of the atom with the *vacuum*, which can fluctuate in energy due to the Heisenburg uncertainty principle even though the vacuum state contains *zero* photons. So in some sense, you can think of spontaneous emission as stimulated emission due to "quantum fluctuations" of the vacuum. Wild, huh?

$$\sigma(0) = \frac{6\pi c^2}{\omega_0^2} = \frac{3\lambda_0^2}{2\pi} \tag{2.33}$$

where $\lambda_0 = 2\pi c/\omega_0$, the wavelength of the laser on resonance. This is a convenient metric to remember: when a laser is resonant with an atom, the absorption cross section of the atom is about $\lambda_0^2/2$.

Selection rules. The selection rules are constraints on what transitions are possible in the atom. Essentially, they are derived in evaluating the coupling between two states. For an atom in an oscillating electric field $\mathbf{E}(t) = E(t)\hat{\boldsymbol{e}}$ such as light, the additional term we need to add to our atomic Hamiltonian is one that describes the interaction of the atom with the electric field, which can induce transitions between atomic levels. We typically call this term the "interaction Hamiltonian," $H_I = e\mathbf{r} \cdot \mathbf{E}(t)$. To find the coupling between some atomic states $|a\rangle \to |b\rangle$, we sandwich the interaction Hamiltonian between states $|a\rangle$ and $|b\rangle$:

$$\langle b| H_I |a\rangle = \langle b| e\mathbf{r} \cdot \mathbf{E}(t) |a\rangle = eE(t) \langle b| r\hat{\boldsymbol{r}} \cdot \hat{\boldsymbol{e}} |a\rangle \tag{2.34}$$

Note that the expression above is suspiciously reminiscent of the expression for the Rabi frequency. That's because it is, and we could substitute in the Rabi frequency in the expression above if we wanted to! However from here, we will instead use the spatial atomic wavefunctions of states $|a\rangle$ and $|b\rangle$ to acquire $\langle b| r\hat{\boldsymbol{r}} \cdot \hat{\boldsymbol{e}} |a\rangle$:

$$|a\rangle = R_{n_a,l_a} Y_{l_a,m_a} \tag{2.35}$$

$$|b\rangle = R_{n_b,l_b} Y_{l_b,m_b} \tag{2.36}$$

$$\langle b|\, r\hat{\boldsymbol{r}}\cdot\hat{\boldsymbol{e}}\,|a\rangle = \int_0^{2\pi}\int_0^{\pi}\int_0^{\infty} R^*_{n_b,l_b}Y^*_{l_b,m_b}r\hat{\boldsymbol{r}}\cdot\hat{\boldsymbol{e}}R_{n_a,l_a}Y_{l_a,m_a}r^2\sin\theta\,dr\,d\theta\,d\phi \tag{2.37}$$

R_{n_i,l_i} and Y_{l_i,m_i} are the radial and angular wavefunction, respectively, of the state $|i\rangle$ where $i \in \{a, b\}$. Fortunately, if we actually wanted to evaluate this integral, we can be lazy and have a computer program do it for us. However, the upshot here is that sometimes this integral goes to zero, meaning the coupling $\langle b|\, H_I\,|a\rangle$ is zero and the transition is forbidden. The cases in which this integral is zero are rather specific, leading to specific transition constrains we call the selection rules. Table 2.1 contains the selection rules for electric dipole transitions between fine structure states and hyperfine structure states.

	Fine structure	Hyperfine structure
Interaction	$\mathbf{L}\cdot\mathbf{S}$	$\mathbf{I}\cdot\mathbf{J}$
Total angular momentum	$\mathbf{J}=\mathbf{L}+\mathbf{S}$	$\mathbf{F}=\mathbf{I}+\mathbf{J}$
Eigenstates	$\lvert LSJM_J\rangle$	$\lvert IJFM_F\rangle$
Energy scaling	$\propto Z^2$	$\propto Z$
Selection rules	$\Delta L = 0, \pm 1$ $(L = 0 \nleftrightarrow 0)$	$\Delta I = 0$
	$\Delta S = 0$	$\Delta J = 0, \pm 1$ $(J = 0 \nleftrightarrow 0)$
	$\Delta J = 0, \pm 1$ $(J = 0 \nleftrightarrow 0)$	$\Delta F = 0, \pm 1$ $(F = 0 \nleftrightarrow 0)$
	$\Delta M_J = 0, \pm 1$	$\Delta M_F = 0, \pm 1$

Table 2.1: **Properties of electric dipole transitions.** This table was inspired by [11]. Note that there are no constrains on changes in the principle quantum number, Δn. Additionally note that here, capital letters represent total quantities over many electrons. The case in which this concept becomes relevant is for ΔL versus Δl. For a single electron, $\Delta l = \pm 1$ (i.e. S to S, P to P, etc. transitions are forbidden). We typically write Rydberg states as $|LSJM_J\rangle$ states since the electron orbit is further away from the nucleus in highly excited atoms, thereby reducing the interaction of the electron with the nucleus and making hyperfine structure calculations not strictly necessary. On the other hand, we typically write lower energy states (e.g. the $5S_{1/2}$ and $5P_{3/2}$ states of ^{87}Rb) as $|IJFM_F\rangle$ states where the electron interaction with the nucleus is more relevant as the electron is physically closer to the nucleus. Thus, in terms of the angular momenta I and J, lower energy states are written in the coupled basis whereas Rydberg states are written in the uncoupled basis. If considering a transition between a lower energy state and a Rydberg state, you will need to apply the Wigner-Eckhart theorem to calculate quantities such as the dipole matrix element for the transition.

The AC Stark effect

The AC Stark effect, or "light shift," arises from the interaction between an atom and an oscillating (i.e. AC) electric field, typically a laser. The interaction Hamiltonian that describes this interaction is the same as the previous paragraph:

$$H_I = e\mathbf{r} \cdot \mathbf{E}(t) \tag{2.38}$$

Here, $\mathbf{E}(t) = \mathbf{E}_0 \cos\omega t$,[6] where ω is the oscillation frequency of the electric field (or the frequency of your laser). H_I comes from the form $-\boldsymbol{\mu}\cdot\mathbf{E}$, where here $\boldsymbol{\mu} = -e\mathbf{r}$ and $\mathbf{E} = \mathbf{E}(t)$. The full Hamiltonian, H, becomes

$$H = H_{atom} + H_I \tag{2.39}$$

where $H_{atom} = H_0 + H_{\text{fs}} + H_{\text{hfs}}$ is the atomic Hamiltonian given by Subsection 2.1.1. Let's consider two atomic levels $|a\rangle$ and $|b\rangle$ with eigenenergies $E_a = \hbar\omega_a$ and $E_b = \hbar\omega_b$, respectively. In matrix form, the full Hamiltonian is

$$H = \begin{pmatrix} \langle a| H |a\rangle & \langle a| H |b\rangle \\ \langle b| H |a\rangle & \langle b| H |b\rangle \end{pmatrix} = \begin{pmatrix} E_a & \hbar\Omega\cos\omega t \\ \hbar\Omega^*\cos\omega t & E_b \end{pmatrix} \tag{2.40}$$

where the diagonal elements are simply the eigenenergies of the eigenstates $|a\rangle$ and $|b\rangle$, $\langle a| H_{atom} |a\rangle = E_a$ and $\langle b| H_{atom} |b\rangle = E_b$, and the off-diagonal elements arise purely from the interaction Hamiltonian $\langle a| H_I |b\rangle = \hbar\Omega\cos\omega t$ and $\langle b| H_I |a\rangle = \hbar\Omega^*\cos\omega t$. The elements $\langle a| H_{atom} |b\rangle = \langle b| H_{atom} |a\rangle = \langle a| H_I |a\rangle = \langle b| H_I |b\rangle = 0$ because H_{atom} doesn't induce atomic state changes and H_I is an odd function, so any integration over an even function

6. Note that we use $\mathbf{E}_0\cos\omega t$ here instead of $\mathbf{E}_0 e^{i\omega t}$ because electric fields are *real*. Using the complex representation of the field can potentially lead to incorrect conclusions (e.g. $|\cos\omega t| = \cos\omega t$ is a very different number than $|e^{i\omega t}| = 1$). If your heart is set on working with complex numbers, just remember to define your electric field in a way that extracts the real component (e.g. $\mathbf{E}_0\text{Re}(e^{i\omega t})$ or $\frac{\mathbf{E}_0}{2}(e^{i\omega t} + e^{-i\omega t})$).

times H_I will be odd and thus zero.[7] Note that we have inserted the Rabi frequency, Ω into the expression above where Ω is defined in Equation 2.28.

Ideally, we'd like to find the eigenvalues of this Hamiltonian to see how the presence of an AC electric field changes our eigenenergies. However, there are some simplifications we can make first with the goal of eliminating time-dependence in particular:

(1) **Subtract E_a.** Instead of working with absolute energies E_a and E_b, we are now going to work with relative energies by subtracting E_a from the diagonal elements. All that is happening here is a redefinition of our state energies, which does not impact the off-diagonal terms. Now our Hamiltonian is

$$H = \begin{pmatrix} 0 & \hbar\Omega\cos\omega t \\ \hbar\Omega^*\cos\omega t & E_b - E_a \end{pmatrix} = \begin{pmatrix} 0 & \hbar\Omega\cos\omega t \\ \hbar\Omega^*\cos\omega t & \hbar\omega_0 \end{pmatrix} \tag{2.41}$$

where $\omega_0 = \omega_b - \omega_a$ is the transition frequency between $|a\rangle$ and $|b\rangle$.

(2) **Factor out $\hbar$.** Since all terms of our Hamiltonian contain a factor of $\hbar$, we're just going to factor them out. This step is a quick step, but will result in a more "typical"-looking Hamiltonian. This step also emphasizes frequency terms instead of energy terms, which can be useful since we directly measure frequencies instead of energies in the lab anyway. Now our Hamiltonian is

$$H = \hbar \begin{pmatrix} 0 & \Omega\cos\omega t \\ \Omega^*\cos\omega t & \omega_0 \end{pmatrix} \tag{2.42}$$

(3) **The rotating frame transformation**. Here, we are going to perform a unitary transformation to the Hamiltonian that will put us in the frame rotating at ω, the field

7. $\langle a|a\rangle$ and $\langle b|b\rangle$ will always be an integrals over an even function regardless of whether $|a\rangle$ and $|b\rangle$ are even or odd functions just as $x^n \times x^n = x^{2n}$ will always be an even function regardless of whether n is even or odd.

oscillation frequency (or laser frequency). We will use the unitary matrix

$$U = \begin{pmatrix} 1 & 0 \\ 0 & e^{i\omega t} \end{pmatrix} \tag{2.43}$$

The transformed Hamiltonian H' is

$$H' = UHU^\dagger + i\hbar \frac{\partial U}{\partial t} U^\dagger \tag{2.44}$$

$$= \hbar \begin{pmatrix} 1 & 0 \\ 0 & e^{i\omega t} \end{pmatrix} \begin{pmatrix} 0 & \Omega \cos \omega t \\ \Omega^* \cos \omega t & \omega_0 \end{pmatrix} \begin{pmatrix} 1 & 0 \\ 0 & e^{-i\omega t} \end{pmatrix} + i\hbar \begin{pmatrix} 0 & 0 \\ 0 & i\omega \end{pmatrix} \tag{2.45}$$

$$= \hbar \begin{pmatrix} 0 & e^{-i\omega t}\Omega \cos \omega t \\ e^{i\omega t}\Omega^* \cos \omega t & \omega_0 \end{pmatrix} + i\hbar \begin{pmatrix} 0 & 0 \\ 0 & i\omega \end{pmatrix} \tag{2.46}$$

$$= \hbar \begin{pmatrix} 0 & e^{-i\omega t}\Omega \cos \omega t \\ e^{i\omega t}\Omega^* \cos \omega t & \omega_0 - \omega \end{pmatrix} \tag{2.47}$$

(4) **The rotating wave approximation.** Take note: this approximation is distinctly different from the rotating *frame* transformation above. Let's begin by splitting up $\cos \omega t$ into its complex components:

$$\cos \omega t = \frac{1}{2}(e^{i\omega t} + e^{-i\omega t}) \tag{2.48}$$

plugging this expression into our transformed Hamiltonian (Equation 2.47) yields

$$H' = \hbar \begin{pmatrix} 0 & \frac{\Omega}{2}(e^{i(\omega-\omega)t} + e^{-i(\omega+\omega)t}) \\ \frac{\Omega^*}{2}(e^{i(\omega+\omega)t} + e^{-i(\omega-\omega)t}) & \omega_0 - \omega \end{pmatrix} \tag{2.49}$$

$$= \hbar \begin{pmatrix} 0 & \frac{\Omega}{2}(1 + e^{-i(2\omega)t}) \\ \frac{\Omega^*}{2}(e^{i(2\omega)t} + 1) & \omega_0 - \omega \end{pmatrix} \tag{2.50}$$

The terms $e^{-i(2\omega)t}$ and $e^{i(2\omega)t}$ are very high frequency (in actual frequency units, ω is many THz if we assume the oscillating electric field is generated by a laser!). Thus, we can drop these terms as they will average to zero over any reasonable interaction time as Ω is typically on the MHz to GHz scale at most (at least, in the scope of the work presented in this thesis). The dropping of these terms is the rotating wave approximation. Now, the Hamiltonian is

$$H' = \hbar \begin{pmatrix} 0 & \frac{\Omega}{2} \\ \frac{\Omega^*}{2} & \omega_0 - \omega \end{pmatrix} = \hbar \begin{pmatrix} 0 & \frac{\Omega}{2} \\ \frac{\Omega}{2} & -\Delta \end{pmatrix} \tag{2.51}$$

where the detuning $\Delta = \omega - \omega_0$ and we have assumed Ω to be real in the last step.

Now we have eliminated the time dependence from the Hamiltonian! Phew! The eigenvalues, $\lambda_\pm$, of the Hamiltonian from Equation 2.51 are

$$\lambda_\pm = \frac{-\hbar\Delta}{2} \pm \frac{\hbar\sqrt{\Delta^2 + \Omega^2}}{2} \tag{2.52}$$

Typically, we talk about the AC Stark effect far from the atomic resonance where $|\Delta| \gg \Omega$. In this limit, the eigenvalues become

$$\lambda_+ = 0 + \frac{\hbar\Omega^2}{4\Delta} \tag{2.53}$$

$$\lambda_- = -\hbar\Delta - \frac{\hbar\Omega^2}{4\Delta} \tag{2.54}$$

In words, these expressions mean that the AC Stark effect energetically shifts our initial energies (i.e. 0 and $-\hbar\Delta$ from the diagonal elements of Equation 2.51) by $\pm\frac{\hbar\Omega^2}{4\Delta}$. For *red* detuned light ($\Delta < 0$), the states energetically shift *away* from each other. For *blue* detuned light, the states energetically shift *toward* each other.

In summary, this energetic shift of atomic states by $\pm\frac{\hbar\Omega^2}{4\Delta}$ due to a detuned, oscillating electric field is the AC Stark shift, which can be quite useful for manipulating atomic states.

The DC Stark effect

The DC Stark effect [22] arises from the interaction between an atom and a DC electric field, such as from electrodes. The interaction Hamiltonian that describes this interaction is

$$H_I = e\mathbf{r} \cdot \mathbf{E} \tag{2.55}$$

Here, $\mathbf{E} = E_0\hat{\boldsymbol{e}}$. Once again, we will consider two atomic levels $|a\rangle$ and $|b\rangle$ with eigenenergies $E_a = \hbar\omega_a$ and $E_b = \hbar\omega_b$, respectively, and the full Hamiltonian is $H = H_{atom} + H_I$ as in Equation 2.39 (except now H_I is the interaction Hamiltonian above). In matrix form, the full Hamiltonian is

$$H = \begin{pmatrix} \langle a| H |a\rangle & \langle a| H |b\rangle \\ \langle b| H |a\rangle & \langle b| H |b\rangle \end{pmatrix} = \begin{pmatrix} E_a & \hbar\Omega \\ \hbar\Omega^* & E_b \end{pmatrix} \rightarrow \hbar \begin{pmatrix} 0 & \Omega \\ \Omega & \omega_0 \end{pmatrix} \tag{2.56}$$

where $\omega_0 = \omega_b - \omega_a$ and Ω is the Rabi frequency. This Hamiltonian is time-independent already! Nice! We have made just a few simplifications from the second to last step to the

last step in the equation above, namely 1) shifting the energy scale (i.e. subtracting E_a from the diagonal elements), 2) factoring out $\hbar$, and 3) assuming Ω is real. The eigenvalues, or eigenenergies, of this Hamiltonian, $\lambda\pm$, are

$$\lambda_{\pm} = \frac{\hbar\omega_0}{2} \pm \frac{\hbar\sqrt{\omega_0^2 + 4\Omega^2}}{2} \tag{2.57}$$

Note that the form of these eigenvalues looks suspiciously similar to the forms of both Equations 2.22 and 2.52. This is because the forms of the Hamitlonians from whence all of these eigenvalues were derived are essentially the *same*. The form of the Hamiltonian as in Equation 2.56 is fairly common and worth remembering! Let's take a look at two different limits for $\lambda_{\pm}$ above:

(1) $\boldsymbol{\Omega \ll \omega_0}$. This limit is the "weak field" limit. Remember, Ω is directly proportional to the electric field amplitude, and Ω is small in this limit. The eigenvalues become

$$\lambda_+ = 0 - \frac{\hbar\Omega^2}{\omega_0} \tag{2.58}$$

$$\lambda_- = \hbar\omega_0 + \frac{\hbar\Omega^2}{\omega_0} \tag{2.59}$$

In words, these expressions mean that the DC Stark effect energetically shifts our initial energies (i.e. 0 and $\hbar\omega_0$ from the diagonal elements of Equation 2.56) by $\pm\frac{\hbar\Omega^2}{\omega_0}$, very similar to the AC Stark effect. This shift is often rewritten in terms of a quantity called the polarizability, α_0, which scales like n^7 where n is the principle quantum number [16].[8] This is why atoms which high principle quantum number (i.e. Rydberg atoms) are extremely sensitive to electric fields![9] The state-dependent energy shift,

8. Ω depends on the dipole matrix element, which scales like n^2. ω_0 depends on the atomic level spacing, which scales like n^{-3}. So, the DC Stark shift of $\pm\frac{\hbar\Omega^2}{\omega_0}$, and therefore the polarizability, scales like $\frac{(n^2)^2}{n^{-3}} = n^7$.

9. If you happen to be a graduate student attempting to experimentally zero the electric field for your

ΔE, and the polarizability for a state $|i\rangle$ are [23]

$$\Delta E = -\frac{1}{2}\alpha_0 E_0^2 \tag{2.60}$$

$$\alpha_0 = 2\sum_{j\neq i} \frac{|\langle i| e\mathbf{r}\cdot\hat{\boldsymbol{e}}|j\rangle|^2}{E_j - E_i} \tag{2.61}$$

Note that ΔE is the state-dependent because α_0 is state-dependent. In our two-level example with states $|a\rangle$ and $|b\rangle$ above, $\alpha_0 = 2\frac{(\hbar\Omega/E_0)^2}{\hbar\omega_0}$ for state $|a\rangle$ and $\alpha_0 = -2\frac{(\hbar\Omega/E_0)^2}{\hbar\omega_0}$ for state $|b\rangle$, leading to energy shifts $\Delta E = -\frac{\hbar\Omega^2}{\omega_0}$ and $\Delta E = \frac{\hbar\Omega^2}{\omega_0}$ for states $|a\rangle$ and $|b\rangle$, respectively (the same conclusion we came to initially).

Additionally note that Equation 2.61 is awfully reminiscent of good old second-order perturbation theory. Essentially, it *is* second-order perturbation theory, where the first order is vanishing in this case of applying a weak electric field to a set of non-degenerate states.

(2) $\boldsymbol{\Omega \gg \omega_0}$. This limit is both the "strong field" limit and the "degenerate states" limit. The eigenvalues become

$$\lambda_\pm = \mp\hbar\Omega \tag{2.62}$$

In words, this expression means the energy shift is linear in the electric field (as $\Omega \propto E_0$) for either strong electric fields or for all field magnitudes in the case of degenerate atomic states.

In reality, atoms have many, many states. In order to calculate experimentally accurate

sensitive Rydberg atoms, you can tell when you're close because your atomic spectra will look *quadratic* in the electric field about zero!

DC Stark shifts, one must include all states that are energetically close to a state of interest in the Hamiltonian. Once again, calculational tools like ARC can help you do this.

In summary, the DC Stark shift is *quadratic* in the electric field for weak fields and *linear* in the applied electric field for strong fields (or degenerate states). This shift can be useful for "splitting out" degenerate states, or as a metric for experimentally tuning electric fields to zero.

The DC Zeeman effect

The DC Zeeman effect, or just "the Zeeman effect," arises from the interaction between an atom and a DC magnetic field, such as from magnetic coils. We will consider only the first order energy corrections in the weak field limits where 1) the atom-field interaction is perturbative to the fine structure atomic Hamiltonian, and 2) the atom-field interaction is perturbative to the hyperfine structure atomic Hamiltonian. In other words, we will examine two cases where the energy shift due to the atom-field interaction is small compared to 1) the fine structure splittings, and 2) the hyperfine structure splittings.

(1) **Perturbation to fine structure states.** The interaction Hamiltonian that describes the Zeeman effect, under the assumption it is a small perturbation to the fine structure Hamiltonian, is [13]

$$H_I = -(\boldsymbol{\mu}_S + \boldsymbol{\mu}_L) \cdot \mathbf{B} \tag{2.63}$$

$$= \frac{\mu_B}{\hbar}(g_S \mathbf{S} + g_L \mathbf{L}) \cdot \mathbf{B} \tag{2.64}$$

$$= \frac{\mu_B}{\hbar}(g_S S_z + g_L L_z) B_0 \tag{2.65}$$

Here, $\boldsymbol{\mu}_S = \frac{\mu_B g_S}{\hbar}\mathbf{S}$ is the magnetic dipole moment due to the electron spin, $\boldsymbol{\mu}_L = \frac{\mu_B g_L}{\hbar}\mathbf{L}$ is the magnetic dipole moment due to the electron orbit, $\mu_B = e\hbar/2m_e$ is the

Bohr magneton, and we have assumed the magnetic field B_0 to be along the z-axis in the last step above. The factors g_S and g_L are the electron spin and orbital g-factors, respectively, where the "g-factors" are dimensionless proportionality constants that essentially relate experimentally observed magnetic moments to their respective angular momenta. H_I comes from the form $-\boldsymbol{\mu} \cdot \mathbf{B}$, where here $\boldsymbol{\mu} = \boldsymbol{\mu}_l + \boldsymbol{\mu}_s$. Taking the first order perturbation using the fine structure states $|Jm_J\rangle$ yields the energy shift, ΔE, due to the Zeeman effect:

$$\Delta E = \langle Jm_J | \, H_I \, | Jm_J \rangle \tag{2.66}$$

$$= \mu_B g_J m_J B_0 \tag{2.67}$$

$$g_J = g_L + (g_S - g_L)\frac{J(J+1) + S(S+1) - L(L+1)}{2J(J+1)} \tag{2.68}$$

$$\approx 1 + \frac{J(J+1) + S(S+1) - L(L+1)}{2J(J+1)} \tag{2.69}$$

where we've plugged in the values $g_L \approx 1$ and $g_S \approx 2$ in the last step. Here, we have basically skipped to the punchline without explicit algebra as derivations of the Zeeman energy shift are fairly uniform across atomic physics and quantum mechanics literature [11, 24, 13].

(2) **Perturbation to hyperfine structure states.** The interaction Hamiltonian that describes the Zeeman effect, under the assumption it is a small perturbation to the hyperfine structure Hamiltonian, is very similar to that of the fine structure case [25]:

$$H_I = -(\boldsymbol{\mu}_S + \boldsymbol{\mu}_L + \boldsymbol{\mu}_I) \cdot \mathbf{B} \tag{2.70}$$

$$= \frac{\mu_B}{\hbar}(g_S \mathbf{S} + g_L \mathbf{L} + g_I \mathbf{I}) \cdot \mathbf{B} \tag{2.71}$$

$$= \frac{\mu_B}{\hbar}(g_S S_z + g_L L_z + g_I I_z) B_0 \tag{2.72}$$

$$= \frac{\mu_B}{\hbar}(g_J J_z + g_I I_z) B_0 \tag{2.73}$$

Here, g_I is the nuclear spin g-factor and I is the nuclear spin operator. Taking the first order perturbation using the hyperfine structure states $|Fm_F\rangle$ yields the energy shift, ΔE, due to the Zeeman effect:

$$\Delta E = \langle Fm_F | \, H_I \, | Fm_F \rangle \tag{2.74}$$

$$= \mu_B g_F m_F B_0 \tag{2.75}$$

$$g_F = g_J + (g_I - g_J)\frac{F(F+1) + I(I+1) - J(J+1)}{2F(F+1)} \tag{2.76}$$

$$\approx g_J \frac{F(F+1) - I(I+1) + J(J+1)}{2F(F+1)} \tag{2.77}$$

where the last step simplification could be made because $g_I \ll g_J$ [26].[10] Once again, we have basically skipped to the punchline.

Note that we haven't mentioned the AC Zeeman effect at all. If atoms can couple to oscillating electric fields, shouldn't they be able to couple to oscillating magnetic fields?

10. $g_I \approx -0.001$ for ^{87}Rb.

Atoms *do* couple to oscillating magnetic fields which leads to *magnetic* dipole transitions as opposed to *electric* dipole transitions, but we typically use only the language of electric dipole transitions as magnetic dipole transitions are rather weak. However, there are still instances in which magnetic dipole transitions are used, such as in coupling different Zeeman sublevels or hyperfine states using microwaves.

In summary, the energy shift due to the weak field Zeeman effect is *linear* in the applied magnetic field field for both fine structure and hyperfine structure states.

2.2 Cavities

In the context of atomic, molecular, and optical physics, cavities[11] are used widely as a tool for manipulating light and light-matter interactions [27]. In the lab, we often generate our light-matter interactions via lasers at *optical* frequencies that excite atomic transitions. Hence, this section will overview various mathematical tools and parameters that are useful for characterizing *optical* cavities, which are generally structures comprised of two or more mirrors that confine light.

2.2.1 Gaussian beams

Before we can examine how light behaves inside a cavity, we should first examine how light behaves more generally. We know light must obey Maxwell's equations, and from Maxwell's equations we can construct a wave equation for light. Solving this equation, the "paraxial Helmholtz equation," gives us the mathematical form for what we call Gaussian beams, monochromatic electromagnetic waves whose transverse field amplitudes follow Gaussian functions (see Table 2.2). In other words, solving this equations basically gives us the mathematical form of a laser beam, which turns out to be quite useful if you work with

11. You may hear "resonator," "Fabry-Pérot interferometer," or "etalon" in place of "cavity." In essence, they all describe the same object.

lasers. This subsection will overview some of the main ideas and mathematical expressions that describe Gaussian beams, how they behave in free space, and how they transform through optical elements.

$$\mathbf{E}(r,z) = \mathbf{E}_0 \frac{\omega_0}{\omega(z)} \exp\left(\frac{-r^2}{\omega(z)^2}\right) \exp\left(-i\left(kz + k\frac{r^2}{2R(z)} - \psi(z)\right)\right) \tag{2.78}$$

Quantity	Symbol	Expression
Field amplitude, phase, and direction	$\mathbf{E}_0$	
Radial distance	r	
Axial distance	z	
Wavelength	λ	
Refractive index	n	
Waist radius	ω_0	
Wave number	k	$\frac{2\pi n}{\lambda}$
Rayleigh range	z_R	$\frac{\pi\omega_0^2 n}{\lambda}$
Beam radius	$\omega(z)$	$\omega_0\sqrt{1+\left(\frac{z}{z_R}\right)^2}$
Radius of curvature	$R(z)$	$z\left(1+\left(\frac{z}{z_R}\right)^2\right)$
Gouy phase	$\psi(z)$	$\arctan\left(\frac{z}{z_R}\right)$

Table 2.2: **Electric field of a Gaussian beam.** This table was inspired by the "Gaussian beam" page on Wikipedia. Note that the beam radius is defined by the radial distance at which the field amplitude falls to $1/e$ of its value at $r = 0$, which corresponds with $1/e^2$ in intensity. Additionally note that the Rayleigh range is the axial distance where $\omega(z_R) = \sqrt{2}\omega_0$. In summary, Equation 2.78 describes a Gaussian beam in free space.

The language of light

The paraxial approximation. In basic laser alignment and cavity construction, we often assume that light travels at small angles relative to some optical axis formed by optical components. In other words, the angle, θ, between the wave vector, $\mathbf{k}$, and the optical axis is small, such that $\sin\theta \approx \tan\theta \approx \theta$. Note that $|\mathbf{k}| = k = 2\pi n/\lambda$ is the wave number. This "small θ" approximation is called the paraxial approximation.

ABCD matrices. Also called "ray transfer matrices," the ABCD matrices are a collection of matrices that describe how optical elements transform the properties of a beam in the paraxial regime [28]. While not limited to 2×2 matrices, the ABCD matrices are often expressed as 2×2 matrices with elements A, B, C, and D with determinant

$$AD - BC = 1 \tag{2.79}$$

so long as rays enter and leave optical elements in media of the same refractive index. There are two major instances in which we use the ABCD matrices: (1) to transform light as a ray, and (2) to transform light as a Gaussian beam.

(1) **Light as a ray.** As a ray, the ABCD matrices transform the position and slope vector of light:

$$\begin{pmatrix} r_f \\ r'_f \end{pmatrix} = \begin{pmatrix} A & B \\ C & D \end{pmatrix} \begin{pmatrix} r_i \\ r'_i \end{pmatrix} \tag{2.80}$$

where $r_i = r(z_i)$ is the initial position relative to some optical axis and $r'_i = \frac{dr(z)}{dz}\big|_{z=z_i} \approx \theta_i$ is the initial slope. r_f and r'_f are the ray's final position and slope, respectively.

(2) **Light as a Gaussian beam.** As a Gaussian beam, the ABCD matrices transform the complex beam parameter [28]:

$$q_f = \frac{Aq_i + B}{Cq_i + D} \tag{2.81}$$

where

$$q(z) = z + iz_R \tag{2.82}$$

$$\frac{1}{q(z)} = \frac{1}{R(z)} - \frac{i\lambda}{n\pi\omega(z)^2} \tag{2.83}$$

Table 2.3 lists some common ABCD matrices. Note that the electric field formula for a Gaussian beam of Equation 2.78 may also be written in a much simpler form (excluding the kz and $\psi(z)$ phase factors) using the complex beam parameter for ease of extracting experimentally relevant quantities such as the waist and radius of curvature:

$$E(r,z) = E_0 \frac{1}{q(z)} \exp\left(-ik\frac{r^2}{2q(z)}\right) \tag{2.84}$$

It is necessary to use ABCD matrices larger than 2×2 when dealing with higher dimensional spaces and misaligned optical elements [28, 29]. For instance, the work presented in this thesis utilizes a twisted, non-planar, 4-mirror cavity in which both the x and y positions and slopes become relevant. Thus, the vector to be transformed in a cavity such as this is

$$\begin{pmatrix} x \\ x' \\ y \\ y' \end{pmatrix} \tag{2.85}$$

thereby necessitating 4×4 ABCD matrices. In the case of misaligned optical elements, the misalignment can be captured by an additional ABCD matrix dimension. The general

Transformation	Matrix
Propagation by a distance d through constant refractive index	$\begin{pmatrix} 1 & d \\ 0 & 1 \end{pmatrix}$
Reflection from a curved mirror with radius of curvature R	$\begin{pmatrix} 1 & 0 \\ -\frac{2}{R} & 1 \end{pmatrix}$
Refraction through a thin lens with focal length f	$\begin{pmatrix} 1 & 0 \\ -\frac{1}{f} & 1 \end{pmatrix}$

Table 2.3: **ABCD matrices.** Note that reflection from a curved mirror occurs at normal incidence. $R > 0$ for concave mirrors and $f > 0$ for convex lenses. Notice how propagation changes only a ray's position r whereas reflection from a curved mirror and refraction through a thin lens change only a ray's slope r'.

transformation of a ray's position and slope vector in one dimension becomes the 3×3 ABCD matrix

$$\begin{pmatrix} r_f \\ r'_f \\ 1 \end{pmatrix} = \begin{pmatrix} A & B & E \\ C & D & F \\ 0 & 0 & 1 \end{pmatrix} \begin{pmatrix} r_i \\ r'_i \\ 1 \end{pmatrix} \tag{2.86}$$

where matrix elements E and F quantify the amount of misalignment. See Reference [28] for additional details.

2.2.2 Is it a cavity?

Let's say you're in the lab, you pick up a few random mirrors, and mount them on an optical table generally facing one another. Is it a cavity? We answer "yes" if a light ray can be confined indefinitely between the cavity mirrors.[12]

12. This statement assumes perfectly reflective mirrors. In the case of somewhat transmissive mirrors, we may still answer "yes, it's a cavity" even if light cannot be confined indefinitely so long as light is *transmitted* through the cavity mirrors before it can "leak off" a physical mirror edge.

The stability criterion

A cavity that can confine a light ray indefinitely is called "stable." A cavity than cannot confine a light ray indefinitely is called "unstable."[13] The "stability criterion" is the criterion that needs to be met in order for a cavity to be considered stable. This criterion can be expressed mathematically by modeling the cavity as a matrix that transforms a light ray's position and slope vector in the ABCD matrix formalism. We define the optical axis as the axis formed by connecting the center points of the mirrors, and the coordinate z as the distance along it.[14] After one round trip through the cavity, the ray's initial position relative to the optical axis and slope transform as in Equation 2.86.

So how do we determine if an arbitrary ray will be confined by the cavity forever? If the ray is confined forever, its position and slope must not diverge after N round trips through the cavity. The divergence of the position and slope physically corresponds to the ray escaping from the cavity. Finite-sized mirrors that are spaced apart can't confine rays with infinite position and slope! After N round trips in the cavity, the ray's position and slope transform as

$$\begin{pmatrix} r_f \\ r'_f \end{pmatrix} = \begin{pmatrix} A & B \\ C & D \end{pmatrix}^N \begin{pmatrix} r_i \\ r'_i \end{pmatrix} \tag{2.87}$$

$$= \frac{1}{\sin\phi} \begin{pmatrix} A\sin N\phi - \sin(N-1)\phi & B\sin N\phi \\ C\sin N\phi & D\sin N\phi - \sin(N-1)\phi \end{pmatrix} \begin{pmatrix} r_i \\ r'_i \end{pmatrix} \tag{2.88}$$

where

13. Some may even say "there is no cavity."

14. Note that the optical axis may not be a line that extends to infinity. For example, a three-mirror cavity forms an optical axis that looks like a triangle!

$$\cos\phi = \frac{A+D}{2} \tag{2.89}$$

we have kept elements A, B, C, and D as general coefficients for now, but will plug in meaningful values later. Here, we have utilized a result from [30] to acquire the N^{th} power of the ABCD matrix based on Sylverster's theorem.

If ϕ is complex, r_f and r'_f diverge as $N \to \infty$ because the sine terms like $\sin N\phi / \sin\phi = (e^{iN\phi} - e^{-iN\phi})/(e^{i\phi} - e^{-i\phi})$ then contain a real part that blows up.

If ϕ is real, r_f and r'_f do not diverge as $N \to \infty$ because the sine terms like $\sin N\phi / \sin\phi = (e^{iN\phi} - e^{-iN\phi})/(e^{i\phi} - e^{-i\phi})$ are then oscillatory.

Thus, ϕ must be real in order for rays to be forever confined within the cavity, leading to the stability criterion $-1 \leq \cos\phi \leq 1$, or

$$-1 \leq \frac{A+D}{2} \leq 1 \tag{2.90}$$

The stability criterion for a two-mirror cavity

In order to determine the stability criterion for a two-mirror cavity, we first need to determine the round trip ABCD matrix for a such a cavity. From the ABCD matrices in Table 2.3, we can construct the round trip matrix of a cavity comprised of two mirrors, one of radius R_1 and one of radius R_2, separated be a distance L by multiplying the ABCD matrices for the individual cavity components in succession:

$$\begin{pmatrix} A & B \\ C & D \end{pmatrix} = \begin{pmatrix} 1 & L \\ 0 & 1 \end{pmatrix} \begin{pmatrix} 1 & 0 \\ -2/R_2 & 1 \end{pmatrix} \begin{pmatrix} 1 & L \\ 0 & 1 \end{pmatrix} \begin{pmatrix} 1 & 0 \\ -2/R_1 & 1 \end{pmatrix} \tag{2.91}$$

$$= \begin{pmatrix} 1 - \frac{4L}{R_1} - \frac{2L}{R_2} + \frac{4L^2}{R_1 R_2} & 2L - \frac{2L^2}{R_2} \\ -\frac{2}{R_1} - \frac{2}{R_2} + \frac{4L}{R_1 R_2} & 1 - \frac{2L}{R_2} \end{pmatrix} \tag{2.92}$$

Physically, the ABCD matrix above corresponds to a ray that reflects off the first mirror, propagates across the cavity length, reflects off the second mirror, then propagates across the cavity length once more.[15] Note that the order of these operations read right to left in Equation 2.91 as right to left is the order in which the matrices will act on a ray's position and slope vector. The stability criterion is thus

$$-1 \leq \frac{A+D}{2} \leq 1 \tag{2.93}$$

$$\downarrow \tag{2.94}$$

$$-1 \leq 1 - \frac{2L}{R_1} - \frac{2L}{R_2} + \frac{2L^2}{R_1 R_2} \leq 1 \tag{2.95}$$

$$\downarrow \tag{2.96}$$

$$0 \leq 1 - \frac{L}{R_1} - \frac{L}{R_2} + \frac{L^2}{R_1 R_2} \leq 1 \tag{2.97}$$

$$\downarrow \tag{2.98}$$

$$0 \leq g_1 g_2 \leq 1 \tag{2.99}$$

where

$$g_1 = 1 - \frac{L}{R_1} \tag{2.100}$$

$$g_2 = 1 - \frac{L}{R_2} \tag{2.101}$$

Figure 2.2 depicts a visual representation of this stability criterion for different combinations of g_1 and g_2, corresponding with different choices of L, R_1, and R_2.

15. We could equally have written down these matrices in a different order, for example starting with propagation first or at the middle of the cavity instead of an end. The result will be the same!

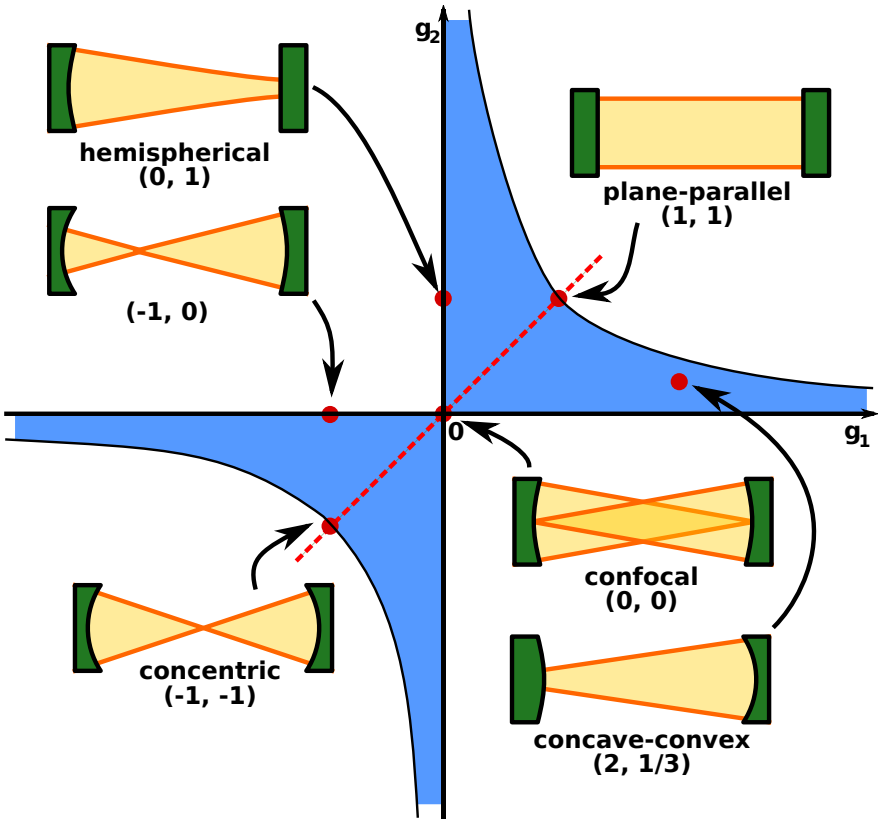

Figure 2.2: **Cavity stability.** Light can be confined in cavities whose geometries obey the stability criterion. Stable cavities lie in the blue region. Figure used from "Optical cavity" Wikipedia webpage.

2.2.3 Cavity parameters

The subsection will overview common cavity parameters and how to find them both theoretically and experimentally. This overview will include the following main ideas:

(1) Free spectral range

(2) Linewidth

(3) Finesse

(4) Transverse modes

Quantity	Unit	Symbol	Expression
Free spectral range	frequency	FSR	$\mathcal{F}\kappa = \dfrac{c}{L}$
Linewidth	frequency	κ	$\dfrac{\text{FSR}}{\mathcal{F}} = \dfrac{1-R}{\pi\sqrt{R}}\text{FSR}$
Finesse	unitless	$\mathcal{F}$	$\dfrac{\text{FSR}}{\kappa} = \dfrac{\pi\sqrt{R}}{1-R} \approx \dfrac{2\pi}{2T}$

Table 2.4: **Cavity parameters.** The expression for the FSR holds for an cavity, where c is the speed of light and L is the round trip cavity length. The expressions for the linewidth and finesse were derived explicitly in the context of a cavity comprised of two lossless mirrors, each with reflectivity R and transmittivity T.

Free spectral range

(1) **Theory.** The free spectral range is deeply intertwined with the concept of longitudinal cavity modes, the modes along the cavity axis. Longitudinal modes, or resonances, occur any time the phase of an electromagnetic wave returns to itself (modulo 2π) after one round trip through the cavity. In blunt terms, "the wave fits exactly inside the box." Mathematically, this resonance condition is

$$kL = 2\pi L/\lambda = 2\pi n \tag{2.102}$$

where n is an integer and $kL = 2\pi L/\lambda$ is the phase accrued by an electromagnetic wave after propagation through a distance L, which in this case is the round trip distance through the cavity. The free spectral range is the frequency difference between two adjacent longitudinal modes. Utilizing the common relationship $c = \lambda\nu$ and Equation 2.102 above,

$$\begin{aligned} \text{FSR} &= \nu_2 - \nu_1 && (2.103)\\ &= c\left(\frac{1}{\lambda_2} - \frac{1}{\lambda_1}\right) && (2.104)\\ &= c\left(\frac{n+1}{L} - \frac{n}{L}\right) && (2.105)\\ &= \frac{c}{L} && (2.106) \end{aligned}$$

For two-mirror cavities, you may see an expression like FSR $= \frac{c}{2d}$ instead, which is equivalent to the expression above. Often times, d will be defined as the cavity length in the two-mirror case because it is easy to physically measure. So, to acquire the round trip distance through the cavity (i.e. L), d needs to be multiplied by 2. Note also that the longitudinal modes of two-mirror cavities are *standing waves*, whereas the longitudinal modes of three or more mirror cavities are *running waves*, but can be operated in a standing wave fashion if necessary [31]. Just as standing waves can exist in free space by counterpropagating two laser beams, standing wave modes exist in a two-mirror cavity because the "right" traveling waves interfere with the "left" traveling waves. In a three or more mirror cavity, there is only either "right" or "left" traveling waves unless one explicitly excites both directions by sending two laser beams into the

cavity such that they counterpropagate inside. However, running wave cavities are advantageous in that running waves do not create intracavity intensity gradients as in the case of standing wave cavities—a favorable feature if you are trying to uniformly illuminate a cloud of atoms in the cavity, for example.

(2) **Experiment.** How do I find the FSR of my real life cavity?

- **Measure the cavity length.**

  Literally, take a ruler, measure the round trip distance by holding it up to the cavity, then plug this distance in for L in Equation 2.106. This method isn't the world's best measure of the FSR, but it should provide a decent estimate.

- **Estimate by tuning the laser.**

  This method assumes a laser is aligned to the cavity, there is a measure of the cavity output (e.g. spectra or imaging), the laser frequency is tunable via either temperature or current, and there is a measure of how the laser frequency changes with temperature or current (e.g. from a laser spec sheet). Identify some obvious mode in your measure of the cavity output (the fundamental Gaussian mode is usually a good choice), then tune the laser via either temperature or current until that same mode appears again, note the temperature or current change, then map that change to a frequency using your laser spec sheet.

  More specifically, let's say you initially sweep the laser current, and therefore frequency, repeatedly to view the cavity spectra using a photodiode and oscilloscope. If the laser is not very well aligned to any one particular cavity mode, there are probably a lot of different Lorentzian peaks which correspond to the cavity's various modes that you happen to be exciting. Tweak the alignment of the laser to the cavity until one mode is fairly distinguishable (e.g. its Lorentzian peak is by far the tallest), then tweak the current sweep to center your chosen

mode on a definitive marking on the oscilloscope screen. It may be the case that changing the overall current level will not change the frequency enough to bring your chosen mode of the next FSR into view, so let's say you choose to change the laser temperature—which typically has a larger impact on the frequency change—without changing the current sweep. So, the laser frequency will be locally sweeping due to the current, but the center frequency of this sweep will change due to the temperature. Once you change the laser temperature, the peaks on the oscilloscope screen will move as a result of the laser's center frequency changing. After some amount of temperature tuning, a mode that looks like your original chosen mode should appear of the oscilloscope screen—this is your chosen mode, but of the next FSR over! Tune the temperature such that this mode is centered on the definitive marking on the oscilloscope screen you chose earlier. Record the temperature change, map the temperature change to a frequency change, and the frequency change is the FSR. Words of caution: (1) make sure temperature tuning won't damage your laser (e.g. if you reduce the temperature, make sure it doesn't dip below the dew point. Otherwise, water will condense on the laser!), (2) the laser frequency can be sensitive to temperature tuning, so go easy on turning temperature knobs, and (3) it is possible the laser will "mode hop," or jump in frequency, while being temperature tuned. If this happens, I leave it to you to debug. Have fun!

- **Use a frequency ruler in the cavity spectra.**

  This method also assumes a laser is aligned to the cavity, there is a measure of the cavity spectra across at least one full FSR, and there is a way to modulate the laser frequency (e.g. via current modulation or using an electro-optic modulator). If you frequency modulate the laser, frequency sidebands should appear on either side of every mode in the cavity spectra which you can use as a "frequency ruler."

In other words, if you modulate the laser by 10 MHz, then you know the "distance" between then first order sideband and the carrier is 10 MHz in the spectra. Save an oscilloscope trace that contains your frequency-modulated modes across a full FSR, taking note which two Lorentzian peaks correspond with one FSR (e.g. the fundamental Gaussian of one FSR and the fundamental Gaussian of the next FSR; it may be difficult to tell which peak in the spectra corresponds with the fundamental Gaussian without imaging the cavity output, but it is usually the peak that is the tallest if the laser is well-aligned to the cavity). Read the trace into your favorite analysis software (e.g. Mathematica, Python), fit the two peaks that correspond with one FSR and at least one sideband of one of these peaks with a Lorentzian function, and extract the distances between (1) the two peaks that correspond with one FSR, and (2) a sideband and carrier. Note that these distances will be in "oscilloscope units" that are not particularly meaningful. However, the "distance" in *frequency* between a sideband and carrier is the modulation frequency you selected earlier. Thus, you can find how "oscilloscope units" transform to meaningful frequency units, then transform the distance between the two peaks that correspond with one FSR from "oscilloscope units" to frequency units. The transformed distance in frequency units is the FSR.

Linewidth

(1) **Theory.** Typically represented by κ in angular frequency units, the linewidth of a cavity is the FWHM of the cavity's transmission function and a measure of the lifetime of photons inside the cavity. In other words, $1/\kappa$ is the lifetime of photon in the cavity before it is transmitted through a cavity mirror. In order to find the expression for the cavity transmission, we consider a two-mirror cavity of length d. We assume the first (second) mirror has reflection coefficient r_1 (r_2) and transmission coefficient t_1 (t_2).

These coefficients quantify the fraction of the electric *field* (not intensity) that reflects off and transmits through the mirrors. We additionally assume some intracavity loss medium with coefficient l, which quantifies the fraction of the field that passes through the medium. We can now write down a system of self-consistent equations to solve for the reflected field off the cavity E_R, the left circulating field inside the cavity E_{CL}, the right circulating field inside the cavity E_{CR}, and the transmitted field through the cavity E_T, assuming some laser drive with amplitude E_0 and wave number $k = 2\pi/\lambda$:

$$E_{CR} = E_0 t_1 l e^{ikd} + E_{CL} r_1 l e^{ikd} \tag{2.107}$$

$$E_{CL} = E_{CR} r_2 l e^{ikd} \tag{2.108}$$

$$E_R = -E_0 r_1 + E_{CL} t_1 \tag{2.109}$$

$$E_T = E_{CR} t_2 \tag{2.110}$$

where e^{ikd} is the phase accrued by propagation through the cavity length. The three equations above contain three unknown variables (E_R, E_C, and E_T). Thus, we can solve for these three unknown variables, such as in Mathematica, yielding the solutions

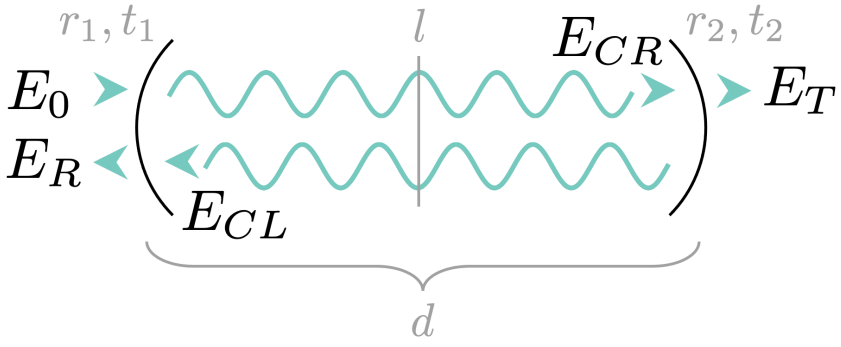

Figure 2.3: **Fields in a two-mirror cavity.** We can solve for the reflected field E_R, transmitted field E_T, right circulating field E_{CR}, and left circulating field E_{CL} given some laser drive with amplitude E_0. Remember, the locations where all of these fields are defined matter!

$$E_{CR} = E_0 \frac{t_1 l e^{ikd}}{1 - r_1 r_2 l^2 e^{2ikd}} \tag{2.111}$$

$$E_{CL} = E_0 \frac{r_2 t_1 l^2 e^{2ikd}}{1 - r_1 r_2 l^2 e^{2ikd}} \tag{2.112}$$

$$E_R = E_0 \left(\frac{r_2 t_1^2 l^2 e^{2ikd}}{1 - r_1 r_2 l^2 e^{2ikd}} - r_1 \right) \tag{2.113}$$

$$E_T = E_0 \frac{t_1 t_2 l e^{ikd}}{1 - r_1 r_2 l^2 e^{2ikd}} \tag{2.114}$$

Note that you can utilize the method above to solve for the reflected, circulating, and transmitted fields in general for cavities, but it is imperative that you (1) explicitly define positions for where each field will be calculated (e.g. the left circulating field is defined immediately to the right of the left mirror), and (2) obey the beam splitter relations, which can flip the sign of some reflection coefficients (as in the case of Equation 2.109 where r_1 is negative). Some sources [32, 33] will instead derive the reflected, circulating, and transmitted fields from infinite sums of electric field components, but I personally think the method above is more straightforward especially when dealing with complicated cavity designs. We can now derive the cavity transmission function in terms of intensities, where $I \propto |E|^2$:

$$\frac{I_T}{I_0} = \frac{|E_T|^2}{|E_0|^2} = \frac{(t_1 t_2 l)^2}{1 - 2r_1 r_2 l^2 \cos(2kd) + (r_1 r_2 l^2)^2} \tag{2.115}$$

$$= \frac{(t_1 t_2 l)^2}{1 - 2r_1 r_2 l^2 (1 - 2\sin^2(kd)) + (r_1 r_2 l^2)^2} \tag{2.116}$$

$$= \frac{(t_1 t_2 l)^2}{(1 - r_1 r_2 l^2)^2} \frac{1}{1 + \frac{4 r_1 r_2 l^2}{(1 - r_1 r_2 l^2)^2} \sin^2(kd)} \tag{2.117}$$

$$= \frac{T_1 T_2 L}{(1 - \sqrt{R_1 R_2} L)^2} \frac{1}{1 + \frac{4\sqrt{R_1 R_2} L}{(1 - \sqrt{R_1 R_2} L)^2} \sin^2(kd)} \tag{2.118}$$

where $T_1 = t_1^2$, $T_2 = t_2^2$, $R_1 = r_1^2$, $R_2 = r_2^2$, $R_1 + T_1 = 1$, $R_2 + T_2 = 1$, and $L = l^2$. This function is half its maximum value when

$$\frac{1}{1 + \frac{4\sqrt{R_1 R_2} L}{(1 - \sqrt{R_1 R_2} L)^2} \sin^2(kd)} = \frac{1}{2} \tag{2.119}$$

$$\downarrow \tag{2.120}$$

$$kd = \arcsin \sqrt{\frac{(1 - \sqrt{R_1 R_2} L)^2}{4\sqrt{R_1 R_2} L}} \tag{2.121}$$

Thus, the FWHM of the cavity transmission function is twice the value above. Maxima of the transmission function occur every time $\sin^2(kd) = 0$. Thus, the phase between maxima is $kd = \pi$, corresponding with one FSR in frequency. Combining Equation 2.121 with this fact, we can acquire the cavity linewidth κ in frequency:

$$\kappa = 2 \arcsin \sqrt{\frac{(1 - \sqrt{R_1 R_2} L)^2}{4\sqrt{R_1 R_2} L}} \frac{\mathrm{FSR}}{\pi} \tag{2.122}$$

which, if we assume no loss ($L = 1$), equal mirror reflectivities ($R_1 = R_2 = R$), and highly reflective mirrors ($R \approx 1$),

$$\kappa = 2 \arcsin \sqrt{\frac{(1-R)^2}{4R}} \frac{\mathrm{FSR}}{\pi} \tag{2.123}$$

$$\approx 2 \sqrt{\frac{(1-R)^2}{4R}} \frac{\mathrm{FSR}}{\pi} \tag{2.124}$$

$$= \frac{1-R}{\pi\sqrt{R}} \mathrm{FSR} \tag{2.125}$$

(2) **Experiment.** How do I find the linewidth of my real life cavity?

- **Use a frequency ruler in the cavity spectra.**

  This method is similar to a method used for measuring the FSR of a cavity. It assumes a laser is aligned to the cavity, there is a measure of the cavity spectra across at least one cavity mode, and there is a way to modulate the laser frequency to put first order sidebands on the cavity modes in the spectra. Let's say you modulate the laser, look at the cavity spectra on an oscilloscope, and see sidebands appear on either side of a cavity mode. Save an oscilloscope trace of the carrier and sidebands, read it into your favorite analysis software, and fit the three mode peaks with Lorentzian functions. The distance, in frequency, between a sideband and the carrier is the modulation frequency. Therefore, you know the transformation between distance in "oscilloscope units" to distance in frequency units. If you apply this transformation to the FWHM of one of the Lorentzian peaks in "oscilloscope units," you will acquire the cavity linewidth in frequency units. Note that the measured linewidth is actually a convolution of the laser linewidth with the cavity linewidth. So, if you measure the linewidth with a particularly broad laser or have constructed a particularly narrow cavity, you will likely need to deconvolve the two linewidths to attain the cavity linewidth.

Finesse

(1) **Theory.** The finesse of a cavity is a measure of how "lossy" it is, where "loss" includes transmission through cavity mirror(s), scattering or absorption via intracavity "junk," propagation at steep angles that causes light to literally "miss" mirror(s), and any other mechanism by which light exits the cavity. A high finesse is indicative of low loss, whereas a low finesse is indicative of high loss. For a cavity comprised of two mirrors of equal reflectivity R and loss via transmission T only, the finesse is defined as [32, 33]

$$\mathcal{F} = \frac{\text{FSR}}{\kappa} = \frac{\pi\sqrt{R}}{1-R} \tag{2.126}$$

Note that the finesse depends *only* on the reflective properties of the mirrors. For highly reflective mirrors ($R \approx 1$, $T \ll 1$), we can make a convenient approximation that is useful for remembering in the lab:

$$\mathcal{F} = \frac{\pi\sqrt{R}}{1-R} = \frac{\pi\sqrt{1-T}}{T} \approx \frac{\pi}{T} = \frac{2\pi}{2T} \tag{2.127}$$

In words, for highly reflective mirrors, the finesse can be approximated by 2π divided by the round trip loss! We approximated $\frac{\sqrt{1-T}}{T}$ as $\frac{1}{T}$ above by taking the first order of the Taylor series for $\frac{\sqrt{1-T}}{T}$ about $T = 0$.

(2) **Experiment.** How do I measure the finesse of my real life cavity?

- **Plug in mirror specs.**

  Literally, look at the spec sheet for the mirrors you'd like to use for your cavity, extract their reflectivities, and plug the reflectivities in to the formula for the finesse. The reflectivities quoted for mirrors will almost certainly be R (for intensities), not r (for fields). This method will provide you with an estimate for what finesse you should expect experimentally, but the experimental value may

be different in reality due to dust, differences in the quoted reflectivity, and so on.

- **Extract from the FSR and κ.**

  If you have measured the FSR and κ, you are essentially done! Plug these quantities into Equation 2.126 to acquire the finesse.

- **Ringdown.**

  This method assumes a laser is aligned to the cavity, there is a measure of the cavity spectra across one cavity mode, and there is a a way to sweep the cavity length over the cavity linewidth faster than it takes for light to escape. If you perform a sweep such as this (e.g. by ramping the voltage of a piezoelectric actuator that controls the cavity length), the transmission will no longer be Lorentzian. Instead, it will be a Lorentzian-like function that exhibits oscillations that decrease in magnitude on one side, or a "ringdown." The finesse can be extracted from the fit function for this ringdown, which can be found in Reference [34].

Transverse modes

(1) **Theory.** In addition to longitudinal modes along the cavity axis, there are modes perpendicular to the cavity axis called transverse modes [28]. These modes are characterized by differing electric field profiles as viewed in the transverse planes of a cavity (i.e. planes normal to the cavity axis). In other words, these are the modes you would see if you looked directly at a laser beam bouncing around a cavity—the beam might look like a typical Gaussian blob, a donut, or some other shape![16] These different shapes are different transverse modes. The transverse modes often occur at different frequencies as a result of the Gouy phase, an additional electric field phase that results from propagation through a focus (i.e. the waist(s) of a cavity). The Gouy phase is different for different transverse modes, resulting in non-degenerate transverse modes

16. Please do not look directly at a laser beam.

for most cavity geometries.[17] We will consider two main families of transverse modes often observed in cavities: Hermite-Gaussian modes and Laguerre-Gaussian modes.

- **Hermite-Gaussian modes.**

  The Hermite-Gaussian (HG) modes are the solutions to the paraxial Helmholtz equation as written in Cartesian coordinates:

$$\begin{aligned} E_{n,m}(x,y,z) =& E_0 \frac{\omega_0}{\omega(z)} H_n\left(\frac{\sqrt{2}x}{\omega(z)}\right) H_m\left(\frac{\sqrt{2}y}{\omega(z)}\right) \\ & \times \exp\left(-\frac{x^2+y^2}{\omega(z)^2}\right) \exp\left(-i\frac{k(x^2+y^2)}{2R(z)}\right) \exp(i\psi(z)) \exp(-ikz) \end{aligned} \tag{2.128}$$

  where the H_i terms are Hermite polynomial of order i, $\psi(z)$ is the Gouy phase, and indices n, m refer to the x and y directions, respectively. Here, the Gouy phase is

$$\psi(z) = (n+m+1)\arctan\left(\frac{z}{z_R}\right) \tag{2.129}$$

- **Laguerre-Gaussian modes.**

  The Laguerre-Gaussian (LG) modes are the solutions to the paraxial Helmholtz equation as written in cylindrical coordinates:

$$\begin{aligned} E_{l,p}(r,\phi,z) =& E_0 C_{lp}^{LG} \frac{\omega_0}{\omega(z)} \left(\frac{\sqrt{2}r}{\omega(z)}\right)^{|l|} L_p^{|l|}\left(\frac{2r^2}{\omega(z)^2}\right) \\ & \times \exp\left(-\frac{r^2}{\omega(z)^2}\right) \exp\left(-i\frac{kr^2}{2R(z)}\right) \exp(i\psi(z)) \exp(-il\phi) \end{aligned} \tag{2.130}$$

17. A main focus of the research presented later in this thesis is to create a cavity in which transverse modes *are* degenerate—a nontrivial task.

where L_p^l are the generalized Laguerre polynomials, C_{lp}^{LG} is a normalization constant, $\psi(z)$ is the Gouy phase, and indices l, p are the azimuthal index and radial index, respectively. l can be any integer whereas $p \geq 0$. The normalization constant is

$$C_{lp}^{LG} = \sqrt{\frac{2p!}{\pi(p+|l|)!}} \tag{2.131}$$

and here, the Gouy phase is

$$\psi(z) = (|l| + 2p + 1)\arctan\left(\frac{z}{z_R}\right) \tag{2.132}$$

While our resonance condition from Equation 2.102 still holds true for each individual transverse mode, we consider a slightly modified version of this condition to calculate the transverse mode frequencies relative to each other. For a two-mirror cavity of length d, the round trip phase change δ is [32]

$$\delta = 2kd - 2(\psi(z_2) - \psi(z_1)) = 2\pi q \tag{2.133}$$

where we have imposed the round trip phase change must be equal to $2\pi q$, where q is an integer, in order for a transverse mode to be resonant. z_1 and z_2 are the z coordinates of the first and second mirror, respectively, relative to the cavity waist. We can solve for the resonance frequencies of the transverse modes by plugging in the expression(s) for the Gouy phase and performing some simplifications.

For HG modes, the resonant frequencies of the transverse modes are

$$\nu_{nmq} = \left(q + (n+m+1)\frac{\arccos \pm\sqrt{g_1 g_2}}{\pi}\right)\frac{c}{2d} \tag{2.134}$$

For LG modes, the resonant frequencies of the transverse modes are

$$\nu_{lpq} = \left(q + (|l| + p + 1) \frac{\arccos \pm \sqrt{g_1 g_2}}{\pi} \right) \frac{c}{2d} \tag{2.135}$$

In both Equations 2.134 and 2.135 above, $g_1 = 1 - \frac{d}{R_1}$, $g_2 = 1 - \frac{d}{R_2}$, the positive sign is taken when $g_1, g_2 > 0$, and the negative sign is taken when $g_1, g_2 < 0$. Note that there are many frequencies in which a given transverse mode can occur, and these frequencies are separated by $\frac{c}{2d}$, or one FSR.

(2) **Experiment.** How do I find the transverse modes of my real life cavity?

- **Combine imaging and spectra.**

  This method assumes a laser is aligned to the cavity, the laser frequency is both tunable and sweepable, and the cavity output is sent to both a photodiode (to observe spectra) and a camera (to observe the intensity profile of the output). To identify which transverse mode a peak corresponds to in the spectra, tune the laser frequency such that your selected peak in the spectra is the only peak the laser sweeps over in frequency. As the laser sweeps over this peak, look at the camera output on a monitor or computer. The transverse modes are fairly distinct from one another, so you should be able to tell which transverse mode it is just by the shape of the intensity profile! If instead you are interested in measuring the transverse mode spacing in frequency, use the aforementioned method to first identify the modes in the spectra, then use the "frequency ruler" trick mentioned in previous parts of this subsection to acquire a frequency metric for spectra measurements.

CHAPTER 3

CAVITY QUANTUM ELECTRODYNAMICS

3.1 Quantum materials and cavity QED

In Chapter 2, we discussed atoms and cavities separately. Now, we are going to discuss atoms *in* cavities, or cavity quantum electrodynamics (also known as "cavity QED" or "cQED") [35]! When combined, atoms and cavities offer the essential ingredients for constructing quantum materials [36] made of light. Atoms offer their tunable interactions, and cavities offer their ability to shape the energy landscape, or dispersion, of photons. Together, these ingredients can be harnessed to create entangled photonic states, or quantum materials, that exhibit strong correlations in time and space as we will see in Chapter 5.

This chapter will overview the theory behind atoms in cavities and how we can utilize it to extract experimentally relevant information.

3.2 Common systems

3.2.1 A single two-level atom in a single mode cavity

This subsection will consider a single two-level atom in a single mode cavity. We will call the two levels of the atom the "ground state" $|g\rangle$ with energy $\hbar\omega_g$ and the "excited state" $|e\rangle$ with energy $\hbar\omega_e$. Remember, $|g\rangle$ and $|e\rangle$ are really spatial electronic wavefunctions, the ones discussed in Subsection 2.1.1, for some states we have called the ground and excited state here. In practice $|g\rangle$ and $|e\rangle$ might be the $5S_{1/2}$ and $5P_{3/2}$ states of ^{87}Rb, respectively (which is almost always the case for the work presented in this thesis). The cavity can host some number of photons n in a single mode, corresponding with the photon state $|n\rangle$. In other words, $|0\rangle$ means there are no photons in the cavity, $|1\rangle$ means there is one photon in the cavity, and so on. Photons are created with the creation operator $a^\dagger$ and annihilated with

the annihilation operator a. We will call the energy of this single cavity mode $\hbar\omega_c$, where ω_c is the angular frequency that corresponds with a particular transverse and longitudinal mode, such as the fundamental Gaussian mode of some FSR.

As our system includes an atom, a cavity, and some interaction between the atom and cavity photons, the full system Hamiltonian is the sum of the atomic Hamiltonian, cavity Hamiltonian, interaction Hamiltonian, and a drive Hamiltonian [37] with strength $\hbar\Omega_l$ and frequency ω_l.

$$H = H_{atom} + H_{cav} + H_{int} + H_{drive} \tag{3.1}$$

where

$$H_{atom} = \hbar\omega_g |g\rangle \langle g| + \hbar\omega_e |e\rangle \langle e| \tag{3.2}$$

$$H_{cav} = \hbar\omega_c a^\dagger a \tag{3.3}$$

$$H_{int} = e\mathbf{r} \cdot \mathbf{E} \tag{3.4}$$

$$H_{drive} = \hbar\Omega_l (e^{-i\omega_l t} a^\dagger + e^{i\omega_l t} a) \tag{3.5}$$

where H_{int} may look familiar from Subsection 2.1.3 when we discussed Stark effects. Physically, the drive Hamiltonian usually corresponds to some laser of frequency ω_l that probes the system. Without a drive, our system is stuck at 0 photons! Typically, this drive is very weak and is often thought of as a perturbation to the full system Hamiltonian rather than included in the full system Hamiltonian as we will see later in this chapter. However, the drive must be included in the full system Hamiltonian when solving for the full time dynamics of the system, which is why we will keep it around for now. We can write H_{int} more explicitly in terms of states and operators as

$$H_{int} = e(|g\rangle\langle g|\,\mathbf{r}\,|g\rangle\langle g| + |g\rangle\langle g|\,\mathbf{r}\,|e\rangle\langle e| + |e\rangle\langle e|\,\mathbf{r}\,|g\rangle\langle g| + |e\rangle\langle e|\,\mathbf{r}\,|e\rangle\langle e|) \cdot \hat{\mathbf{e}}E_0(a^\dagger + a) \tag{3.6}$$

where we have utilized completeness to write $\mathbf{r}$ in terms of the atomic states. However, $\langle g|\,\mathbf{r}\,|g\rangle = 0$ and $\langle e|\,\mathbf{r}\,|e\rangle = 0$ as these are integrals over odd functions of r. Thus, H_{int} simplifies to

$$\begin{aligned} H_{int} = {} & |g\rangle\langle e|\langle g|\,e\mathbf{r}\cdot\hat{\mathbf{e}}E_0\,|e\rangle\,a^\dagger \\ & + |g\rangle\langle e|\langle g|\,e\mathbf{r}\cdot\hat{\mathbf{e}}E_0\,|e\rangle\,a \\ & + |e\rangle\langle g|\langle e|\,e\mathbf{r}\cdot\hat{\mathbf{e}}E_0\,|g\rangle\,a^\dagger \\ & + |e\rangle\langle g|\langle e|\,e\mathbf{r}\cdot\hat{\mathbf{e}}E_0\,|g\rangle\,a \end{aligned} \tag{3.7}$$

However, the second and third terms in the equation above violate the conservation of energy! So long as $\langle g|\,e\mathbf{r}\cdot\hat{\mathbf{e}}E_0\,|e\rangle = \langle e|\,e\mathbf{r}\cdot\hat{\mathbf{e}}E_0\,|g\rangle \ll (\hbar\omega_e - \hbar\omega_g)$, we can drop these terms and H_{int} becomes

$$H_{int} = |g\rangle\langle e|\langle g|\,e\mathbf{r}\cdot\hat{\mathbf{e}}E_0\,|e\rangle\,a^\dagger + |e\rangle\langle g|\langle e|\,e\mathbf{r}\cdot\hat{\mathbf{e}}E_0\,|g\rangle\,a \tag{3.8}$$

$$= \hbar g(|g\rangle\langle e|\,a^\dagger + |e\rangle\langle g|\,a) \tag{3.9}$$

where

$$g = \frac{\langle g|\,e\mathbf{r}\cdot\hat{\mathbf{e}}E_0\,|e\rangle}{\hbar} = \frac{\langle e|\,e\mathbf{r}\cdot\hat{\mathbf{e}}E_0\,|g\rangle}{\hbar} = \frac{\mathbf{d}\cdot\hat{\mathbf{e}}E_0}{\hbar} \tag{3.10}$$

E_0 is defined to be the electric field magnitude at the location of the atom due to a single

cavity photon, and $\mathbf{d}$ is the dipole matrix element between states $|g\rangle$ and $|e\rangle$. Now we can write out the full system Hamiltonian with our newly simplified H_{int}:

$$\begin{aligned} H &= \hbar\omega_g \left|g\right\rangle \left\langle g\right| + \hbar\omega_e \left|e\right\rangle \left\langle e\right| \\ &+ \hbar\omega_c a^\dagger a \\ &+ \hbar g(\left|g\right\rangle \left\langle e\right| a^\dagger + \left|e\right\rangle \left\langle g\right| a) \\ &+ \hbar\Omega_l(e^{-i\omega_l t}a^\dagger + e^{i\omega_l t}a) \end{aligned} \tag{3.11}$$

To simplify this Hamiltonian even further, we will set the ground state energy ω_g to zero. To include the real world effects of decay, we will incorporate two imaginary loss terms: one that depends on Γ, the excited atomic state decay rate, and one that depends on κ, the cavity decay rate. Now,

$$\begin{aligned} H &= \hbar(\omega_e - \frac{i\Gamma}{2}) \left|e\right\rangle \left\langle e\right| \\ &+ \hbar(\omega_c - \frac{i\kappa}{2})a^\dagger a \\ &+ \hbar g(\left|g\right\rangle \left\langle e\right| a^\dagger + \left|e\right\rangle \left\langle g\right| a) \\ &+ \hbar\Omega_l(e^{-i\omega_l t}a^\dagger + e^{i\omega_l t}a) \end{aligned} \tag{3.12}$$

We can write the full Hamiltonian in matrix form by utilizing the $|atom\rangle \otimes |cavity\rangle$ states of our system, where $|g\rangle \otimes |1\rangle = |g1\rangle$ is the state where the atom is in the ground state and there is one photon in the cavity, for example.

If we consider only the states that contain up to *one* excitation, or the states that can result from up to one photon bouncing around the atom-cavity system, only the states $|g0\rangle$, $|g1\rangle$, and $|e0\rangle$ are relevant. This collection of one-excitation states is called the first excitation manifold.

If we consider only the states that contain up to *two* excitations, or the states that can result from up to two photons bouncing around the atom-cavity system, then we must include the additional states $|g2\rangle$ and $|e1\rangle$. This collection of two-excitation states is called the second excitation manifold.

If we consider only the states that contain up to *three* excitations... wait, how many excitations do we actually need to consider theoretically? The number of excitations could go on forever! Fortunately, there is a good rule of thumb, and it depends on what you are interested in measuring experimentally. If you are interested in measuring the transmission of photons through a cavity that you probe weakly with a laser, you need only consider one photon. However, if you are interested in measuring quantities that depend on two or more photons like temporal correlations, then you must utilize the full system Hamiltonian that considers states with two or more excitations.

We will write down the full system Hamiltonian in matrix form considering states that contain up to *two* excitations, as the work presented later in this thesis does not extend beyond two-photon correlations. In matrix form, the full Hamiltonian is

$$H = \begin{pmatrix} \langle g0| H |g0\rangle & \langle g0| H |g1\rangle & \langle g0| H |e0\rangle & \langle g0| H |g2\rangle & \langle g0| H |e1\rangle \\ \langle g1| H |g0\rangle & \langle g1| H |g1\rangle & \langle g1| H |e0\rangle & \langle g1| H |g2\rangle & \langle g1| H |e1\rangle \\ \langle e0| H |g0\rangle & \langle e0| H |g1\rangle & \langle e0| H |e0\rangle & \langle e0| H |g2\rangle & \langle e0| H |e1\rangle \\ \langle g2| H |g0\rangle & \langle g2| H |g1\rangle & \langle g2| H |e0\rangle & \langle g2| H |g2\rangle & \langle g2| H |e1\rangle \\ \langle e1| H |g0\rangle & \langle e1| H |g1\rangle & \langle e1| H |e0\rangle & \langle e1| H |g2\rangle & \langle e1| H |e1\rangle \end{pmatrix} \tag{3.13}$$

Plugging in the full system Hamiltonian H from Equation 3.12, we acquire

$$H = \hbar \begin{pmatrix} 0 & \Omega_l e^{i\omega_l t} & 0 & 0 & 0 \\ \Omega_l e^{-i\omega_l t} & \omega_c - \frac{i\kappa}{2} & g & \sqrt{2}\Omega_l e^{i\omega_l t} & 0 \\ 0 & g & \omega_e - \frac{i\Gamma}{2} & 0 & \Omega_l e^{i\omega_l t} \\ 0 & \sqrt{2}\Omega_l e^{-i\omega_l t} & 0 & 2(\omega_c - \frac{i\kappa}{2}) & \sqrt{2}g \\ 0 & 0 & \Omega_l e^{-i\omega_l t} & \sqrt{2}g & (\omega_c - \frac{i\kappa}{2}) + (\omega_e - \frac{i\Gamma}{2}) \end{pmatrix} \tag{3.14}$$

For those who wish to consider H_{drive} as a perturbation, it is useful to split the Hamiltonian above into its unperturbed constituent H_0 (given by $H_{atom}+H_{cav}+H_{int}$) and its perturbative constituent V (given by H_{drive}) such that $H = H_0 + V$.

$$H_0 = \hbar \begin{pmatrix} 0 & 0 & 0 & 0 & 0 \\ 0 & \omega_c - \frac{i\kappa}{2} & g & 0 & 0 \\ 0 & g & \omega_e - \frac{i\Gamma}{2} & 0 & 0 \\ 0 & 0 & 0 & 2(\omega_c - \frac{i\kappa}{2}) & \sqrt{2}g \\ 0 & 0 & 0 & \sqrt{2}g & (\omega_c - \frac{i\kappa}{2}) + (\omega_e - \frac{i\Gamma}{2}) \end{pmatrix} \tag{3.15}$$

$$V = \hbar \begin{pmatrix} 0 & \Omega_l e^{i\omega_l t} & 0 & 0 & 0 \\ \Omega_l e^{-i\omega_l t} & 0 & 0 & \sqrt{2}\Omega_l e^{i\omega_l t} & 0 \\ 0 & 0 & 0 & 0 & \Omega_l e^{i\omega_l t} \\ 0 & \sqrt{2}\Omega_l e^{-i\omega_l t} & 0 & 0 & 0 \\ 0 & 0 & \Omega_l e^{-i\omega_l t} & 0 & 0 \end{pmatrix} \tag{3.16}$$

We can eliminate the time dependence using a unitary transformation as we did in Subsection 2.1.3. We will make an educated guess for the correct transformation matrix. Educated guesses do not work so well for more complicated systems, as we will discuss later, but here

we will use the unitary transformation matrix

$$U = \begin{pmatrix} 1 & 0 & 0 & 0 & 0 \\ 0 & e^{i\omega_l t} & 0 & 0 & 0 \\ 0 & 0 & e^{i\omega_l t} & 0 & 0 \\ 0 & 0 & 0 & e^{i2\omega_l t} & 0 \\ 0 & 0 & 0 & 0 & e^{i2\omega_l t} \end{pmatrix} \tag{3.17}$$

After punching this transformation matrix and Hamiltonian into Mathematica, we compute our transformed Hamiltonian to be

$$H' = UHU^\dagger + i\hbar \frac{\partial U}{\partial t} U^\dagger \tag{3.18}$$

$$= \hbar \begin{pmatrix} 0 & \Omega_l & 0 & 0 & 0 \\ \Omega_l & \omega_c - \omega_l - \frac{i\kappa}{2} & g & \sqrt{2}\Omega_l & 0 \\ 0 & g & \omega_e - \omega_l - \frac{i\Gamma}{2} & 0 & \Omega_l \\ 0 & \sqrt{2}\Omega_l & 0 & 2(\omega_c - \omega_l - \frac{i\kappa}{2}) & \sqrt{2}g \\ 0 & 0 & \Omega_l & \sqrt{2}g & (\omega_c - \omega_l - \frac{i\kappa}{2}) + (\omega_e - \omega_l - \frac{i\Gamma}{2}) \end{pmatrix} \tag{3.19}$$

where

$$H_0' = \hbar \begin{pmatrix} 0 & 0 & 0 & 0 & 0 \\ 0 & \omega_c - \omega_l - \frac{i\kappa}{2} & g & 0 & 0 \\ 0 & g & \omega_e - \omega_l - \frac{i\Gamma}{2} & 0 & 0 \\ 0 & 0 & 0 & 2(\omega_c - \omega_l - \frac{i\kappa}{2}) & \sqrt{2}g \\ 0 & 0 & 0 & \sqrt{2}g & (\omega_c - \omega_l - \frac{i\kappa}{2}) + (\omega_e - \omega_l - \frac{i\Gamma}{2}) \end{pmatrix} \tag{3.20}$$

$$V' = \hbar \begin{pmatrix} 0 & \Omega_l & 0 & 0 & 0 \\ \Omega_l & 0 & 0 & \sqrt{2}\Omega_l & 0 \\ 0 & 0 & 0 & 0 & \Omega_l \\ 0 & \sqrt{2}\Omega_l & 0 & 0 & 0 \\ 0 & 0 & \Omega_l & 0 & 0 \end{pmatrix} \tag{3.21}$$

If you care only about the states that contain up to one excitation, then you need only utilize the upper left 3x3 portion of Equation 3.19. In fact, it is also not uncommon to utilize only a 2x2 portion of Equation 3.19 when carrying out transmission calculations using non-Hermitian perturbation theory as we will see later in this chapter.

3.2.2 N two-level atoms in a single mode cavity (VRS)

This subsection will consider N two-level atoms in a single mode cavity. Fortunately, we can just steal the Hamiltonian from the previous subsection and modify it a bit to now sum over N atoms instead of one and eliminate the time dependence that we already know can be transformed away from Equation 3.19:

$$
\begin{aligned}
H = &\sum_{m}^{N} \hbar(\omega_e - \omega_l - \frac{i\Gamma}{2}) \left|e\right\rangle_m \left\langle e\right|_m \\
&+ \hbar(\omega_c - \omega_l - \frac{i\kappa}{2}) a^\dagger a \\
&+ \sum_{m}^{N} \hbar g_m (\left|g\right\rangle_m \left\langle e\right|_m a^\dagger + \left|e\right\rangle_m \left\langle g\right|_m a) \\
&+ \hbar\Omega_l (a^\dagger + a)
\end{aligned}
\tag{3.22}
$$

Assuming some reasonable number of atoms that we deal with in the lab (on the scale of hundreds to thousands), writing the full matrix form of the Hamiltonian above out by hand can become horrifically large as just the first excitation manifold alone contains all the $|atom\rangle \otimes |cavity\rangle$ states $|gggg...1\rangle$, $|eggg...0\rangle$, $|gegg...0\rangle$, $|ggeg...0\rangle$, and so on for N atoms.

However, we can simplify the Hamiltonian above by first considering the two-atom case. Up to the first excitation manifold, the states we have at our disposal are $|gg0\rangle$, $|gg1\rangle$, $|eg0\rangle$, and $|ge0\rangle$. We know the time evolution operator for some arbitrary state is e^{-iHt}, which Taylor expands as $\sum_n^\infty \frac{(-it)^n (H^n)}{n!}$. So, we should be able to determine which states we *actually* need to consider by repeatedly applying H to our initial state, $|gg0\rangle$, and seeing which states result [38]. The Hamiltonian for two atoms is

$$
\begin{aligned}
H = &\hbar(\omega_e - \omega_l - \frac{i\Gamma}{2})(\left|e\right\rangle_1 \left\langle e\right|_1 + \left|e\right\rangle_2 \left\langle e\right|_2) \\
&+ \hbar(\omega_c - \omega_l - \frac{i\kappa}{2}) a^\dagger a \\
&+ \hbar g_1 (\left|g\right\rangle_1 \left\langle e\right|_1 a^\dagger + \left|e\right\rangle_1 \left\langle g\right|_1 a) + \hbar g_2 (\left|g\right\rangle_2 \left\langle e\right|_2 a^\dagger + \left|e\right\rangle_2 \left\langle g\right|_2 a) \\
&+ \hbar\Omega_l (a^\dagger + a)
\end{aligned}
\tag{3.23}
$$

Applying H above to the state $|gg0\rangle$, we acquire the state $|gg1\rangle$ as a "relevant" state after normalization:

$$H\,|gg0\rangle = \hbar\Omega_l\,|gg1\rangle \rightarrow |gg1\rangle \tag{3.24}$$

Great! Now let's continue this procedure, while carrying out Gram-Schmidt orthogonalization (intuitively, to "filter out" the states we have already found) and normalization to find the set of normalized states that are relevant for our calculations:

$$\begin{aligned} H\,|gg1\rangle &= \hbar\Omega_l\,|gg0\rangle + \hbar(\omega_c - \omega_l - \frac{i\kappa}{2})\,|gg1\rangle + \hbar g_1\,|eg0\rangle + \hbar g_2\,|ge0\rangle \\ &\rightarrow \frac{g_1\,|eg0\rangle + g_2\,|ge0\rangle}{\sqrt{g_1^2+g_2^2}} \end{aligned} \tag{3.25}$$

$$\begin{aligned} H\frac{g_1\,|eg0\rangle + g_2\,|ge0\rangle}{\sqrt{g_1^2+g_2^2}} &= \hbar(\omega_e - \omega_l - \frac{i\Gamma}{2})\frac{g_1}{\sqrt{g_1^2+g_2^2}}\,|eg0\rangle \\ &+ \hbar(\omega_e - \omega_l - \frac{i\Gamma}{2})\frac{g_2}{\sqrt{g_1^2+g_2^2}}\,|ge0\rangle \\ &+ \frac{\hbar g_1^2}{\sqrt{g_1^2+g_2^2}}\,|gg1\rangle + \frac{\hbar g_2^2}{\sqrt{g_1^2+g_2^2}}\,|gg1\rangle \\ &\rightarrow \text{no new states!} \end{aligned} \tag{3.26}$$

We have now found our set of relevant states: $|gg0\rangle$, $|gg1\rangle$, and $\frac{g_1|eg0\rangle+g_2|ge0\rangle}{\sqrt{g_1^2+g_2^2}}$. We say these states are written in the "coupled basis," whereas our original set of states, $|gg0\rangle$, $|gg1\rangle$, $|eg0\rangle$, and $|ge0\rangle$, are written in the "uncoupled basis." You can write down the full system Hamiltonian in matrix form using either of these bases, but there will be far fewer coupled basis states than uncoupled basis states as the atom number N increases. The coupled basis state $\frac{g_1|eg0\rangle+g_2|ge0\rangle}{\sqrt{g_1^2+g_2^2}}$ is one we refer to as a "collective state," in which the collective of atoms "share" an excitation.

Extending this collective state language to N atoms, we can now simplify the Hamiltonian

in Equation 3.22 by introducing the collective state operator

$$E^\dagger = \frac{1}{\sqrt{\sum_m^N g_m^2}} \sum_m^N g_m \left|e\right\rangle_m \left\langle g\right|_m \tag{3.27}$$

which creates a collective excited state when acted on the state $|gggg...0\rangle$. We will use this operator to essentially rewrite the Hamiltonian of Equation 3.22 in the context of collective states, yielding

$$\begin{aligned} H &= \hbar(\omega_e - \omega_l - \frac{i\Gamma}{2})E^\dagger E \\ &+ \hbar(\omega_c - \omega_l - \frac{i\kappa}{2})a^\dagger a \\ &+ \hbar\sqrt{\sum_m^N g_m^2}(Ea^\dagger + E^\dagger a) \\ &+ \hbar\Omega_l(a^\dagger + a) \end{aligned} \tag{3.28}$$

Note that we have not just substituted the collective state operator into Equation 3.22 to acquire the Hamiltonian above. Rather, we have performed a partial diagonalization to essentially make our Hamiltonian operate only on the coupled basis states we have deemed relevant, which for N atoms are $|gggg...0\rangle$, $|gggg...1\rangle$, and the collective state $\frac{1}{\sqrt{g_1^2+g_2^2+g_3^2+...}}(g_1 \left|eggg...0\right\rangle + g_2 \left|gegg...0\right\rangle + g_3 \left|ggeg...0\right\rangle + ...)$.

If we can assume most atoms "see" the same electric field (for example, if they are localized near the center of a relatively large laser beam), then we can assume $g_m = g$ for all atoms and the Hamiltonian further simplifies to

$$
\begin{aligned}
H = &\hbar(\omega_e - \omega_l - \frac{i\Gamma}{2})E^\dagger E \\
&+ \hbar(\omega_c - \omega_l - \frac{i\kappa}{2})a^\dagger a \\
&+ \hbar g\sqrt{N}(Ea^\dagger + E^\dagger a) \\
&+ \hbar\Omega_l(a^\dagger + a)
\end{aligned}
\tag{3.29}
$$

Using the coupled basis states for N atoms, which are now $|gggg...0\rangle$, $|gggg...1\rangle$, and the collective state $\frac{1}{\sqrt{N}}(|eggg...0\rangle + |gegg...0\rangle + |ggeg...0\rangle + ...)$ for $g_m = g$, the Hamiltonian above can be written in matrix form up to the first excitation manifold as

$$
H = \hbar \begin{pmatrix} 0 & \Omega_l & 0 \\ \Omega_l & \omega_c - \omega_l - \frac{i\kappa}{2} & g\sqrt{N} \\ 0 & g\sqrt{N} & \omega_e - \omega_l - \frac{i\Gamma}{2} \end{pmatrix}
\tag{3.30}
$$

The matrix above is demonstrative of the power of collective states. In the uncoupled basis, the size of our Hamiltonian in matrix form would have been $(N+2) \times (N+2)$. In the coupled basis, the size of our Hamiltonian in matrix form is 3x3 (the matrix in Equation 3.30 above), yet it encompasses the physics of N atoms! If anybody ever asks you "what's your G?" or "what's big G?," they are likely referring to the coupling $g\sqrt{N}$, the collectively enhanced coupling between the cavity and atomic states, as opposed to the single atom coupling g.

If the electric field "seen" by the atoms is non-uniform, you *cannot* assume $g_m = g$ for all atoms as g_m depends on the electric field at the location of atom m. Particularly in multimode systems where different atoms can experience multiple different electric field profiles, take care to identify what the relevant collective states actually are. It may be the case that working in the uncoupled basis is easier for accommodating spatially-dependent couplings.

3.2.3 N three-level atoms in a single mode cavity (EIT)

This subsection will consider N three-level atoms in a single mode cavity, where we are now going to introduce the third atomic level $|r\rangle$ with energy $\hbar\omega_r$ and decay rate γ_r. Here, the third level "r" is suggestive of a "Rydberg" level, as it often is in the work presented in this thesis. We are once again going to steal a Hamiltonian from the previous subsection, Equation 3.22, and modify it to suit our current needs. We will add a third level for every atom and a coupling to that level:

$$\begin{aligned} H = &\sum_m^N \hbar(\omega_r - \omega_l - \frac{i\gamma_r}{2}) \left|r\right\rangle_m \left\langle r\right|_m \\ &+ \sum_m^N \hbar(\omega_e - \omega_l - \frac{i\Gamma}{2}) \left|e\right\rangle_m \left\langle e\right|_m \\ &+ \hbar(\omega_c - \omega_l - \frac{i\kappa}{2}) a^\dagger a \\ &+ \sum_m^N \hbar\Omega(\left|e\right\rangle_m \left\langle r\right|_m e^{i\omega_b t} + \left|r\right\rangle_m \left\langle e\right|_m e^{-i\omega_b t}) \\ &+ \sum_m^N \hbar g_m(\left|g\right\rangle_m \left\langle e\right|_m a^\dagger + \left|e\right\rangle_m \left\langle g\right|_m a) \\ &+ \hbar\Omega_l(a^\dagger + a) \end{aligned} \tag{3.31}$$

where in the Hamiltonian above, we have subtracted ω_l from ω_r from the get go as this would have happened in the unitary transformation to remove the time dependence from the drive term containing Ω_l. Ω is the Rabi frequency between the second and third atomic level, coupling $|e\rangle$ and $|r\rangle$. As the Rabi frequency depends on the electric field of the coupling light, which oscillates at some frequency ω_b, Ω can be increased by increasing the light intensity and is also associated with time dependence.

Now, how do we simplify the Hamiltonian above? Remember how we found the relevant coupled basis states for the two-atom case in the previous subsection? We found the collective

excited state to be $\frac{g_1|eg0\rangle+g_2|ge0\rangle}{\sqrt{g_1^2+g_2^2}}$. By acting the Hamiltonian above on this state, we unlock a new collective state: the collective Rydberg state $\frac{g_1|rg0\rangle+g_2|gr0\rangle}{\sqrt{g_1^2+g_2^2}}$ assuming Ω is the same for all atoms.[1] Extending this collective Rydberg state idea to N atoms, we introduce a new collective state operator

$$R^\dagger = \frac{1}{\sqrt{\sum_m^N g_m^2}} \sum_m^N g_m \left|r\right\rangle_m \left\langle g\right|_m \tag{3.32}$$

which creates a collective Rydberg state (or whatever third level you're dealing with) when acted on the state $|gggg...0\rangle$. Using this operator and $E^\dagger$ from the previous subsection, the new partially diagonalized Hamiltonian is

$$\begin{aligned} H &= \hbar(\omega_e - \omega_l - \frac{i\Gamma}{2})E^\dagger E + \hbar(\omega_r - \omega_l - \frac{i\gamma_r}{2})R^\dagger R \\ &+ \hbar(\omega_c - \omega_l - \frac{i\kappa}{2})a^\dagger a \\ &+ \hbar\sqrt{\sum_m^N g_m^2}(Ea^\dagger + E^\dagger a) + \hbar\Omega(E^\dagger R e^{i\omega_b t} + R^\dagger E e^{-i\omega_b t}) \\ &+ \hbar\Omega_l(a^\dagger + a) \end{aligned} \tag{3.33}$$

Once again, if we can assume $g_m = g$ for all atoms, the Hamiltonian above simplifies further to

1. What if Ω isn't the same for all atoms? Then, the collective Rydberg state would look something like $\Omega_1 g_1 \left|rg0\right\rangle + \Omega_2 g_2 \left|gr0\right\rangle$ up to a normalization factor. Upon acting the Hamiltonian on this state, we are taken to a *new* collective excited state proportional to $\Omega_1^2 g_1 \left|eg0\right\rangle + \Omega_2^2 g_2 \left|ge0\right\rangle$ instead of the collective excited state proportional to $g_1 \left|eg0\right\rangle + g_2 \left|ge0\right\rangle$ which we found initially. The upshot here is that if Ω isn't the same for all atoms, we end up with a mess of collective states that we have to consider and are not necessarily orthogonal to one another. For this reason, we experimentally chose to make the beam that couples $|e\rangle$ and $|r\rangle$ large so the atoms all roughly experience the same laser field and thus Ω.

$$
\begin{aligned}
H = & \hbar(\omega_e - \omega_l - \frac{i\Gamma}{2})E^\dagger E + \hbar(\omega_r - \omega_l - \frac{i\gamma_r}{2})R^\dagger R \\
& + \hbar(\omega_c - \omega_l - \frac{i\kappa}{2})a^\dagger a \\
& + \hbar g\sqrt{N}(Ea^\dagger + E^\dagger a) + \hbar\Omega(E^\dagger R e^{i\omega_b t} + R^\dagger E e^{-i\omega_b t}) \\
& + \hbar\Omega_l(a^\dagger + a)
\end{aligned}
\tag{3.34}
$$

Using the coupled basis states $|gggg...0\rangle$, $|gggg...1\rangle$, the collective excited state $\frac{1}{\sqrt{N}}(|eggg...0\rangle + |gegg...0\rangle + |ggeg...0\rangle + ...)$, and the collective Rydberg state $\frac{1}{\sqrt{N}}(|rggg...0\rangle + |grgg...0\rangle + |ggrg...0\rangle + ...)$, the Hamiltonian above can be written in matrix form up to the first excitation manifold as

$$
H = \hbar \begin{pmatrix}
0 & \Omega_l & 0 & 0 \\
\Omega_l & \omega_c - \omega_l - \frac{i\kappa}{2} & g\sqrt{N} & 0 \\
0 & g\sqrt{N} & \omega_e - \omega_l - \frac{i\Gamma}{2} & \Omega e^{i\omega_b t} \\
0 & 0 & \Omega e^{-i\omega_b t} & \omega_r - \omega_l - \frac{i\gamma_r}{2}
\end{pmatrix}
\tag{3.35}
$$

As in previous subsections, we will eliminate the time dependence in the Hamiltonian above using a unitary transformation:

$$
U = \hbar \begin{pmatrix}
1 & 0 & 0 & 0 \\
0 & 1 & 0 & 0 \\
0 & 0 & 1 & 0 \\
0 & 0 & 0 & e^{i\omega_b t}
\end{pmatrix}
\tag{3.36}
$$

The transformed Hamiltonian is

$$H' = \hbar \begin{pmatrix} 0 & \Omega_l & 0 & 0 \\ \Omega_l & \omega_c - \omega_l - \frac{i\kappa}{2} & g\sqrt{N} & 0 \\ 0 & g\sqrt{N} & \omega_e - \omega_l - \frac{i\Gamma}{2} & \Omega \\ 0 & 0 & \Omega & \omega_r - \omega_l - \omega_b - \frac{i\gamma_r}{2} \end{pmatrix} \tag{3.37}$$

and we're done! Note how there is no $\sqrt{N}$ enhancement on Ω as there is with g. Intuitively, when a photon that excites $|g\rangle$ to $|e\rangle$ is incident upon many atoms in the ground state, *any* atom could absorb it. However, when a photon that excites $|e\rangle$ to $|r\rangle$ is incident upon the atoms, there is only *one* atom in $|e\rangle$ even though we know not which one. Hence, g receives a $\sqrt{N}$ enhancement whereas Ω does not.

3.2.4 N three-level atoms in a multimode cavity

This subsection will consider N three-level atoms in a multimode cavity. We are now going to steal the Hamiltonian from Equation 3.22 in the previous subsection and modify it to include a sum over M cavity modes:

$$
\begin{aligned}
H = &\sum_{m}^{N} \hbar(\omega_r - \omega_l - \omega_b - \frac{i\gamma_r}{2}) \left|r\right\rangle_m \left\langle r\right|_m \\
&+ \sum_{m}^{N} \hbar(\omega_e - \omega_l - \frac{i\Gamma}{2}) \left|e\right\rangle_m \left\langle e\right|_m \\
&+ \sum_{n}^{M} \hbar(\omega_{c,n} - \omega_l - \frac{i\kappa}{2}) a_n^\dagger a_n \\
&+ \sum_{m}^{N} \hbar\Omega(\left|e\right\rangle_m \left\langle r\right|_m + \left|r\right\rangle_m \left\langle e\right|_m) \\
&+ \sum_{n}^{M} \sum_{m}^{N} \hbar g_{mn}(\left|g\right\rangle_m \left\langle e\right|_m a_n^\dagger + \left|e\right\rangle_m \left\langle g\right|_m a_n) \\
&+ \sum_{n}^{M} \hbar\Omega_{l,n}(a_n^\dagger + a_n)
\end{aligned}
\tag{3.38}
$$

where we have eliminated the time dependence attached to Ω by considering methods of the previous subsection. This Hamiltonian is pretty gnarly. Hypothetically, we can make some simplifications, but they will be difficult to make unless we know information about the modes involved. For example, are the modes different transverse modes? Then spatial dependence becomes important. How many modes do we care about? We could include all the modes of our cavity, but doing so would be inefficient if only two or three modes are significantly coupled to. So, the simplifications that can be made to the Hamiltonian above are rather dependent on experimental conditions. I leave it to you to decide what experimental conditions you have. If you find yourself struggling to find the relevant coupled basis states, remember that utilizing the uncoupled $|atom\rangle \otimes |cavity\rangle$ basis states is always an option. For N three-level atoms in a multimode cavity, these uncoupled basis states look like $|gggg...0000...\rangle$, $|gggg...1000...\rangle$, $|eggg...0000...\rangle$, $|gggg...0100...\rangle$, and so on for seemingly eternity if dealing with many modes and many atoms.

3.3 Examples of theory in practice

The section will overview a few examples of theory in practice. In practice, we typically use the tools of Mathematica, Python, or MATLAB to carry out our calculations using the formalism of non-Hermitian perturbation theory (NHPT), master equations, or Floquet theory. An overview of non-Hermitian perturbation theory has been well detailed across the theses of Simon Lab members such as References [38, 33, 39, 40, 41], so we will not repeat the derivation here.

My general rule of thumb has been to use non-Hermitian perturbation theory for time-independent Hamiltonians. For time-dependent Hamiltonians, I turn to master equation formalism or Floquet theory, if applicable. In our experiment, our primary means of data collection is counting photons over time. Thus, one might want to predict measurements such as cavity spectra or temporal correlations between photons using a model Hamiltonian to see if the experimental data are consistent with our theoretical understanding.

This section will not overview an exhaustive list of examples, but hopefully it will elucidate the connection between theoretically derived Hamiltonians and how they may be put to use.

3.3.1 NHPT for the VRS Hamiltonian in Mathematica

We've worked hard to simplify the Hamiltonian for N two-level atoms in a single mode cavity, and now we are going to use the simplified, time-independent Hamiltonian of Equation 3.30. Figure 3.1 depicts NHPT in code form where the laser drive is taken as a perturbation. The result is the cavity spectra (normalized to bare cavity transmission) as a function of the laser drive frequency ω_l, where numerical values have been assigned to variables to carry out computation. Additional results are the eigenvalues and eigenvectors of this Hamiltonian, and the fit form of the cavity spectra.

This spectral feature is often referred to as vacuum Rabi splitting (VRS), and the cor-

responding Hamiltonian as the N atom version of the Jaynes-Cummings Hamiltonian [42]. Intuitively, one might think of the atomic cloud as a piece of glass that changes the resonance condition of the cavity because it imparts a slight phase shift on intracavity light, causing this interesting spectral feature. Another way to think about this splitting is that the excited atomic state is coupled to the cavity state of one photon, and as coupled modes spectrally *split* in general, the result is a splitting in the spectra.

3.3.2 NHPT for the EIT Hamiltonian in Mathematica

We've also worked hard to simplify the Hamiltonian for N three-level atoms in a single mode cavity, and now we are going to use the simplified, time-independent Hamiltonian of Equation 3.37. Figure 3.2 depicts NHPT in code form where the laser drive is taken as a perturbation once again, with similar results to Subsection 3.3.1.

This spectral feature is often referred to as electromagnetically induced transparency (EIT). Importantly, the eigenstates here are what we call Rydberg polaritons—quasiparticles that are atom-photon hybrids. There are two "bright" polaritons, which are comprised partially of all three states—cavity photon, excited state, and Rydberg state—and one "dark" polariton, which is "dark" to the excited state. The dark polariton is of particular interest as a result of its strongly-interacting Rydberg component. When we create dark polaritons experimentally, we simply park our drive laser at the frequency which corresponds with the middle peak of this spectra, which is energetically the dark polariton.

3.3.3 NHPT for spatially-dependent Hamiltonians in Python

When dealing with a spatially-dependent Hamiltonian, it can be difficult to find the relevant collective states of the system, and in fact may be more straightforward to construct the Hamiltonian in the uncoupled basis. Once this Hamiltonian has been constructed, the most non-trivial step in NHPT is inverting a potentially large matrix. This process can be a pain

In[1]:=
```
parms = {κ → 1.6, Γ → 6, G → 5, ωc → 0, ωe → 0};
H = ( ωc - i κ/2      G
      G      ωe - i Γ/2 );
Imat = IdentityMatrix[Length[H]];
ψc = {1, 0};
Aout = κ/2 ψc.Inverse[Imat δ - H].ψc;
EAout = Evaluate[Abs[Aout]^2 /. parms];
Plot[EAout, {δ, -15, 15}, PlotRange → {0, 1}] (*yields cavity spectra*)
```

Out[7]=

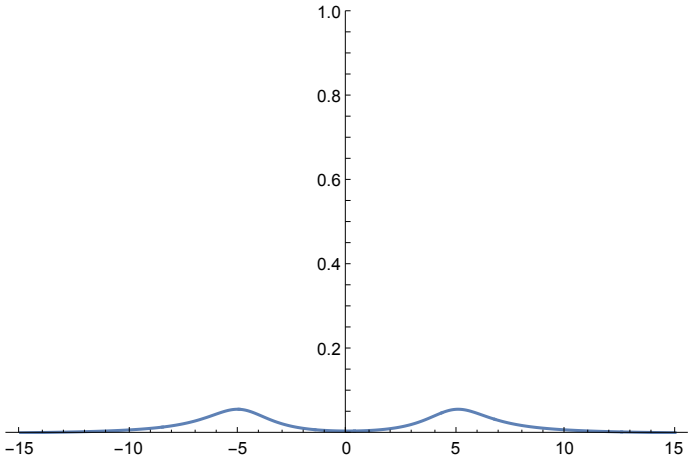

In[8]:=
```
Eigensystem[( ωc - i κ/2      G
              G      ωe - i Γ/2 ) /. {κ → 0, Γ → 0, ωc → 0, ωe → 0}]
(*Gives eigenvalues and eigenvectors!*)
```

Out[8]= {{-G, G}, {{-1, 1}, {1, 1}}}

In[9]:=
```
Abs[Aout]^2 (*fit form for VRS*)
```

Out[9]=
$$\frac{1}{4}\,\text{Abs}\left[\frac{\kappa\left(\frac{i\,\Gamma}{2}+\delta-\omega e\right)}{-G^2+\left(\delta+\frac{i\,\kappa}{2}-\omega c\right)\left(\frac{i\,\Gamma}{2}+\delta-\omega e\right)}\right]^2$$

Figure 3.1: **Theory in practice: VRS Hamiltonian.** The spectra above occurs when the cavity photon is resonant with the ground to excited transition in the atom, though one may explore off-resonant conditions by tweaking "params." In fact, if one sets $G = g\sqrt{N}$ to zero, the resulting spectra is just bare cavity transmission, as expected without any coupling to the atoms.

for many atoms, but fortunately can be sped up using sparse matrix methods as many entries in the Hamiltonian will end up being zero.

Let's consider a few two-level atoms that experience a spatially-dependent g due to their distribution across a spatially-varying cavity mode. The Hamiltonian for this system can be constructed by brute force using for loops in Python—no special packages necessary—as depicted in Figure 3.3, where the value for g is modified by the location of each atom and mode parameters. After this Hamiltonian is constructed, we can carry out NHPT and view the resulting spectra.

Each run of the code randomizes the locations of the atoms within some Gaussian distribution—not unlike a real experiment. Figure 3.4 depicts how the cavity spectra depends on the locations of the atoms. Put simply, an atom needs to overlap with the mode in order for g to be nonzero for that atom! This reason is why atomic distributions that overlap with the mode more have a greater overall splitting in the spectra.

3.3.4 Master equations for time-dependent Hamiltonians in Python

In this subsection, we will essentially put back the time dependence we simplified away for our VRS Hamiltonian to demonstrate how one might handle time-dependent Hamiltonians. It turns out this time dependence can be handled quite nicely using the built-in master equation formalism in the QuTiP software for Python. Now, our laser drive term is no longer treated as a perturbation as in NHPT and is included in the full Hamiltonian.

The left plot in Figure 3.5 depicts the expectation value of the cavity photon number over time, which Rabi oscillates. Intuitively, this oscillation can be thought of as an exchange of the photon between the atoms and the cavity. If we average over this oscillation in time for various drive frequencies, we regain our familiar VRS splitting as depicted in the right plot Figure 3.5. These time and frequency domain plots were generated by the code shown in Figures 3.6 and 3.7, respectively.

In[1]:=
```
parms = {κ → 1.6, Γ → 6, G → 5, ωc → 0, ωe → 0, Δ → 0, γr → 1, Ω → 3};

H = ( ωc - i κ/2      G              0
      G               ωe - i Γ/2     Ω
      0               Ω              Δ - i γr/2 );

Imat = IdentityMatrix[Length[H]];
ψc = {1, 0, 0};
Aout = κ/2 ψc.Inverse[Imat δ - H].ψc;
EAout = Evaluate[Abs[Aout]^2 /. parms];
Plot[EAout, {δ, -15, 15}, PlotRange → {0, 1}] (*yields cavity spectra*)
```

Out[7]=

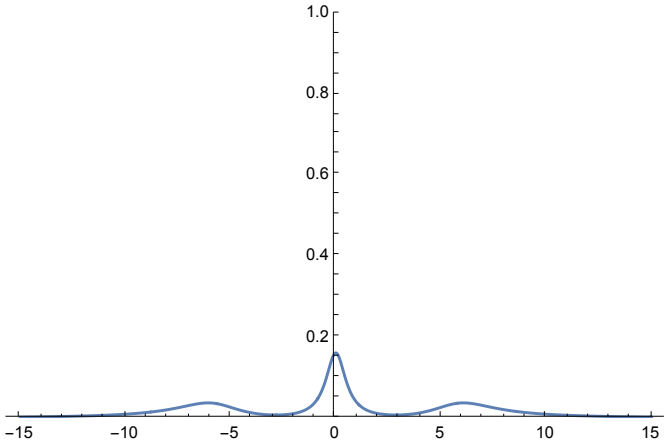

In[8]:=
```
Eigensystem[ ( ωc - i κ/2      g              0
               g               ωe - i Γ/2     Ω
               0               Ω              Δ - i γr/2 ) /. {κ → 0, Γ → 0, ωc → 0, ωe → 0, Δ → 0, γr → 0}]

(*Gives eigenvalues and eigenvectors! You can see how the
 peak with eigenvalue 0 has a 0 component for the excited state!*)
```

Out[8]=
$$\left\{\left\{0, -\sqrt{g^2+\Omega^2}, \sqrt{g^2+\Omega^2}\right\}, \left\{\left\{-\frac{\Omega}{g}, 0, 1\right\}, \left\{\frac{g}{\Omega}, -\frac{\sqrt{g^2+\Omega^2}}{\Omega}, 1\right\}, \left\{\frac{g}{\Omega}, \frac{\sqrt{g^2+\Omega^2}}{\Omega}, 1\right\}\right\}\right\}$$

In[9]:=
```
Abs[Aout]^2 (*fit form for EIT*)
```

Out[9]=
$$\frac{1}{4}\,\text{Abs}\left[\frac{\kappa\left(-\Omega^2+\left(\frac{i\gamma r}{2}+\delta-\Delta\right)\left(\frac{i\Gamma}{2}+\delta-\omega e\right)\right)}{\Omega\left(-\delta\,\Omega-\frac{i\kappa\Omega}{2}+\Omega\,\omega c\right)+\left(\frac{i\gamma r}{2}+\delta-\Delta\right)\left(-G^2+\left(\delta+\frac{i\kappa}{2}-\omega c\right)\left(\frac{i\Gamma}{2}+\delta-\omega e\right)\right)}\right]^2$$

Figure 3.2: **Theory in practice: EIT Hamiltonian.** The spectra above occurs when the cavity photon is resonant with the ground to excited transition in the atom, and similarly a control drive is resonant with the excited to Rydberg transition.

```
# generates the single-excitation Hamiltonian for "n_cav" cavity modes and "n_atoms" atoms
# dimension of matrix will be (n_cav+2*n_atoms) x (n_cav+2*n_atoms) for cavity modes and atoms with 2 levels
def gen_M(cav_arr, atom_arr, state_arr):
    [n_atoms, atoms_x, atoms_y]=gen_atoms(atom_arr);
    n_cav=len(cav_arr);
    M = zeros(n_cav+2*n_atoms,n_cav+2*n_atoms)
    for i in range(n_cav+2*n_atoms):
        for j in range(n_cav+2*n_atoms):
            if i<n_cav:
                M[i,i]=cav_arr[i][0]-1.0j*(cav_arr[i][1]/2)
            if i>=n_cav and i<n_cav+n_atoms:
                M[i,i]=0-1.0j*(atom_arr[3]/2)
            if i<n_cav and j>=n_cav and j<n_cav+n_atoms:
                p = cav_arr[i][2]
                l = cav_arr[i][3]
                ω0 = cav_arr[i][4]
                g = cav_arr[i][5]
                M[i,j]=g*LGCart(atoms_x[j-n_cav], atoms_y[j-n_cav], p, l, ω0);
            if j<n_cav and i>=n_cav and i<n_cav+n_atoms:
                p = cav_arr[j][2]
                l = cav_arr[j][3]
                ω0 = cav_arr[j][4]
                g = cav_arr[j][5]
                M[i,j]=np.conjugate(g*LGCart(atoms_x[i-n_cav], atoms_y[i-n_cav], p, l, ω0));
            if i>=n_cav+n_atoms:
                M[i,i]=state_arr[0]-1.0j*(state_arr[1]/2)
            if i<n_cav+n_atoms and i>=n_cav and j>=n_cav+n_atoms and j==(i+n_atoms):
                p = state_arr[2]
                l = state_arr[3]
                ω0 = state_arr[4]
                Ω = state_arr[5]
                M[i,j]=Ω*LGCart(atoms_x[i-n_cav], atoms_y[i-n_cav], p, l, ω0);
            if j<n_cav+n_atoms and j>=n_cav and i>=n_cav+n_atoms and i==(j+n_atoms):
                p = state_arr[2]
                l = state_arr[3]
                ω0 = state_arr[4]
                Ω = state_arr[5]
                M[i,j]=np.conjugate(Ω)*(LGCart(atoms_x[j-n_cav], atoms_y[j-n_cav], p, l, ω0));
    return M, atoms_x, atoms_y
```

Figure 3.3: **Theory in practice: spatially-dependent Hamiltonian.** The uncoupled basis Hamiltonian is constructed by brute force using for loops over all atoms and cavity modes.

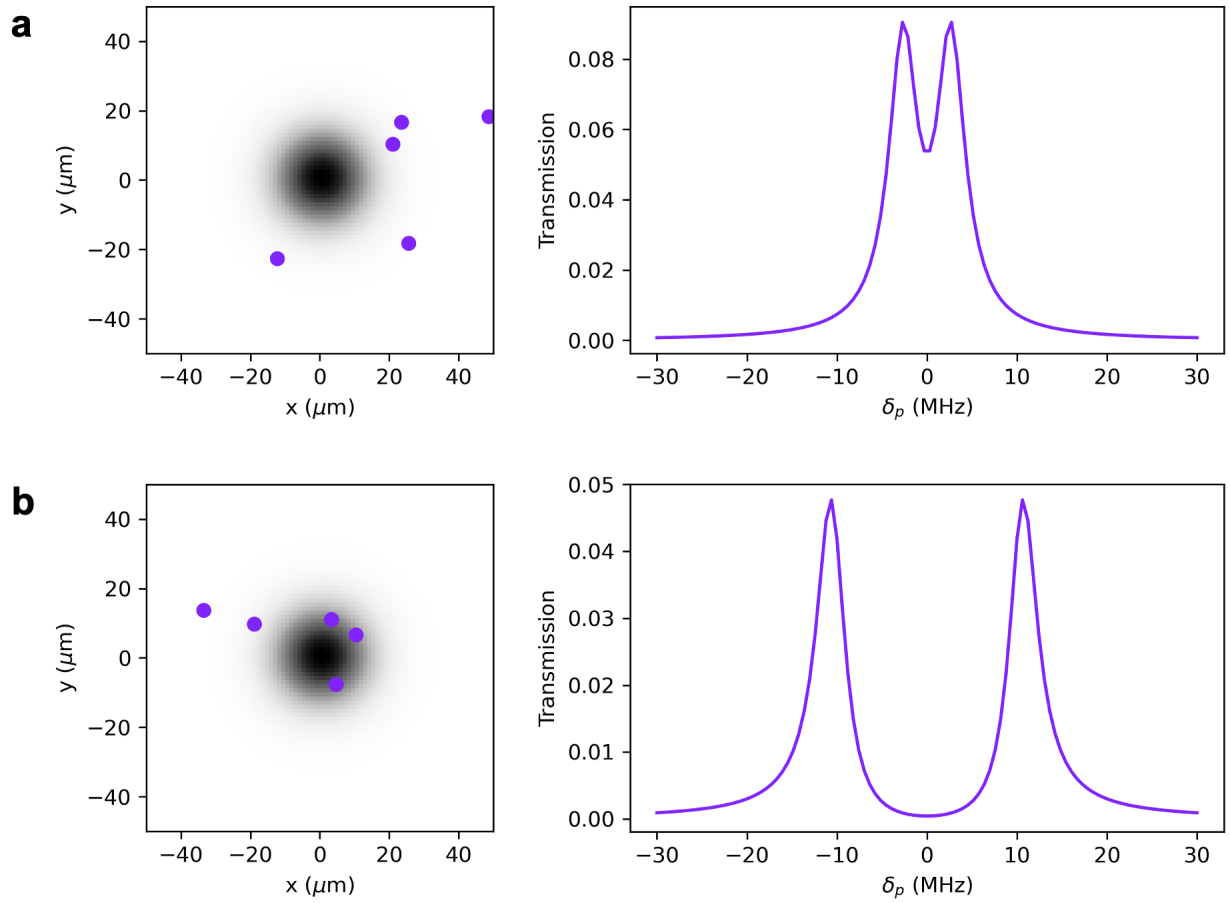

Figure 3.4: **Effect of spatial dependence on spectra.** The atoms in **b** overlap with the cavity mode significantly more than the atoms in **a**, resulting in a wider VRS in the spectra.

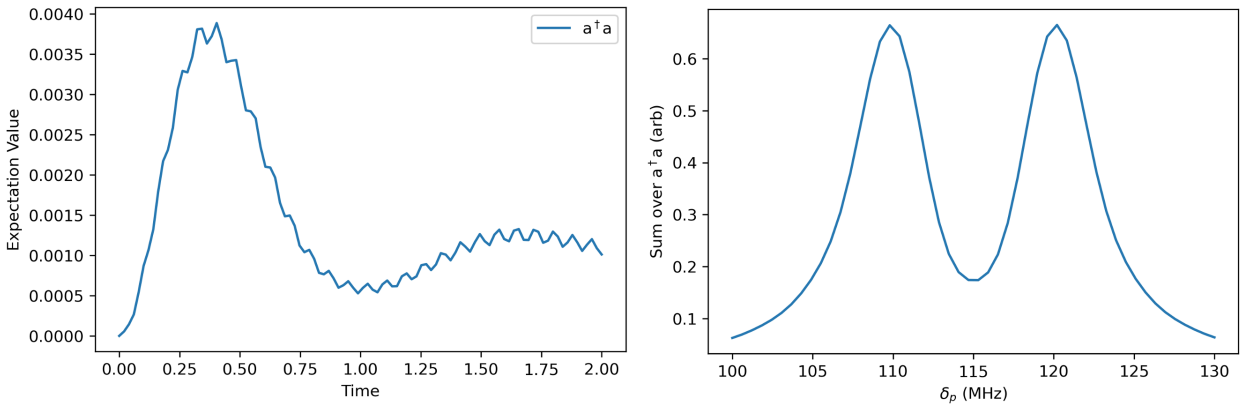

Figure 3.5: **Theory in practice: time-dependent Hamiltonian.** Rabi oscillations can be seen in the time domain (left), which equate to a VRS in the frequency domain (right).

Essentially "un-doing" the rotating-frame transformation, we have:

$$H_0 = (\omega_{cav} - \frac{i\kappa}{2})a^\dagger a + (\omega_{atom} - \frac{i\Gamma}{2})b^\dagger b + g(a^\dagger b + bp^\dagger)$$

$$H_1 = \Omega_p sin(\omega_p t)(a^\dagger c + ac^\dagger)$$

or in matrix form:

$$H_0 = \begin{pmatrix} 0 & 0 & 0 \\ 0 & \omega_{cav} - \frac{i\kappa}{2} & g \\ 0 & g & \omega_{atom} - \frac{i\Gamma}{2} \end{pmatrix} H_1 = \begin{pmatrix} 0 & \Omega_p sin(\omega_p t) & 0 \\ \Omega_p sin(\omega_p t) & 0 & 0 \\ 0 & 0 & 0 \end{pmatrix}$$

where the full Hamiltonian is $H_0 + H_1$, qutip just wants time-dependent things to be split up from non-time-dependent things like this.

```
# Time-dependence: https://qutip.org/docs/latest/guide/dynamics/dynamics-time.html
def H1_coeff(t, args):
    omega_p = args['omega_p']; omega = args['omega'];
    return omega_p * np.sin(omega*t)
```

```
w_cav=115; w_atom=115; g=5.0; kappa=1.3; gamma=6; omega_p=0.6; omega=115; N=2;
c = tensor(destroy(N), qeye(N), qeye(N)) # tensor used here to make c, a, and b act on different subspaces!
a = tensor(qeye(N), destroy(N), qeye(N))
b = tensor(qeye(N), qeye(N), destroy(N))
psi0  = tensor(basis(N,1), basis(N,0), basis(N,0))
c_ops = [np.sqrt(0.0)*c, np.sqrt(kappa) * a, np.sqrt(gamma) * b]
H0 = (w_cav) * a.dag()*a + (w_atom) * b.dag()*b + g*(a.dag()*b+b.dag()*a) + 0*c.dag()*c
H1 = (c.dag()*a+a.dag()*c)

args={'omega_p': omega_p, 'omega': omega}
H = [H0,[H1, H1_coeff]]

times = np.linspace(0.0, 2.0, 100)
result = mesolve(H, psi0, times, c_ops, [c.dag()*c, a.dag()*a, b.dag()*b], args=args)
fig, ax = plt.subplots()

ax.plot(times, result.expect[1]);
ax.set_xlabel('Time');
ax.set_ylabel('Expectation Value');
ax.legend(['a$^\dagger$a']);
plt.show()
```

Time

Figure 3.6: **Generating time domain plots with QuTiP.**

```
omega_arr=np.linspace(100,130,50)
times = np.linspace(0.0, 2.0, 200)
w_cav=115; w_atom=115; g=5.0; kappa=1.3; gamma=6; omega_p=0.6;
c = tensor(destroy(N), qeye(N), qeye(N))
a = tensor(qeye(N), destroy(N), qeye(N))
b = tensor(qeye(N), qeye(N), destroy(N))
psi0  = tensor(basis(N,1), basis(N,0), basis(N,0))
exp_arr = np.zeros(len(delta_arr))
c_ops = [np.sqrt(0.0)*c, np.sqrt(kappa) * a, np.sqrt(gamma) * b]

for idx, omega in enumerate(omega_arr):

    # The timescale depends on the units of the Hamiltonian. If your coefficients are written as 2pi*f then your timescale is 1/f.
    H0 = (w_cav) * a.dag()*a + (w_atom) * b.dag()*b + g*(a.dag()*b+b.dag()*a) + 0*c.dag()*c
    H1 = (c.dag()*a+a.dag()*c)
    args={'omega_p': omega_p, 'omega': omega}
    H = [H0,[H1, H1_coeff]]
    result = mesolve(H, psi0, times, c_ops, [c.dag()*c, a.dag()*a, b.dag()*b],args=args)
    exp_arr[idx]=np.sum(result.expect[1])

fig, ax = plt.subplots()
ax.plot(omega_arr, ((kappa/2)/omega_p)**2*(1/times[-1])*exp_arr);
ax.set_xlabel('$\delta_p$ (MHz)');
ax.set_ylabel('Sum over a$^\dagger$a (arb)');
plt.show(fig)
```

Frequency

Figure 3.7: **Generating frequency domain plots with QuTiP.**

CHAPTER 4

EXPERIMENTAL SETUP

4.1 Overview

This chapter is primarily intended to provide an overview of the physical equipment in the experiment and how it operates. In an effort to be as blunt as possible, the first two subsections of this chapter will pose the following explicit questions to be answered:

(1) What is the thing?

(2) Why do we have it?

As the work presented in this thesis is centered around the platform of atoms in cavities, almost all aspects of the experimental setup boil down to manipulating light, atoms, and cavities.

4.2 Inside vacuum

4.2.1 The twisted cavity structure

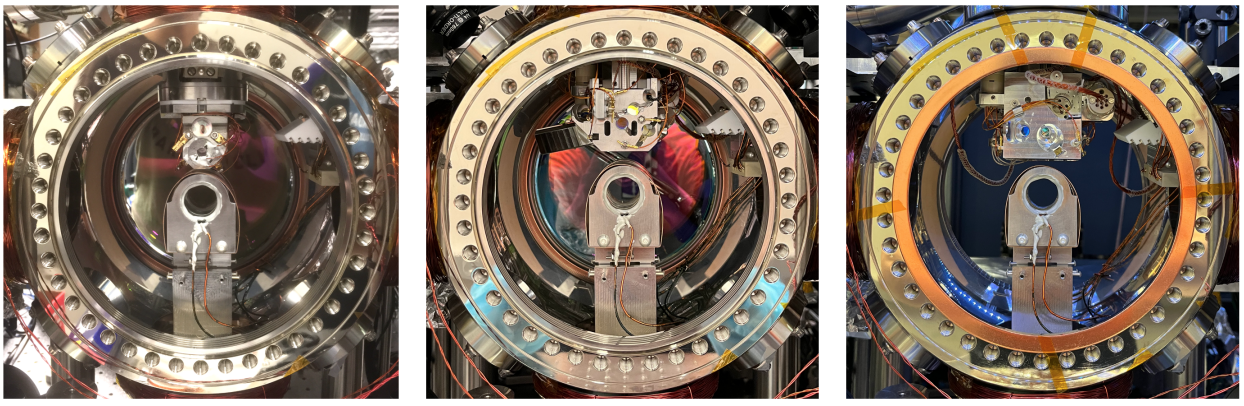

Figure 4.1: **Cavity generations.** From left to right: the first *planar* in-vacuum experimental cavity, the Original Twister, and Lluna.

What is the thing? The twisted cavity structure is a machined block of metal that houses the cavity within which we create quantum materials made of light and other components for cavity and atom control. There have been several twisted cavity structure generations (Figure 4.1), but I will discuss only the two most recent generations and their general features below:

Original Twister (2018-2022)

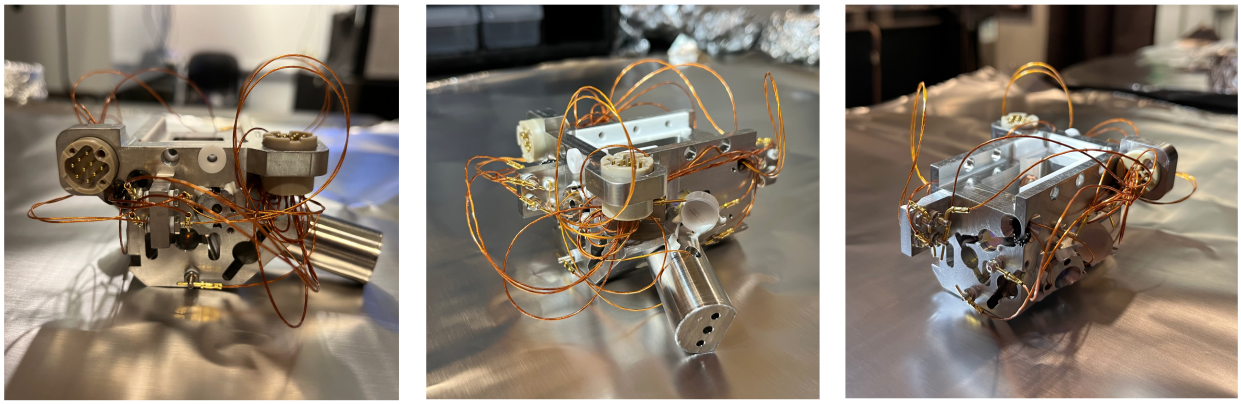

Figure 4.2: **The Original Twister.**

The Original Twister cavity structure was used in the works of both Chapters 5 and 6 and was machined from 316 stainless steel by Zero Hour Parts.

This structure housed two twisted cavities whose modes crossed at 35 degrees: one primarily for 780 nm light, and one primarily for 480 nm light. The 780 nm cavity was comprised of four curved mirrors procured from LAYERTEC GmbH, two convex mirrors (99.91(1)% reflection) and two concave mirrors (HR), to achieve a small waist at the location of the atoms and effectively reduced the number of input-output ports from four to two. The 780 nm cavity mirrors were additionally coated at 1560 nm so that 1560 nm light could be used for a Pound-Drever-Hall lock to stabilize the cavity length. Both cavities contained one mirror glued to a short ring piezo (Noliac NAC2123) to actuate the cavity length stabilization. The 780 nm cavity contained an additional mirror mounted to a long throw piezo for the purpose of significantly tuning the overall cavity length. To avoid degradation of the mirror

coatings in vacuum, the outer layer of all mirror coatings' dielectric stacks were specified for SiO_2, not Ta_2O_5 [43].

Electrodes were mounted in the structure to control the electric field at the location of the atoms (Figure 4.3). Here, "control" really means "zero" most of the time as we usually deal with Rydberg atoms which are highly sensitive to electric fields. The electrodes are screws that have had a hole drilled through the end for a voltage-delivering pin to be held by friction. The screws are physically, and thus electrically, isolated from the cavity structure by Macor washers. The washers facing the atoms are covered with very thin, handmade copper washers to shield the atoms from potential fields generated by induced dipoles in the dielectric Macor. To prevent our atoms from interacting with surface-generated fields in general, we make an effort to physically space the atoms > 10 mm from any point in the twisted cavity structures when possible. As electric field control entails three electric field components and five independent electric field gradients, at least eight electrodes are needed to account for eight degrees of freedom. The Original Twister cavity structure contained eight electrodes plus voltage control of the structure itself, enabled by its electrical isolation from the other components in the vacuum chamber. To relate electrode voltages to electric fields and gradients at the location of the atoms, transformation matrices were calculated using finite element analysis.

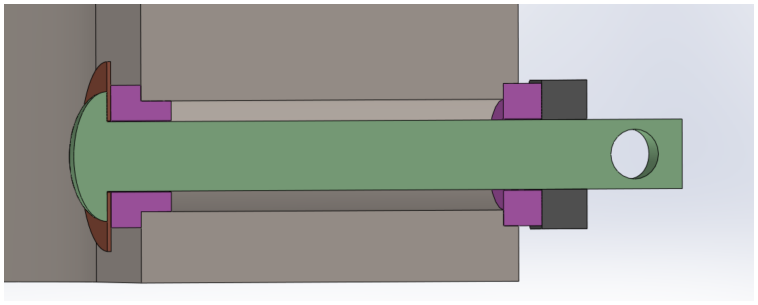

Figure 4.3: **Pin electrode.** A screw (green) passes through the cavity structure wall (beige). It is electrically isolated from the cavity structure by two Macor inserts (pink), with a copper washer (brown) shielding the inner insert from line of sight to the atoms. The screw is secured with a nut (grey), and a voltage-delivering pin can slip into the hole drilled in the end of the screw.

A wire was threaded in a conduit around the structure for the purpose of heating, thereby offering another option for changing the cavity length appreciably in addition to the long throw piezo. All electrical connections for the Original Twister were made via Subminiature-C connectors and Kapton-insulated wire (custom, from Accu-Glass Products, Inc.). Wires from the heating wire, electrodes, and piezos terminated in these connectors that were glued on to the structure itself, which were in turn connected to cables (Accu-Glass 100120) leading to the vacuum chamber feedthroughs (Accu-Glass 100012). The big advantage to this connection design was its modular nature; clunky feedthrough cables need only be installed once by feeding them through the tight spaces within the custom flange atop the main vacuum chamber, then the cavity structure could be installed and removed at will by plugging in and unplugging the feedthrough cables into the Subminiature-C connectors on the structure. Torr-Seal was used for all components (mirrors, piezos, Subminiature-C connectors) that needed to be glued somewhere on cavity structure.

The Original Twister cavity structure enabled a lot of neat science, but also had its problems. One minor issue that occurred during operation with this cavity structure was electric field drifts due to slow changes in the 780 nm cavity locking piezo voltage that affected experimental performance when using Rydberg atoms. This problem was largely resolved by using an Arduino-based feedback loop to keep the piezo voltage roughly constant at 60 V by changing the cavity length with a pulse-width modulated 980 nm heating laser ($\sim$1 W) outside vacuum. This laser was cheaply acquired through Amazon. The laser was focused to about a 1 mm spot on the long throw piezo housing, which juts out of the cavity structure. Another issue that occurred was the degradation of the 480 nm cavity finesse over time, likely due to the interaction of the high intracavity 480 nm power with a cavity mirror that was last-minute acquired from eBay to replace the mirror that was originally going to be used but wasn't as it was loss-dominated. Yet another problem was the misalignment of the 480 nm cavity from the 780 nm cavity as a result of the vacuum bake-out after installation of

the Original Twister structure. This issue was somewhat resolved by utilizing a higher order transverse mode of the 480 nm cavity that was spatially large enough to intersect with the 780 nm cavity mode. While this solution was sufficient to continue with the experiment, the misalignment of the 480 nm cavity ultimately meant much less 480 nm power incident on the atoms than we had hoped. The largest problem that occurred was astigmatism in the 780 nm cavity that caused photonic modes to mix at the cavity length where we expected these modes to by degenerate. Chapter 5 will go into this problem, workarounds, and solutions in more depth. The next generation cavity, Lluna, was designed with the primary intention of achieving mode degeneracy by minimizing optical aberrations.

Lluna (2022-present)[1]

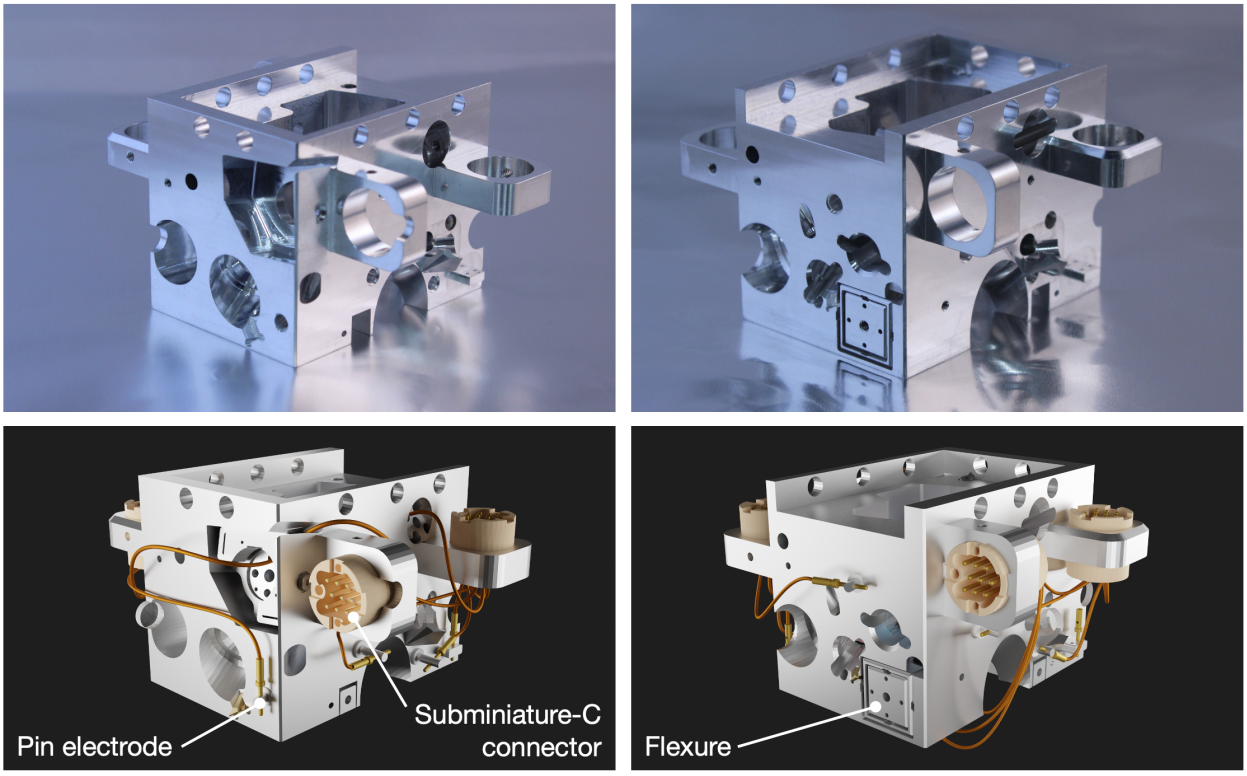

Figure 4.4: **Lluna.**

1. Why the name "Lluna?" As quoted by Matt Jaffe on the Simon Lab Slack, because (1) the cavity structure was "a bit of a moonshot" and (2) the two Ls are for (i) "Landau Level," (ii) "Lens-Lens," and (iii) "to evoke the majestic llama."

Lluna is the successor to the Original Twister. This cavity structure was machined from aluminum by 3ERP. All previous structures were machined from 316 stainless steel as this material has been tried and true (and also the most nonmagnetic stainless steel). However, Lluna was more challenging to machine due to fine structural features and hence necessitated a softer material. So far, it appears there have been no adverse affects due to the usage of aluminum.

This structure also houses two twisted cavities, again primarily for 780 nm and 480 nm light, whose modes cross at 32.5 degrees. The 780 nm cavity is comprised of four flat mirrors (from FiveNine Optics) and two aspheric lenses (from Optimax). The 480 nm cavity is comprised of a mixture of curved and flat mirrors (from FiveNine Optics). See Figure 4.5 for more details. Both cavities contain one mirror glued to a short ring piezo (NAC2122 from CTS, formerly Noliac) with Master Bond EP42HT-3AO glue. Both piezos were pre-baked and cleaned by CTS and were affixed with A02 UHV-compatible wires, 28 AWG.

The electrodes are, once again, screws that hold voltage-delivering pins. Holes were drilled in the ends of #2-56 screws that were electrically isolated from the cavity structure by Macor washers machined by 3ERP. Copper washers were handmade using 0.005" thick copper shim stock (Trinity Brand Industries 6CPR50-5) to cover the Macor. Holes were drilled in the shim stock, then washers were punched out manually using a punch (Trinity Brand Industries SP-9) of the appropriate the outer diameter to completely shield the atoms from line of sight to any Macor. This cavity structure one again utilized Subminiature-C connectors for ease of installation.

Lluna was designed with the intention of solving many of the problems that existed in the Original Twister. To address the potential misalignment of the 480 nm cavity due to the bake, we mounted ring piezo-backed mirror in a tip-tilt piezo stage (SmarAct STT-12.7-UHVT-NM) to finely adjust the 480 nm cavity alignment in vacuum if necessary. While not a problem in the Original Twister per say, Lluna now enables side optical access to

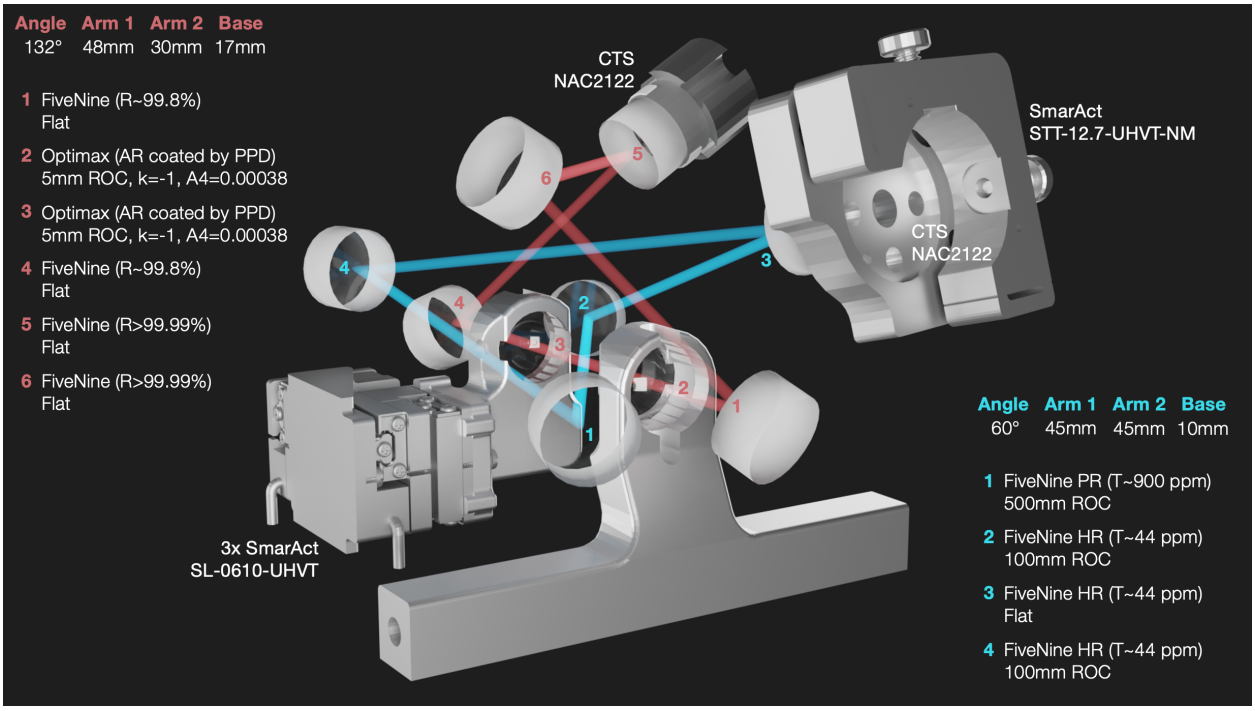

Figure 4.5: **Lluna cavities.** This graphic contains the most relevant components and their specs for the 780 nm and 480 nm twisted cavities of Lluna. For those interested in the 3D coordinates of all four mirrors m_1, m_2, m_3, and m_4, they are $m_1 = \{0, -0.5 \times \text{arm}_1, 0\}$, $m_2 = \{\text{base}, 0.5 \times \text{arm}_2 \times \cos(\text{angle}), 0.5 \times \text{arm}_2 \times \sin(\text{angle})\}$, $m_3 = \{\text{base}, -0.5 \times \text{arm}_2 \times \cos(\text{angle}), -0.5 \times \text{arm}_2 \times \sin(\text{angle})\}$, and $m_4 = \{0, 0.5 \times \text{arm}_1, 0\}$.

the atoms for potential imaging or light excitation. Perhaps most importantly, Lluna was designed to address the problem of non-degenerate modes by minimizing optical aberrations that prevented degeneracy. See Chapter 5 for additional details. The upshot is that instead of utilizing four *curved* mirrors in which the cavity mode strikes curved surfaces at non-normal incidence as in the Original Twister, Lluna utilizes four *flat* mirrors and two *curved* intracavity aspheric lenses to provide beam focusing. In this optical arrangement, the cavity mode strikes curved surfaces at normal incidence, minimizing optical aberrations. One of the intracavity lenses is mounted in a custom lens holder that is affixed to a 3-axis piezo stage (3x SmarAct SL-0610-UHVT) for fine positioning in vacuum if necessary. This 3-axis stage is further mounted on to a flexure machined into the side of the cavity structure for initial alignment purposes outside vacuum.

	Original Twister	**Lluna**
Material	316 Stainless steel	Aluminum
780 nm cavity		
Optics	4x curved mirrors	4x flat mirrors, 2x lenses
FSR	2500 MHz (adjustable)	2270 MHz (adjustable)
Linewidth κ	1.4 MHz	2.9 MHz
Finesse $\mathcal{F}$	1900	1200 (experimental)
Waist at atoms	19 μm	18 μm
480 nm cavity		
Optics	6x curved mirrors	4x curved, flat mirrors
FSR	1135 MHz	1760 MHz
Linewidth κ	6 MHz	720 kHz
Finesse $\mathcal{F}$	190	3000 (experimental)
Waist at atoms	98 μm	106 μm
Additional features	Pin electrodes x8+1	Pin electrodes x8+1
	Piezo-backed mirrors x3	Piezo-backed mirrors x2
	Heating wire	Piezo stages x4

Table 4.1: **Cavity comparison.** The table above lists specs of the Original Twister versus Lluna. See the Supplement of [44] for additional details about the Original Twister.

Why do we have it? Most importantly, the twisted cavity structure exists to create a degenerate manifold of 780 nm photonic modes to enable to study of fractional quantum hall physics. We position a cloud of ^{87}Rb atoms at the intersection between the 780 nm and 480 nm cavity modes, which excite the atomic transitions $5S_{1/2} \leftrightarrow 5P_{3/2}$ and $5P_{3/2} \leftrightarrow$Rydberg, respectively. As mentioned in the footnote of Subsection 3.2.3, it is important that the waist of the $5P_{3/2} \leftrightarrow$Rydberg excitation beam is large, hence the large 480 nm waists relative to the 780 nm waists in Table 4.1. In the scope of its remaining functions, the twisted cavity structure holds necessary components for atom control (electrodes) and cavity control (piezo stages, ring piezos, and heating elements).

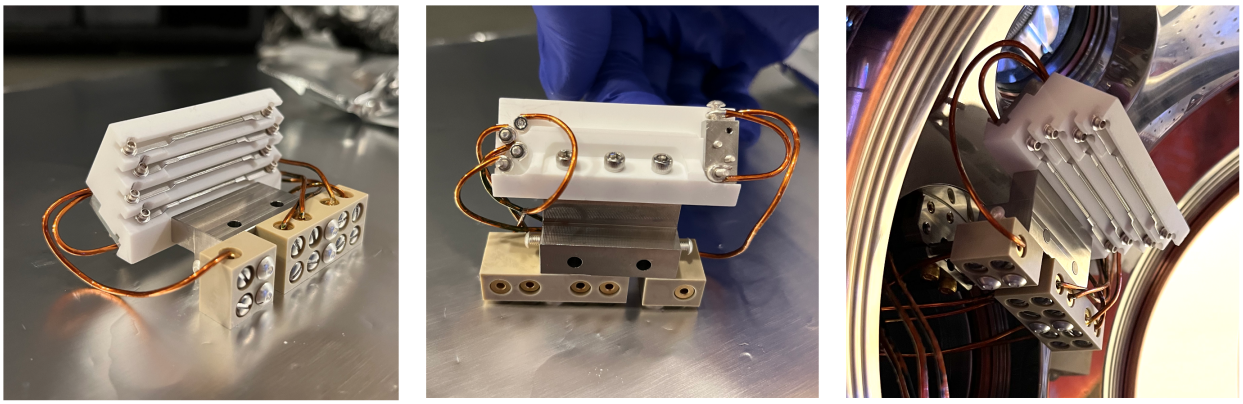

Figure 4.6: **Rubidium dispensers.** The rubidium dispensers, or getters, are the silver rod-like objects mounted in the white Macor structure.

4.2.2 Rubidium dispensers

What is the thing? Our rubidium dispensers, or getters, are procured from SAES. After activating them during the vacuum bake-out, we typically run a current of around 3-3.5 A through them to evaporate rubidium into the main vacuum chamber, which additionally contains the MOT coils and twisted cavity structure. Be careful not to run these dispensers at too high of current as doing so can deplete the rubidium quickly!

The rubidium dispensers are mounted in a Macor block (Figure 4.6), which in turn is mounted to two rods protruding from a groove grabber affixed on the vacuum chamber grooves. Electrical connections between the wires of the Macor structure and the wires leading to a vacuum chamber feedthrough are made within a PEEK terminal block, which contains screws that clamp down on wires to make an electrical connection.

The rubidium dispensers used to be mounted to the Macor structure via screws that clamped down on the dispenser edges, additionally providing an electrical connection. Dispensers could initially be ran normally, but would fail to turn on again after the current had been turned down to zero. However, dispensers we ran continuously would continue to dispense. Thus, for the lifetime of the Original Twister, we ran current through dispensers continuously, raising the current during daily operation to 3-3.5 A and dropping the current

down to 2 A overnight. Upon inspection of the dispensers during Lluna's installation, we discovered that the dispensers that failed to turn on again had physically disconnected from their clamping screws, likely due to the thermal cycle associated with turning off the dispensers completely after being heated by non-zero current. Now, we spot weld washers to the dispenser edges and insert the clamping screw into the washer hole, significantly increasing the surface area of electrical contact.

Why do we have it? The rubidium dispensers provide our ^{87}Rb for the experiment!

4.2.3 Magneto-optical trap (MOT) coils

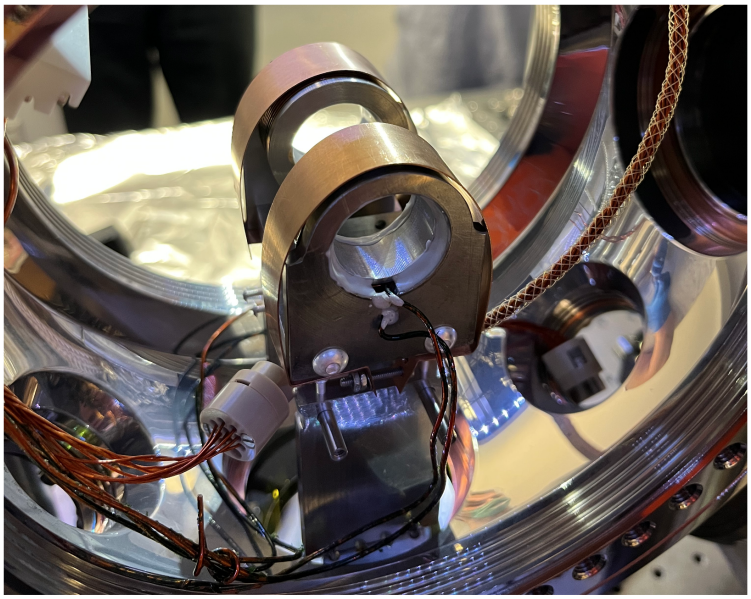

Figure 4.7: **MOT coils.** The coils themselves are shielded from line of sight to the atomic cloud by strips of copper as the coils are coated in Kapton, which is a dielectric.

What is the thing? The magneto-optical trap (MOT) coils are two, 36-turn Kapton-insulated wire coils in an anti-Helmholtz configuration. The dielectric Kapton is shielded from line of sight to the atomic cloud by a strip of copper around the top of the coil structure 4.7.

Why do we have it? The MOT coils provide the magnetic field gradient necessary to produce a MOT, which traps a cloud of ^{87}Rb atoms at the center of the chamber.

4.3 Outside vacuum

4.3.1 Lasers

Name	Make	Model	Laser Medium	Class	Wavelength (nm)	Max Output	Optical Density (OD)	MPE (mW/cm²)	Diffuse NHZ (m)
Master Laser	Eagleyard Photonics	EYP-DFB-0780	Diode	3B	780	100 mW	2.25	1.45	4.69E-02
MOT Laser	Photodigm	PH780DBR180T8	DBR	3B	780	180 mW	2.51	1.45	6.30E-02
MOT TA	Thorlabs	TPA780P20	Tapered Amplifier	4	780	2 W	3.556	1.45	0.21
Repumper Laser	Eagleyard Photonics	EYP-DFB-0780	Diode	3B	780	100 mW	2.25	1.45	4.69E-02
D1 Laser	Photodigm	PH795DBR120T8	DBR	3B	795	150 mW	2.401	1.55	0.06
1560 Seed	Orbits Lightwave, Inc.	Ethernal	Fiber Laser	3B	1560	50 mW	0.716	100	0.00E+00
NuFern Laser	NuFern	NuAmp	Amplifier	4	1560	10 W	3.02	100	5.64E-02
480 Laser	Toptica	TA-SHG Pro	Diode	4	480, 960	400 mW, 2.5 W	2.6, 3.29	2.55, 3.31	7.07E-2, 1.55E-1
Lattice Seed	Toptica	780 DL Pro	Diode	3B	783	100mW	2.249	1.47	0.05
Lattice TA	Sacher Lasertechnik	TEC 400-0780-1500	Amplifier	4	780	1.5 W	3.43	1.45	1.82E-01
Brady	Gooch & Housego	AA1406-196000-100-PM900-FCA-NA	DFB Diode	3B	1529	100 mW	1.017	100	0.00E+00
Gronk	Amonics	AEDFA-PM-37-R-NC	EDFA	4	1529	6W	2.795	100	4.37E-02
1011 Laser	Coherent Dilas	TAL-1010-2000	Tapered Laser	4	1011	2 W	3.094	4.19	0.12

Figure 4.8: **Lasers.**

What is the thing? We own many lasers for a variety of purposes. See Figure 4.8 for information about our main lasers.

Why do we have it? See below for a list of our main lasers and their purposes. Remember, $5S_{1/2}$ $(F = 2) \leftrightarrow 5P_{1/2}$ transitions are referred to as the D1 line and occur around 795 nm, and $5S_{1/2} \leftrightarrow 5P_{3/2}$ transitions are referred to as the D2 line and occur around 780 nm.

- **Master Laser.** The Master Laser is utilized as a frequency reference for the MOT Laser and Repumper Laser. It is typically locked on the $F = 2 \rightarrow 2'$, $F = 2 \rightarrow 3'$

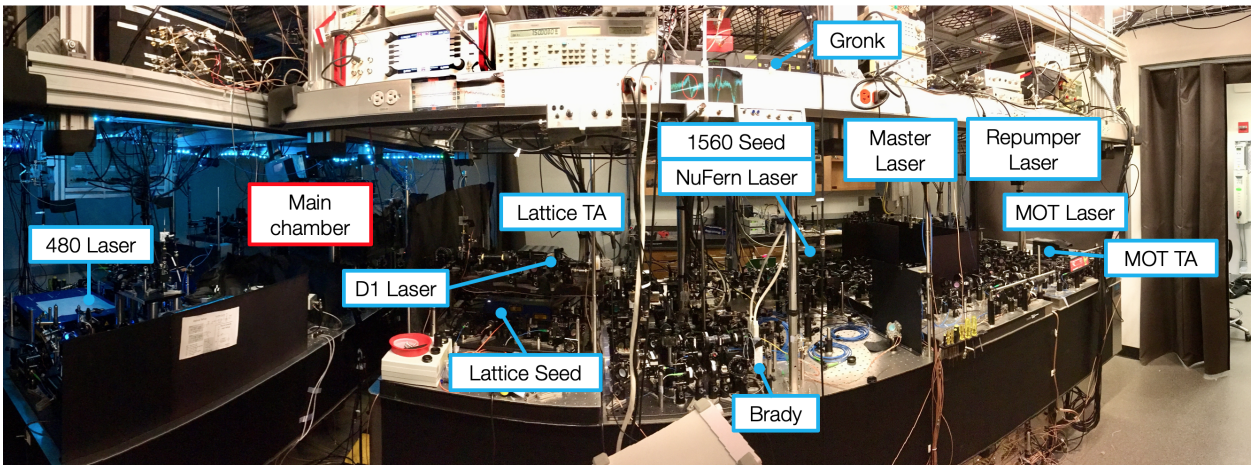

Figure 4.9: **Lasers in the lab.** The lasers listed in Figure 4.8 are physically indicated in the figure above (where visible).

crossover frequency of ^{87}Rb using a rubidium vapor cell, saturated absorption spectroscopy, and a lockbox.

- **MOT Laser.** The MOT Laser is used to create the MOT in the center of our main vacuum chamber, then utilized for polarization-gradient cooling (PGC). Its frequency is slightly red detuned from the $5S_{1/2}$ $(F = 2) \leftrightarrow 5P_{3/2}$ $(F' = 3)$ transition. This detuning can be controlled in the experimental sequence (Section **??**).

- **MOT TA.** The MOT tapered amplified (TA) is used to amplify the MOT Laser power to ∼1 W, yielding 150-200 mW of power in each MOT arm (horizontal and diagonal) near the main chamber.

- **Repumper Laser.** The Repumper Laser is used to "repump" the atoms that have off-resonantly scattered photons and fallen into to the $5S_{1/2}$ $(F = 1)$ state back up to the $5S_{1/2}$ $(F = 2)$ state so the MOT Laser can continue to cool them. Its frequency is resonant with the $5S_{1/2}$ $(F = 1) \leftrightarrow 5P_{3/2}$ $(F' = 2)$ transition.

- **D1 Laser.** The D1 Laser is used for optical pumping the atoms into the $5S_{1/2}$ $(F = 2)$ stretched state. It is typically locked on the $F = 2 \rightarrow 1'$, $F = 2 \rightarrow 2'$ crossover

frequency. This light is frequency modulated to contain frequency tones near the $5S_{1/2}$ $(F = 2) \leftrightarrow 5P_{1/2}$ $(F' = 2)$ and $5S_{1/2}$ $(F = 1) \leftrightarrow 5P_{1/2}$ $(F' = 2)$ transitions. The tone near $5S_{1/2}$ $(F = 2) \leftrightarrow 5P_{1/2}$ $(F' = 2)$ induces transitions toward the $5S_{1/2}$ $(F = 2)$ stretched state, and the tone near $5S_{1/2}$ $(F = 1) \leftrightarrow 5P_{1/2}$ $(F' = 2)$ repumps atoms that have accidentally fallen to the $5S_{1/2}$ $(F = 1)$ state back to the $5S_{1/2}$ $(F = 2)$ state. Finding the optimum power balance and frequencies of these tones has been finicky in the past, so do explore the power and frequency parameter space if you find optical pumping to be ineffective.

- **1560 Seed.** The 1560 Seed laser is a narrow laser that seeds the NuFern amplifier, which amplifies the 1560 nm power to be frequency doubled to 780 nm. This 780 nm light is utilized for several purposes including absorption imaging, locking to the ultrastable cavity, and probing the 780 nm twisted cavity during the probe portion of the experimental sequence (Section **??**). Not all 1560 nm light is frequency doubled, and this remaining light is typically used for locking the 780 nm twisted cavity, or is stolen for use in the other Simon Lab experiments. Watch out for those light thieves from the other experiments. The 1560 Seed laser can sometimes drift in temperature, affecting the output power and causing the NuFern amplifier computer interface to claim its seed power is too low. If this drift occurs, the temperature can be changed using keyboard commands via a serial interface with the laser that can be opened in the Arduino software, for example.

- **NuFern Laser.** While not a laser per say, the NuFern Laser is a fiber amplifier that amplifies the 1560 Seed laser to $\sim$2 W.

- **480 Laser.** The 480 Laser excites the $5P_{3/2} \leftrightarrow$Rydberg transition in ^{87}Rb via injection into the 480 nm twisted cavity. The 480 Laser is an external-cavity diode laser, in which 960 nm light is frequency doubled to 480 nm in a second-harmonic generation cavity.

A small amount of 960 nm light that comes out a side port is used to lock this laser to our ultrastable cavity. By sticking an allen wrench into the appropriate hole of this laser, you can flip an internal beamsplitter cube up into the internal laser paths such that the laser outputs all the 960 nm light instead of 480 nm light in the event you want to use a lot of 960 nm light for something. By sticking a different allen wrench into a different hole of this laser, you can also rotate an internal grating to change the output frequency. This procedure becomes necessary when changing the Rydberg level to which you want to excite and will require some minor realignment as changing the grating angle affects the 480 nm output alignment. To realign the 480 nm output to the 480 nm optics downstream, one can walk the beam's position and angle using two tip-tilt mirrors immediately after the 480 nm laser output.

- **Lattice Seed.** The Lattice Seed seeds the Lattice TA with ∼35 mW. It is far red-detuned from the D2 line, providing dipole trapping for ^{87}Rb atoms. We historically did not lock this laser because of its large detuning, but eventually started locking this laser to the ultrastable cavity to investigate lattice lifetime improvements.

- **Lattice TA.** The Lattice TA amplifies the Lattice Seed, yielding ∼250 mW going into the main chamber. This power is utilized to create the vertical lattice (VLAT), elliptical lattice (ELAT), and cavity optical dipole trap (CODT). The VLAT vertically transports atoms from the MOT to the intersection between the 780 nm and 480 nm twisted cavities, then the elliptical lattice then loads these atoms into a flat, pancake-like shape to prevent more than one Rydberg excitation. The CODT is not always utilized in the experimental sequence, but can potentially be used to increase the atomic density, enhancing the collective atom-cavity coupling $g\sqrt{N}$.

- **Brady.** Brady is the seed laser for Gronk.[2]

2. Our postdoc, Logan, was a Patriots fan.

- **Gronk.** Gronk is the erbium-doped fiber amplifier (EDFA) for Brady. Gronk can output several watts of power at 1529 nm, which has typically been used to AC Stark shift the $5P_{3/2}$ level via the $5P_{3/2} \leftrightarrow 4D_{5/2}$ and $5P_{3/2} \leftrightarrow 4D_{3/2}$ transitions. This 1529 nm light was used for both Floquet modulation (Chapter 5) and optical mode conversion (Chapter 6).

- **1011 Laser.** This laser was intended to be used for a magic optical dipole trap. However, attempting to get this laser to operate robustly proved rather labor-intensive, and this project was eventually terminated [39].

4.3.2 Ultrastable cavity

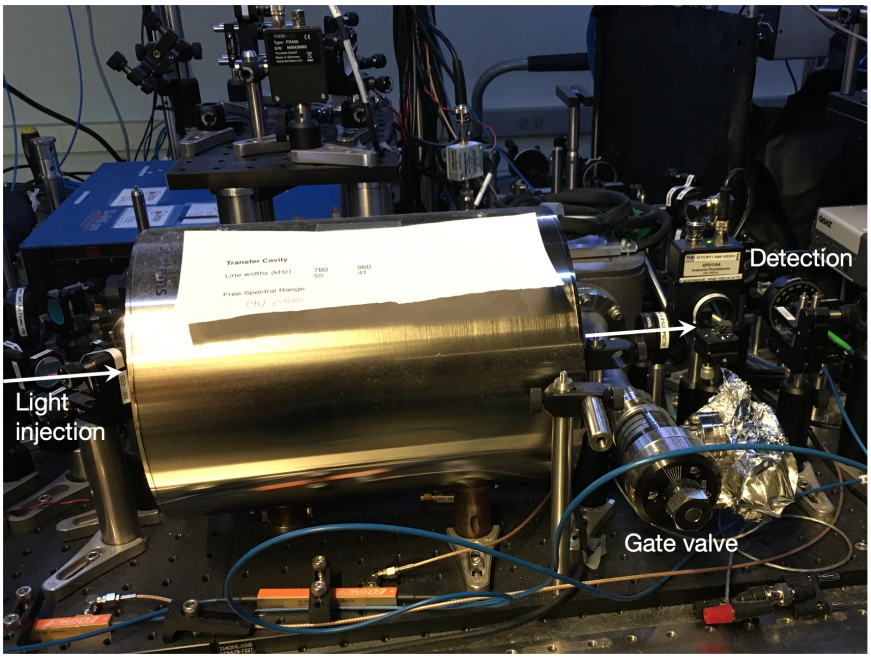

Figure 4.10: **Ultrastable cavity.**

What is the thing? Our ultrastable cavity is VH6020-4 from Stable Laser Systems. The cavity is essentially two mirrors (coated for 780 nm and 960 nm) that have been optically contacted to a tube composed of two different materials with opposite coefficients of thermal expansion to keep the cavity length constant. This cavity is under vacuum and needs to

be temperature stabilized, and is thus controlled by a temperature controller and ion pump controller.

Why do we have it? The ultrastable cavity acts as a stable reference for laser locking. We have historically locked the 480 Laser (via the 960 nm light it produces), the 1560 Seed (via the 780 nm light it produces), and the Lattice Seed to this cavity.

4.3.3 Digital micromirror device (DMD)

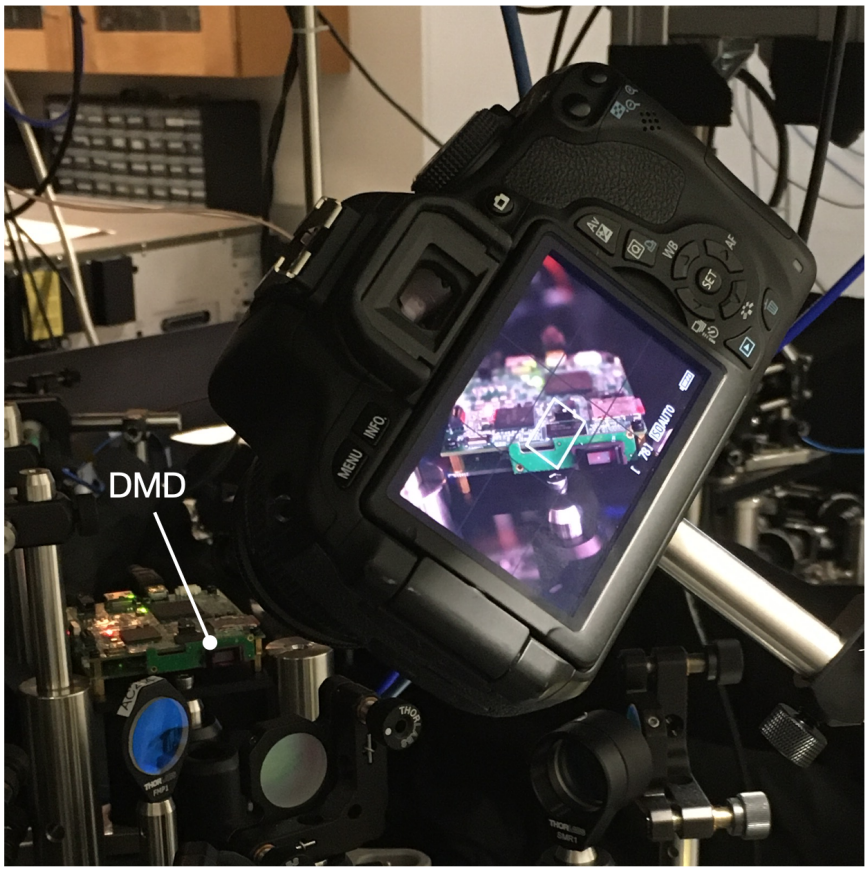

Figure 4.11: **Digital micromirror device.** This view is rather interesting as it captures the view of our DMD through a DSLR camera that has its IR filter removed. If you look closely, you can see a Gaussian pattern on the DMD surface that shapes the incoming beam.

What is the thing? Our main digital micromirror device (DMD) is the DLP3000 chip from Texas Instruments, a 608×684 grid of small mirrors that can be tilted "on" or "off."

In general, these chips are extracted from DLP LightCrafter Evaluation Modules. We can upload custom bitmap images to be displayed on the DMD face using customized Python code. Another DMD like the DLP4500 may not be compatible with this code, however there are likely online resources already for interfacing with other DMDs using Python or pre-existing GUIs.

Why do we have it? We use our DMD primarily to mode match into desired Laguerre-Gaussian eigenmodes of the 780 nm twisted cavity. Before mode matching, we additionally create a "phase map" to correct for optical aberrations imparted by optics between the DMD and the cavity injection mirror. The efficiency of the DMD is rather atrocious; only about $\sim 1\%$ of the incident light is converted to the desired mode. However, this efficiency is all right as we desire near-single photon injection into the cavity, requiring an extraordinarily attenuated 780 nm beam anyway.

4.3.4 Single photon counting modules (SPCMs)

What is the thing? We have several single photon counting modules (SPCMs) from Excelitas Technologies (e.g. SPCM-AQRH-13-FC-ND, SPCM-AQRH-14-FC-ND).

Why do we have it? We use these SPCMs to count the photons that exit the 780 nm twisted cavity, providing all of our data. In experiments that are sensitive to the dead time of these SPCMs like time correlation measurements, we split the twisted cavity output between two SPCMs using a fiber splitter. In experiments that are power-sensitive, the nonlinear response of the SPCMs must be calibrated.

Figure 4.12: **Single photon counting modules.** We keep our SPCMs buried under many layers of foil because they are *very* sensitive to light. Never expose a powered-on SPCM to room light—it will get toasted! Always power off SPCMs in the event you think they will be exposed to light above their specified acceptable count rates.

4.4 The experimental sequence

In this thesis, our goal is to trap a cloud of atoms inside our vacuum chamber, cool them, transport them up into the twisted cavity structure, and hold them at the lower waist of the 780 nm twisted cavity after some additional cloud shaping, cooling, and optical pumping. From here, we can send in 780 nm photons to create topologically ordered states until the atom number decreases sufficiently to warrant executing this cycle once more. We call this cycle "the sequence." The sequence is a fluid beast and is executed via a home-built Python 3 interface dubbed "Front Panel." The Front Panel architecture was designed to be highly

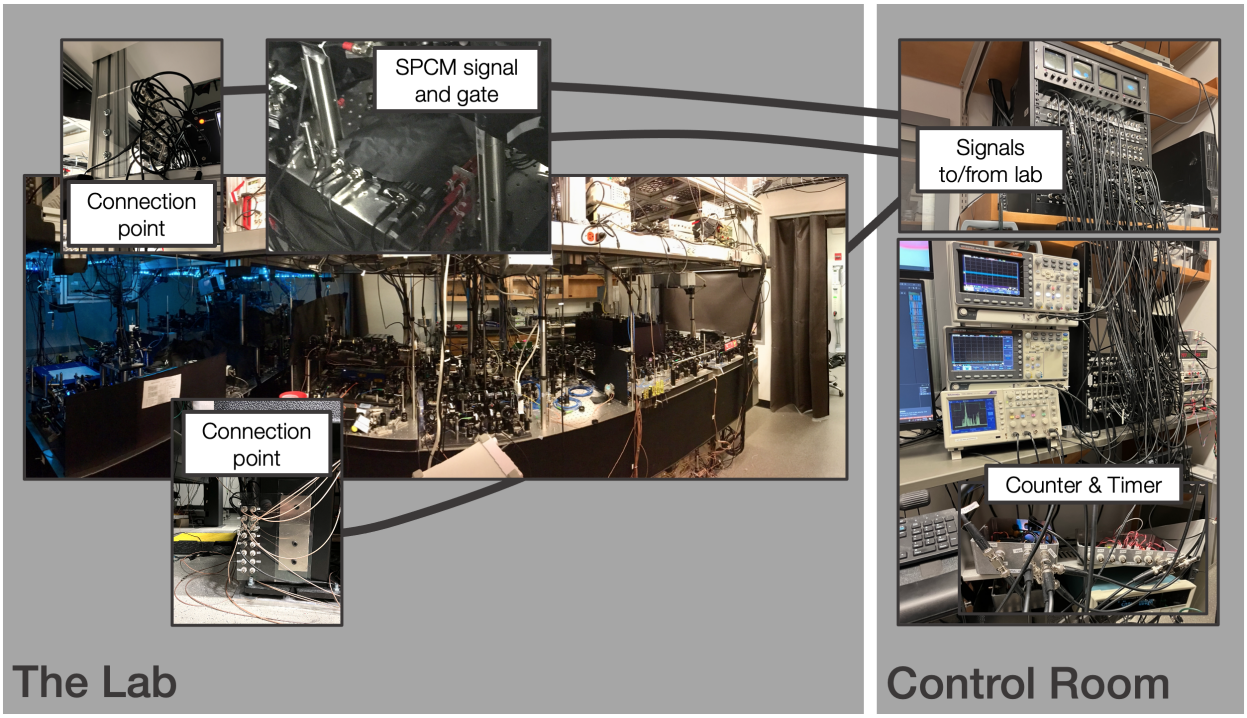

Figure 4.13: **Connections between the lab and control room.** We have a single computer in our control room that runs the experiment. It contains an analog card and a digital card by National Instruments that generate signals to be sent to devices in the lab via BNC cables. There are a number of "connection points" for devices to plug into to send signals to or receive signals from the control room, which is particularly convenient when installing new devices. Signals from our SPCMs return to the control room, also by BNC cables, and connect to the timer or counter FPGAs. These FPGAs are connected via USB to the control computer.

modular, such that if one decides they want to control an additional piece of equipment in the lab, it can be added as a new channel in the code and linked to modifiable variables—or MVs—in the Front Panel GUI. Typically, we call each run of the sequence a "shot," where sweeps over MVs can be programmed for a collection of shots so we can observe trends and optimize various sequence steps. Each shot is about 300 ms long, with 200 ms of sample preparation and 100 ms of data collection.

While the sequence is ever-changing based on our experimental needs, this section will overview the major sequence steps that are relatively unchanging.

4.4.1 Sample preparation

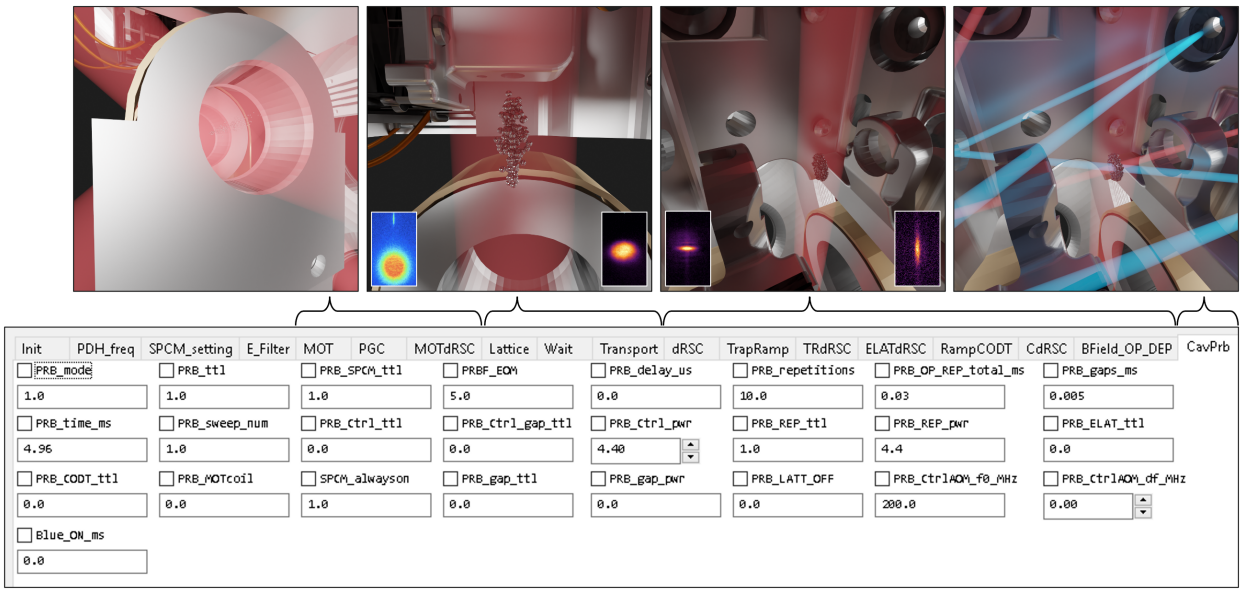

Figure 4.14: **The sequence.** A portion of our Front Panel GUI is displayed—including the various tabs associated with our sequence steps—along with visualizations of what is happening in the experiment during these steps. The second visualization contains two insets: a fluorescence image of our MOT and transporting atomic cloud (left) and an absorption image of atoms in the VLAT at the lower cavity waist (right). The third visualization contains another two insets: an absorption image of atoms in the ELAT at the lower cavity waist (left) and an absorption image of atoms in the CODT at the lower cavity waist (right). There are several tabs not explained in the main text of this thesis, such as Init, PHD_freq, SPCM_setting, and E_Filter. The MVs controlled in these tabs are important for setting the cavity lockpoint and twisted cavity structure electrode voltages, for example, but are not strictly part of preparing the atomic sample.

The list below describes the main steps of our experimental sequence in time order:

- **MOT.** This step controls the formation of our magneto-optical trap (MOT), which initially traps a cloud of atoms floating around our vacuum chamber, using our MOT Laser and Repumper Laser. The parameters we control through Front Panel are primarily laser powers, laser detunings, and the magnetic fields produced by our MOT coils and bias coils. The MOT is about 1 mm in diameter and should be visible via an IR camera. It takes ∼1 second to load the MOT completely, so the atom number will

likely fluctuate depending on the MOT loading time and if there is a long time gap between runs. A normal MOT temperature is ballpark $\sim$100 μK. This temperature is below the expected Doppler limit for a MOT due to PGC-like effects. Measurements of this temperature can be achieve via a time-of-flight experiment, in which the MOT is released after atoms have been loaded and fluorescence images of the expanding atom cloud are captured. The temperature of the cloud can be extracted by fitting the cloud's diameter over time—hotter clouds will expand faster!

- **PGC.** This step controls the cooling of our MOT via polarization gradient cooling (PGC) [45], again using our MOT Laser and Repumper Laser, to cool atoms into our transport lattice. The mechanism behind PGC takes some time to fully understand, but the overall gist is that two counterpropagating beams of orthogonal polarizations—in our case, σ^+ and σ^-—create a polarization gradient in space. The energy levels of atoms traveling along this polarization gradient experience a spatially-dependent shift. This shift can be harnessed so that atoms are excited then decay to a lower energy, causing cooling. A normal MOT temperature after PGC is 5-10 μK, which can again be measured via a time-of-flight experiment. A temperature of 25 μK is all right, but typically colder should be achievable.

- **Lattice.** This step controls the light from the Lattice TA via AOMs—namely, the power and whether the light is on or off (TTL). During PGC, the atoms are loaded into what we call the VLAT—the vertical lattice—which is a lowest-order Gaussian beam that is vertically retroreflected to form a standing wave that holds the atoms via dipolar forces. AOMs controlled in this step are used for frequency shifting the retroreflected beam, thereby causing the standing wave to move, in turn transporting the atoms.

- **Transport.** This step controls the what occurs during the vertical transport of the

atoms up into the cavity such as the acceleration of the atoms, the transport distance, pauses during the transport period, and various laser parameters. Fluorescence imaging of the atoms in the MOT region can be quite useful in debugging the transport step. For example, imaging can tell you if atom transport is occurring at all and how well the VLAT can hold the atoms.

- **dRSC.** This step controls degenerate Raman sideband cooling (dRSC). This cooling is performed to improve atom retention while simultaneously optically pumping the atoms. This step is performed using our Lattice TA, D1 Laser, and HLAT laser, which together pump the atoms into the lowest vibrational level of the $5S_{1/2}$ ($F = 2$) stretched state. The HLAT—or, horizontal lattice—is a detuned 780 nm laser that is split into two paths, each incident on the atoms through holes in the twisted cavity structure. One path is retroreflected and one is running wave. Between the two horizontal lattice paths and one vertical lattice path, a 3D lattice is made for the atoms with some trap frequency that sets the vibrational energy level spacing. The normal atomic cloud temperature after dRSC is $\sim$0.5 μK. See Reference [39] for additional details.

- **TrapRamp.** This step controls the transfer of atoms from the VLAT to the ELAT—the elliptical lattice, which also utilizes Lattice TA light. This transfer shapes the atomic cloud into a 2D pancake such that the blockade effect due to a single Rydberg atom is strong. After transferring the atom cloud to the ELAT, its width along the 780 nm twisted cavity axis is 10 μm.

- **RampCODT.** This step controls the ramp on of the cavity optical dipole trap (CODT). This step has not always been utilized, but has been more recently utilized with the intention of increasing the atom density. Lattice TA light is sent through the 780 nm twisted cavity path, providing compression at the lower cavity waist via dipolar forces.

- **BField_OP_DEP.** This step primarily controls a magnetic field ramp—using the

bias coils—such that there is a well-defined quantization axis while probing the cavity with 780 nm photons. This step additionally controls optical pumping and depumping parameters to maintain a constant atom number throughout long probe times.

- **CavPrb.** This step controls the probing of the cavity. It is during this cavity probe time that topologically ordered states are created and measured using our SPCMs. Figure 4.14 depicts the CavPrb tab in Front Panel, which contains many MVs for controlling the probe time, probe power, whether the 480 nm light is on or off, the 480 nm power, and so on. The probe light is quite weak and is provided by our frequency-doubled Nufern Laser.

4.4.2 Data collection

Our data collection is primarily counting photons over time. During the CavPrb step, we enable our SPCMs and they collect 780 nm photons that leak out of the 780 nm twisted cavity. Signals from the SPCM are sent from the lab to our control room via long BNC cables. These signals can then connect to the input of one of two Opal Kelly XEM6001 FPGAs: one which counts the number of photons detected within a specified time bin—the "counter"—and one which assigns a time tag to every photon detected at 1.4 ns resolution—the "timer."

The counter FPGA is used primarily in collecting cavity spectra, where the high temporal resolution of the timer is not particularly necessary. The timer FPGA is used primarily for measurements where high temporal resolution is necessary, such as for Rabi oscillations or temporal correlations. After the data are collected, all post-processing is performed in Python.

Much of the data we collect actually goes toward experiment calibration and optimization. Figure 4.15 depicts a number of measurements we perform to evaluate our experimental performance, optimize quantities such as the electric field, and extract relevant parameters.

In parametric heating, we "shake" the lattice by modulating one of the frequency-shifting lattice AOMs in the retroreflected arm. At twice the lattice trap frequency, a dip appears as atoms are shaken out of the lattice. Performing this measurement at various atom transport distances can even reveal the lattice waist location! We can additionally sweep the electric fields in the x, y, and z directions. Remember, atomic levels shift quadratically for small electric fields. We can use this fact to find the electrode voltages that zero the electric field by observing the spectral location of the dark polariton as a function of electrode voltage values. In the electric field scans in Figure 4.15, we claim the electric field is approximately zero for Ex, Ey, and Ez values near the center of their respective y-axes. Time of flight is used to extract the temperature of our atomic cloud by fitting Gaussian functions to the freely moving cloud shape in images over time—hotter clouds expand faster! Holding atoms in the VLAT or ELAT reveals their respective lattice lifetimes—acquired by either imaging or measuring the VRS splitting over time. Lastly, the "hotwire" effect can be a useful tool for aligning the atomic cloud to the 780 nm cavity mode. This effect can be achieved by transporting atoms vertically through strong, near-resonant probe light sent through the 780 nm cavity, effectively blasting the atoms away. This effect is most useful when the alignment of the atoms to the cavity is already fairly good and when one is interested in fine-tuning.

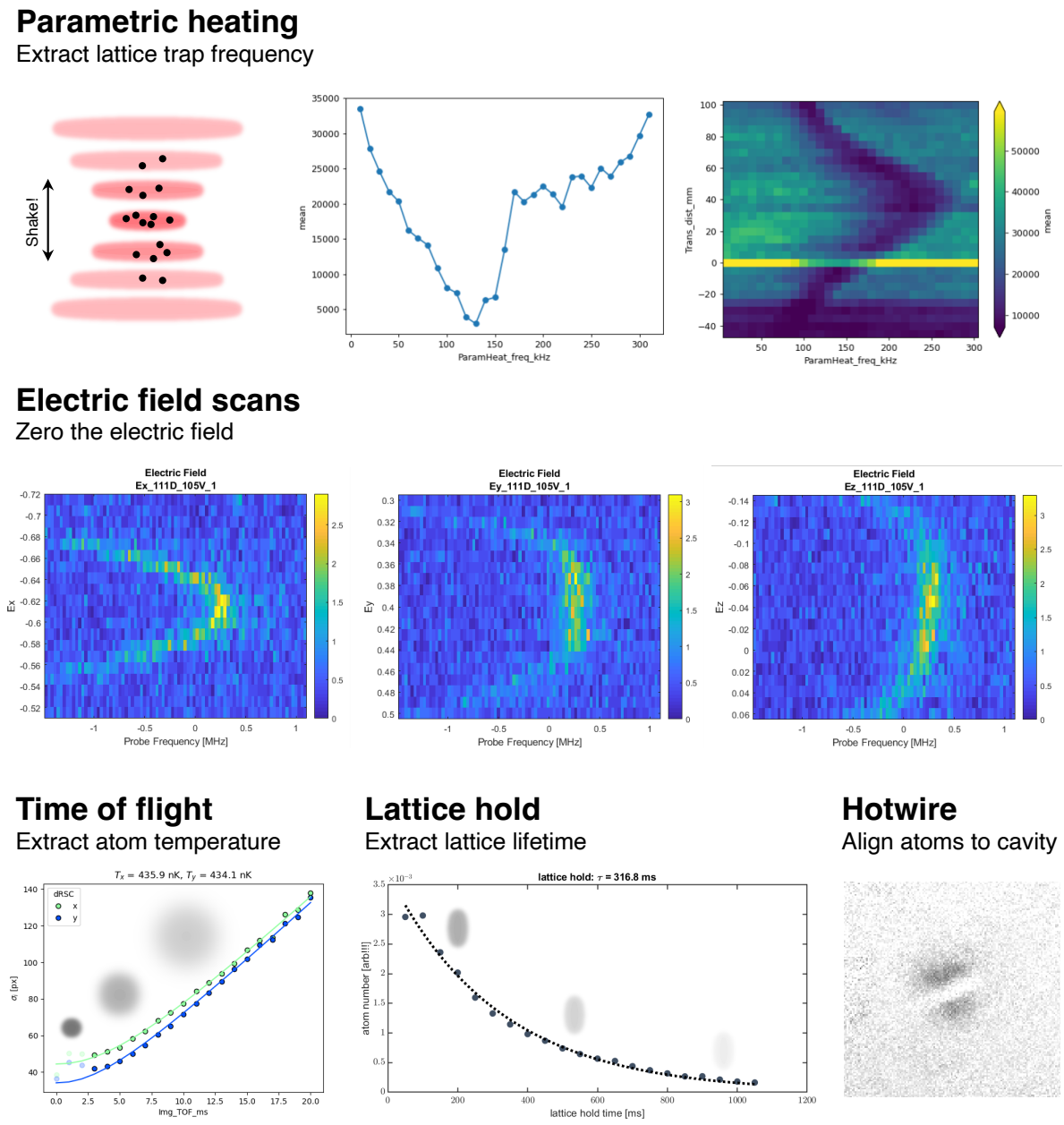

Figure 4.15: **Diagnostic procedures.** This figure depicts a variety of diagnostic experiments we run to extract useful quantities, evaluate performance, and optimize experimental parameters.

CHAPTER 5

QUANTUM MATERIALS MADE OF LIGHT

Sections 5.1 and 5.2 are based off of references [46, 44]:

Interacting Floquet polaritons.

L. W. Clark, N. Jia, N. Schine, C. Baum, A. Georgakopoulos, and J. Simon, *Nature* 571, 532–536, (2019).

Observation of Laughlin states made of light.

L. W. Clark, N. Schine, C. Baum, N. Jia, and J. Simon, *Nature* 582, 41-45, (2020).

Section 5.3 is based off of references [47, 48]:

Aberrated optical cavities.

M. Jaffe, L. Palm, C. Baum, L. Taneja, and J. Simon, *Physical Review A*, 104, 013524, (2021).

Understanding and suppressing backscatter in optical resonators.

M. Jaffe, L. Palm, C. Baum, L. Taneja, A. Kumar, and J. Simon, *Optica*, 9, 878-885 (2022).

5.1 Motivation

5.1.1 Topological order and the fractional quantum Hall effect

Back in the 1940s, Lev Landau developed an incredibly successful general theory of orders and their transitions that seemingly described all the various states of matter around us [1]. Enter the fractional quantum Hall (FQH) effect, discovered experimentally in 1982, which could not be described by Landau's theory (Figure 5.1). Rather, this effect is described by *topological order*, corresponding to patterns of long-range quantum entanglement [2]. Thus

began a new chapter of condensed matter physics and the study of topologically ordered many-body states. These states exhibit fascinating properties largely unseen in other forms of matter; for example, in addition to the robust quantized edge transport which also appears in weakly-interacting systems [49], topologically ordered phases can host excitations with fractional charge and anyonic exchange statistics [50]. More exotic phases can even host non-Abelian anyons, a promising constituent for fault-tolerant quantum computers thanks to their insensitivity to local perturbations [3].

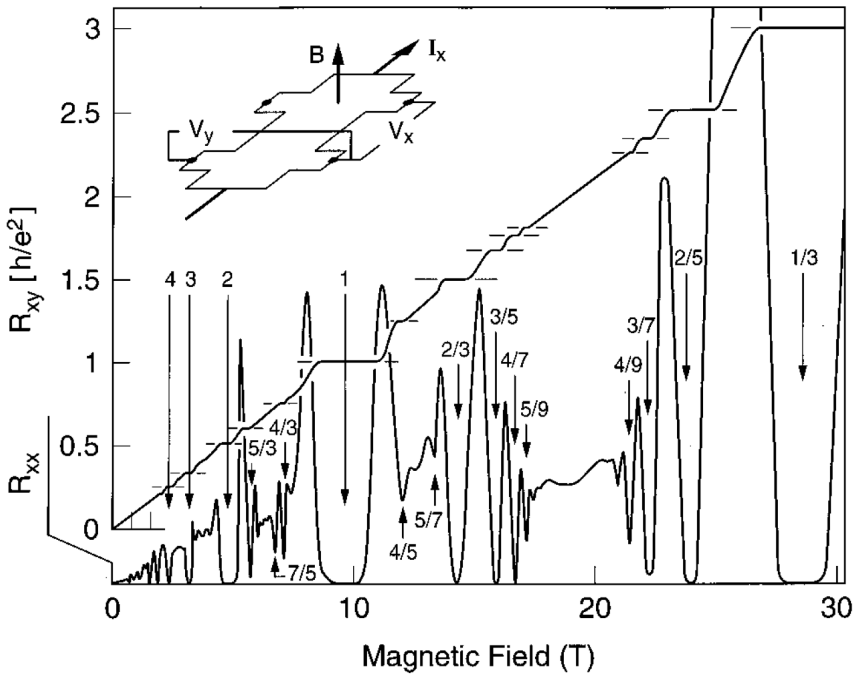

Figure 5.1: **The fractional quantum Hall effect.** Topological order emerges in two-dimensional sheet of metal pierced by a magnetic field, B, and containing a current I_x. The quantum nature of this system is evidenced by plateaus in the Hall resistance, $R_{xy} = V_y/I_x$, as a function of the magnetic field. The magnetoresistance, $R_{xx} = V_x/I_x$, is superposed. Figure from [51].

The simplest recipe for realizing topologically ordered many-body states is to place strongly-interacting particles in an effective magnetic field. However, few experimental systems have been found to host topologically ordered states. All definitive observations of such order have been made in two-dimensional electron gases subjected to magnetic fields, origi-

nally in semiconductor heterojunctions [52], as well as more recently in graphene [53, 5, 54] and van der Waals bilayers [55].

The scarcity of physical platforms hosting topological order has spurred great interest in elucidating its exotic properties using the wide tunability, particle-resolved control, and versatile detection capabilities afforded by synthetic quantum materials [56, 57, 58, 59]. The constituents of typical synthetic materials are atoms and photons, which do not experience a Lorentz force in ordinary magnetic fields because they are charge neutral. Therefore, the key challenge is to implement a synthetic magnetic field which creates an effective Lorentz force and is compatible with strong interactions between particles. A classic approach employed the Coriolis force in rotating ultracold atomic gases [60], and such systems approached the few-body fractional quantum Hall regime [61]. More recent efforts in ultracold atoms focused on Floquet engineering of synthetic magnetic fields [62] combined with strong atomic interactions thanks to tight confinement in an optical lattice [63]. Furthermore, coupling atomic gases with multiple modes of optical resonators provides exciting opportunities for studying many-body physics [64, 65, 66, 67, 68, 69]. Photonic systems have also demonstrated a variety of synthetic magnetic fields [58] compatible with strong interactions via coupling to superconducting qubits in the microwave domain [70, 71] and cold atoms [72, 73, 74, 75] or quantum dots [76] in the optical domain. Because these ingredients have yet to be effectively combined and scaled, the formation of topologically ordered synthetic materials has remained elusive.

We seek to combine the elements presented in this thesis—atoms and cavities—to experimentally create and probe topologically ordered quantum materials made of light. In this chapter, we use a multimode, twisted optical cavity to generate a synthetic gauge field for light [58, 77, 78, 79, 80, 81] and cavity Rydberg polaritons to mediate photon-photon interactions. Making photons interact strongly in this cavity enables us to study strongly correlated fractional quantum Hall states of light, namely *Laughlin states*, the grounds states

of a fractional quantum Hall system [82, 83, 84, 85, 86, 87, 88, 89].

5.2 Combining atoms and cavities

In this section, we describe the formation of optical photon pairs in a Laughlin state. To this end, we construct a photonic system analogous to an electronic fractional quantum Hall fluid by combining two key ingredients: a synthetic magnetic field for light induced by a twisted optical cavity [79] and strong photonic interactions mediated by Rydberg atoms [75].

We first observe that photons in this system undergo collisions which satisfy conservation laws and have density-dependence characteristic of two-body processes. A closer examination of the resulting two-body correlations reveals a two-photon angular momentum distribution consistent with a Laughlin state. Moreover, characterizing these photon pairs in real space reveals that they strongly avoid being in the same location. Together, these results indicate the formation of photon pairs with 76(18)% overlap with a pure Laughlin state.

5.2.1 Interacting photons in a magnetic field

In our experiment, combining atoms and cavities results in cavity Rydberg polaritons, quasiparticles composed of part cavity photon and part atomic Rydberg excitation. The Rydberg component facilitates strong interactions between polaritons [90], while the cavity component allows us to shape the polariton energy landscape via the mode structure of a twisted optical cavity. This combination results in effective photon-photon interactions in a magnetic field, mimicking the conditions for an electronic fractional quantum Hall system (Figure 5.2). The motion of individual polaritons is determined by the cavity modes accessible to their photonic part [91]. The large energy spacing between longitudinal cavity manifolds restricts the polaritons to a single manifold, confining them to undergo two-dimensional motion among its transverse modes. Interactions between polaritons occur via Rydberg blockade and can be characterized via the two-photon correlation function $g^{(2)}(\tau)$ that quantifies the likelihood

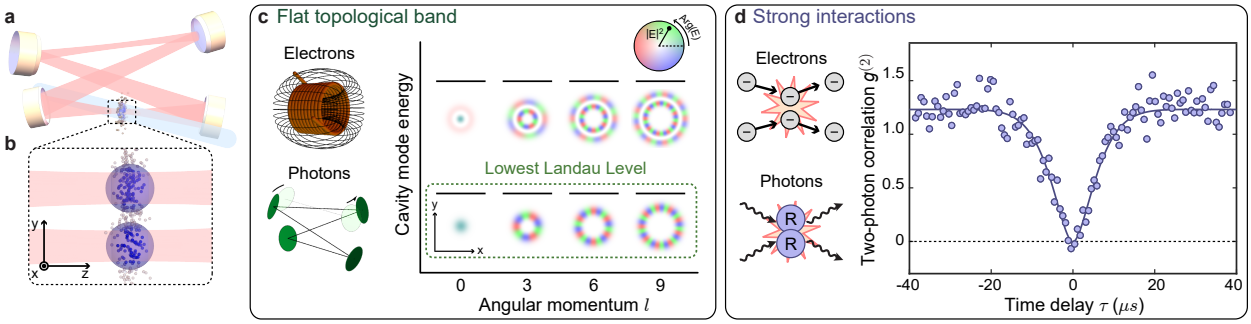

Figure 5.2: **Ingredients for Laughlin states made of light. a,** Our experiment couples optical photons (red) with a gas of 6000(1000) laser-cooled Rubidium-87 atoms at the waist of twisted, four mirror optical cavity. We continuously shine a weak probe laser beam on the cavity for 100 ms. The initially uncorrelated photons from the probe laser which enter the cavity are strongly coupled with an additional Rydberg coupling field (light blue) to a resonant atomic transition. **b,** This coupling turns each photon entering the cavity into a *polariton*, a quasiparticle combining the photon with a collective Rydberg excitation of the atomic gas. Polaritons can move around in the transverse modes available to their photonic component, and a pair of polaritons (depicted) strongly interacts because of their Rydberg components (blue spheres). **c,** Two key ingredients enable this system to explore topological order. First, we form a flat topological band of single-photon states using a twisted optical cavity, which hosts a set of degenerate photonic modes that are equivalent to the states in the lowest Landau level available to electrons in a strong magnetic field. **d,** Second, the strong polaritonic interactions are analogous to the Coulomb interactions between electrons in a traditional fractional quantum Hall system. Polaritons confined to a single cavity mode reveal their strong interactions via transport blockade, in which a single polariton present in the cavity prevents a second photon from entering. Blockade results in antibunched correlations of photons exiting the cavity, shown here for $l = 0$. Figure taken from [44].

of seeing two photons emerge from the cavity separated by a time τ compared to completely uncorrelated photons. Blockade manifests strikingly through anti-bunching; the same-time correlation $g^{(2)}(0)$ falls to zero because there are never two polaritons present in the cavity simultaneously.

We utilize Floquet engineering in our twisted optical cavity to form a set of three degenerate orbital angular momentum modes equivalent to the lowest Landau level accessible to electrons in a magnetic field [92, 46], resulting in 2-particle Laughlin states made of light.

5.2.2 *Floquet engineering*

As mentioned in Chapter 4, the twisted cavity used in this work—the Original Twister—was unable to bring many orbital angular momentum modes into degeneracy as a result of optical aberrations. However, we were able to bring three modes, $l = 3,\ 6$, and 9, effectively into degeneracy by modulating the atoms at the frequency difference between orbital angular momentum modes away from the intended degeneracy point.

Figure 5.3 depicts our "usual," unmodulated experimental setup in terms of the atomic levels of ^{87}Rb we excite to create Rydberg polaritons—the flavors of which are "bright" and "dark." Dark polaritons are comprised only of a 780 nm cavity photon and the atomic Rydberg state, thus "dark" to the lossy $5P_{3/2}$ level. We excite dark polaritons by injecting 780 nm photons at the frequency where the occur spectrally, inducing blockade and effective photon-photon interactions.

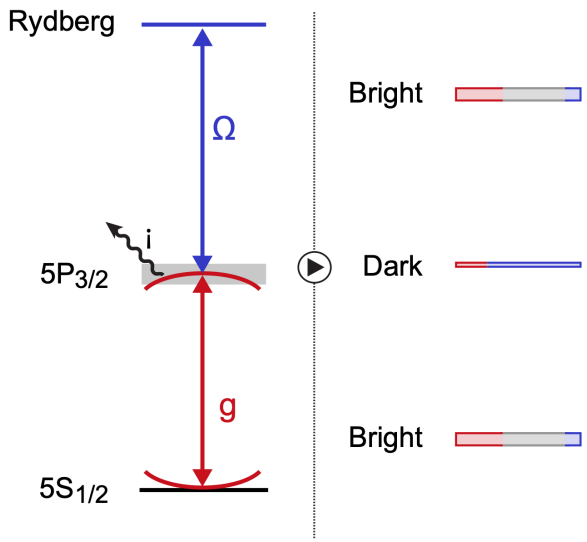

Figure 5.3: **The usual atomic levels.** The $5S_{1/2} \leftrightarrow 5P_{3/2}$ transition is excited by 780 nm photons in the 780 nm twisted cavity, and the $5P_{3/2} \leftrightarrow$Rydberg transition is excited by 480 nm photons in the 480 nm twisted cavity. This excitation configuration gives us electromagnetically induced transparency (EIT), producing two types of Rydberg polaritons—"bright" and "dark."

For a non-degenerate cavity, however, the $5P_{3/2}$ state cannot be resonant with multiple

modes unless we do something about it as the $5P_{3/2}$ state occurs at a single frequency, whereas the cavity modes occur at multiple different frequencies. As demonstrated in [46], Floquet engineering can be used to effectively create frequency sidebands on the $5P_{3/2}$ atomic state using an AC Stark-shirting modulation beam to solve this problem (Figure 5.4). In the case of creating Laughlin states made of light, a 1529 nm modulation beam was used to couple the $5P_{3/2}$ to nearby D states, giving the $5P_{3/2}$ state frequency sidebands at the frequency difference between every third orbital angular momentum mode.

5.2.3 Laughlin states made of light

The Floquet engineering techniques of the previous subsection were used the couple the $5P_{3/2}$ state to the $l = 3,\ 6$, and 9 orbital angular momentum eigenmodes of the twisted cavity, leading to three separate EIT features in Figure 5.5b.

When polaritons have access to multiple transverse modes, in our case in the lowest Landau level of $l = 3,\ 6$, and 9, new physics emerges. It becomes possible for two polaritons to enter in the cavity simultaneously while still avoiding one another: interactions need not lead to blockade, but can instead drive collisions between polaritons, causing them to move among the states of the Landau level and thereby reduce their interaction energy.

Despite the exotic nature of polaritonic quasiparticles, we find that they undergo collisions much like ordinary particles [82, 83, 84, 96]. In particular, collisions between polaritons conserve total energy, as well as angular momentum thanks to the rotational symmetry of the Landau level and interactions. Accordingly, the only collision process which conserves angular momentum converts two input polaritons with $l = 6$ into one output polariton with $l = 3$ and another with $l = 9$. Similarly, as we tune the relative energies between the different angular momentum states, we only observe photons emerging with $l = 3$ or 9 when the aforementioned collision process can conserve energy (Figure 5.5. Indeed, we observe that the rate at which collision products appear $R_{3,9} \propto R_6^2$ is quadratic in the rate R_6 at

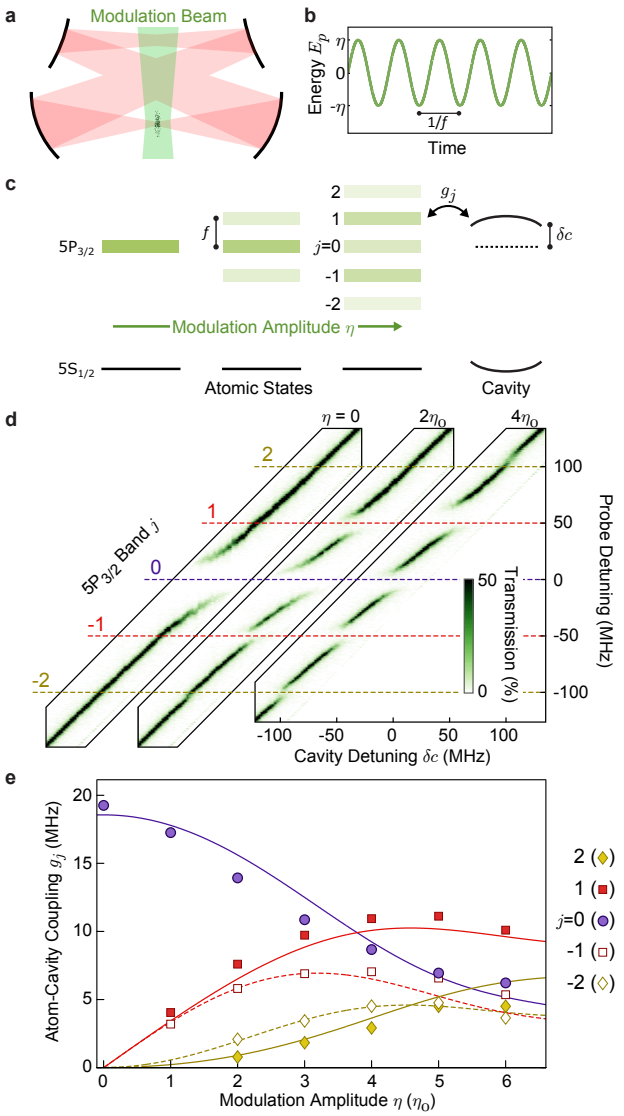

Figure 5.4: **Floquet engineering. a** depicts the 780 nm twisted cavity, atomic cloud, and modulation beam (green). **b,** The energy of the P state, E_p, is modulated in time due to a temporally-varying AC Stark shift of the atoms. This modulation creates sidebands on the $5P_{3/2}$ state (**c**) that can now couple to cavity modes at different frequencies. Increasing the modulation amplitude gives the effect of creating several new P states to which the cavity can couple, which are indicated by avoided crossings in the cavity spectra (**d**). Just as changing the modulation amplitude of an EOM changes the powers in the various frequency sideband orders for example, this concept applies to Floquet modulation as well (**e**). Figure taken from [46].

which photons emerge in the initial angular momentum state (Figure 5.5d).

To understand the ordering that can emerge due to collisions between polaritons, in

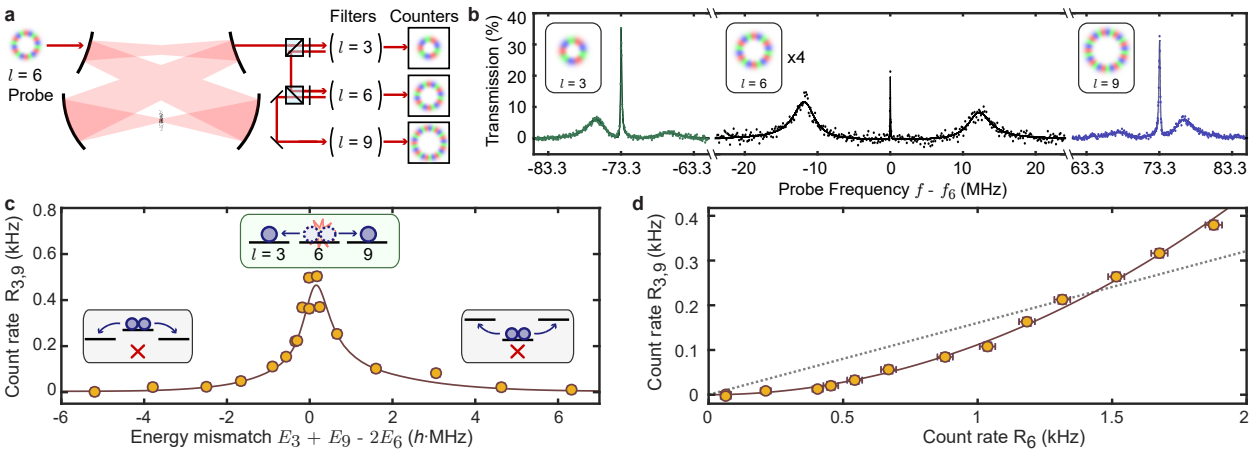

Figure 5.5: **Collisions between polaritons in $l = 3$, 6, and 9. a,** Schematic: To test for mode-changing collisions between polaritons, we inject photons with orbital angular momentum $l = 6$ and then count the photons emerging from the cavity in other angular momentum modes using mode sorting cavities. **b,** We perform spectroscopy of the single-polariton eigenstates by weakly injecting $l = 3, 6, 9$ photons and scanning their energies. We observe Floquet Rydberg polariton resonances [93] (three narrow peaks) for each of the three accessible lowest Landau level eigenstates, separated by ~ 73 MHz. The $l = 3, 9$ polaritons are more photon-like (broader & taller) than the $l = 6$ polariton (see text). We ignore the broad "bright" polaritons [94], as they do not interact [95], instead probing collisions of photons injected on the Rydberg polariton resonances. **c,** When $l = 6$ photons are injected into the cavity at a higher rate, the total rate $R_{3,9}$ at which photons emerge with angular momentum $l = 3$ or 9 peaks when the collisions conserve energy (**inset**); E_l is the angular momentum l polariton's energy. **d,** At zero energy mismatch, varying the photon injection rate reveals that $R_{3,9}$ grows quadratically (solid curve) rather than linearly (dotted line) with the rate R_6 of injected $l = 6$ photons, consistent with $l = 3$ and 9 polaritons produced in two-body collisions between $l = 6$ polaritons. Figure taken from [44].

Figures 5.6a and b we consider an idealized energy spectrum for zero, one, and two polaritons. We consider a "flat Landau level" where all single-polariton states $|l\rangle$ are degenerate, with energy E_{pol}. When only one single-particle eigenstate (for example, the $l = 6$ mode) is accessible, the interactions between polaritons that arise from their Rydberg components cause the state $|66\rangle$ with two polaritons in that mode to have a shifted energy and shorter lifetime absent such interactions [97, 98]. Thus, a probe laser which resonantly excites $|6\rangle$ from the vacuum state $|vac\rangle$ does not subsequently excite the $|6\rangle \rightarrow |66\rangle$ transition, leading to blockade and precluding the formation of multi-polariton states.

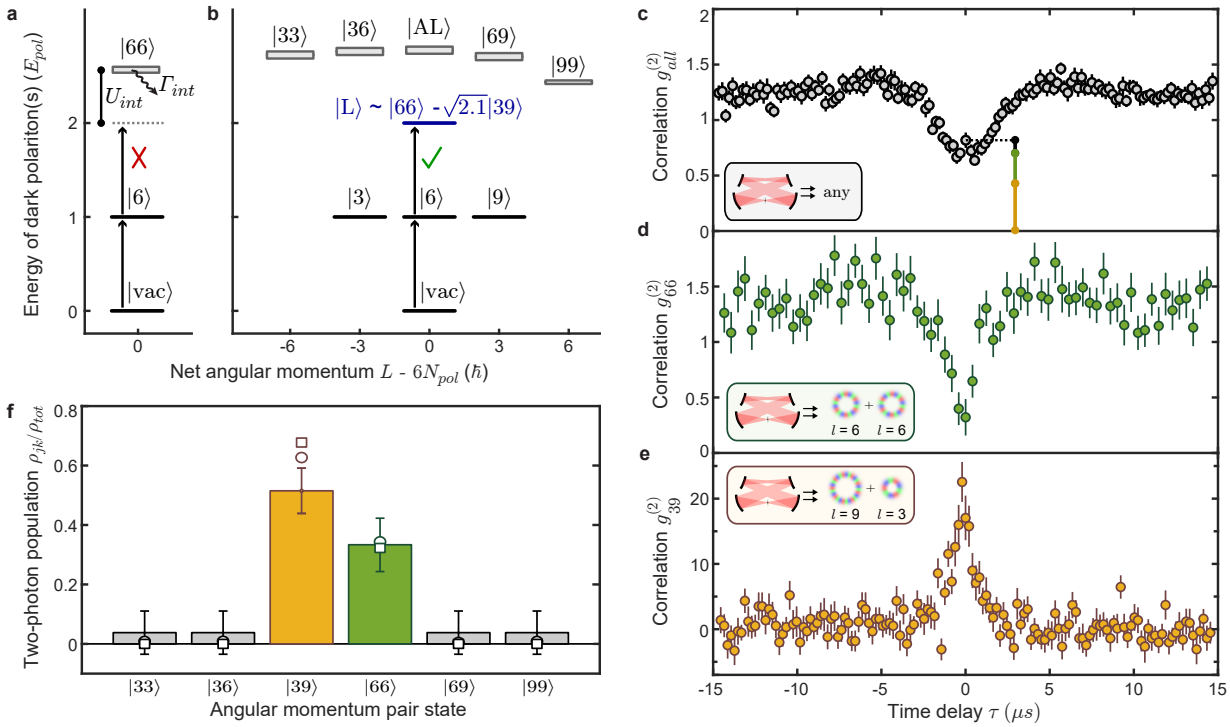

Figure 5.6: **Correlations in angular momentum space.** Schematic many-body energy spectrum for states containing polariton numbers $N_{\mathrm{pol}} \leq 2$ with each particle able to explore only a single mode (**a**) or three modes of the lowest Landau level (**b**). In a single mode (here $l = 6$), the polaritons cannot avoid each other, so the two polariton state $|66\rangle$ has its energy shifted (U_{int}) and rapidly decays (Γ_{int}) due to interactions; these effects induce blockade. With three modes accessible, most two-polariton states are still shifted by interactions. However, a Laughlin state $|L\rangle$ arises in which the interference between $|66\rangle$ and $|39\rangle$ reduces the interaction energy by keeping the particles apart. This pair state is longer-lived and thus preferentially excited by the $l = 6$ probe laser (black arrows). In practice, we study and measure correlations in the related but inequivalent optical quantum field emitted from the cavity: **c,** When all emitted photons are included regardless of angular momentum, photons with access to all three modes exhibit weak blockade. **d,** Correlations between photons with $l = 6$ exhibit stronger blockade, with remnant nonzero correlation $g_{66}(0) = 0.32(3)$ at zero delay. **e,** Photons with angular momenta $l = 3$ and $l = 9$ exhibit a large positive cross-correlation because they are produced together in collisions. **f,** Relative populations in the two-photon manifold determined from coincidence events (bars) are comparable to the Laughlin state (squares) and an atomistic numerical model [93] (circles). Vertical bars in panel **c** indicate the portion of $g^{(2)}_{\mathrm{all}}(0)$ accounted for by pairs in $|39\rangle$ (orange), $|66\rangle$ (green), and all other states (black). All error bars indicate standard error. Figure taken from [44].

In this idealized limit, providing the polaritons access to three single-particle eigenstates in the lowest Landau level leads to the emergence of a long-lived two-particle Laughlin state

$|L\rangle$ (Figure 5.6b). Our experiments offer a unique opportunity to connect the mathematical form of this Laughlin state to measurements of its microscopic structure. For the particular modes used in this work, the two-particle Laughlin wavefunction in real space is $\psi_{\mathrm{L}}(z_1, z_2) \propto z_1^3 z_2^3 (z_1^3 - z_2^3)^2 \exp\left(-|z_1|^2/4 - |z_2|^2/4\right)$ where $z_k \equiv x_k + i y_k$ is a complex number reflecting the position (x_k, y_k) of particle k. Expanding the polynomial prefactor lets us write this state in angular-momentum space as $|L\rangle = \frac{1}{\sqrt{3.1}} |66\rangle - \sqrt{\frac{2.1}{3.1}} |39\rangle$, where $|mn\rangle$ is the state with two polaritons of angular momenta $m\hbar$ and $n\hbar$. Because the wavefunction goes to zero when the particles are at the same position ($\psi_{\mathrm{L}}(z_1 = z_2) = 0$), occupying the Laughlin state enables two particles to avoid each other while remaining in the lowest Landau level. From the perspective of angular momentum states, this avoidance arises from destructive interference between the $|66\rangle$ and $|39\rangle$ two-particle amplitudes for co-located particles. Similar two-particle Laughlin states can be formed in any set of three evenly spaced angular-momentum states.

The spatial anti-correlation of polaritons in the Laughlin state suppresses the interaction energy and interaction-induced decay present in other two-particle states. Thus, for ideal polaritons, simply shining a laser into this atom-cavity system would cause a polaritonic Laughlin state to form inside, because all other two-polariton states are blockaded (including the "Anti-Laughlin" superposition state $|AL\rangle = \sqrt{\frac{2.1}{3.1}} |66\rangle + \frac{1}{\sqrt{3.1}} |39\rangle$).

The collisions observed in Figure 5.5 are the first hint of such ordering. The finite optical depth of our polaritons prevents them from reaching a polaritonic Laughlin state before decaying. Surprisingly, we can distill a high purity photonic Laughlin state outside of the cavity from the polaritonic state produced within the cavity: this is achieved by choosing Floquet conditions to make the $l = 3$ and $l = 9$ polaritons more photon-like than the $l = 6$ polariton (apparent from their larger width in Figure 5.5b), and correcting the phase imparted to the outgoing photons by the Floquet modulation.

To definitively test for the formation of these photonic Laughlin states we experimentally

investigate the correlations of the emerging photon pairs [89]. First, when we detect all output photons regardless of their spatial mode, the "all-mode" correlations $g^{(2)}_{\text{all}}(\tau)$ reveal only a weak blockade effect (Figure 5.6c).

This weak blockade confirms that photon pairs can traverse the three-mode cavity whereas they were blocked in its single-mode counterpart; determining the structure of the pairs requires more detailed measurements.

We gain deeper insight by examining the correlations $g^{(2)}_{jk}$ between photons with angular momenta $l = j$ and $l = k$, again using the setup shown in Figure 5.5a. The correlations $g^{(2)}_{66}$ between photons with $l = 6$ have a nonzero value $g^{(2)}_{66}(0) = 0.32(3)$ at zero time delay, indicating substantial population in the pair state $|66\rangle$ (Figure 5.6d). However, their blockade is still much deeper than that of the all-mode correlations $g^{(2)}_{\text{all}}$, indicating that the two-photon state has a large contribution from pairs not in the state $|66\rangle$. Most of the remaining pairs are accounted for by examining $g^{(2)}_{39}$, which exhibits a prominent peak at zero time (Figure 5.6e). The peak height indicates that photons are $g^{(2)}_{39}(0) = 22(2)$ times more likely to appear in both modes simultaneously than expected for uncorrelated photons arriving with the same individual rates. This bunching arises because photons in these modes are predominantly produced together from polaritonic collisions and rarely injected independently. Unlike parametric collision processes observed in non-linear crystals requiring macroscopic mode populations [99], collisions in our system appear for *just two* intracavity polaritons.

We quantitatively compare the observed pair-photon state with the Laughlin state by calculating the two-particle populations ρ_{jk} with angular momenta j and k from the coincidence rates of events where two photons are observed near-simultaneously (Figure 5.6f). Coincidence events corresponding to $|66\rangle$ or $|39\rangle$ account for 85(15)% of all observed photon pairs, consistent with angular momentum conservation. Moreover, the ratio $\rho_{39}/\rho_{66} = 1.5(5)$ of pair populations is near the intended ratio of 2.1 for the Laughlin state. Deviations from ideal populations could arise from the limited lifetime and interaction strength of our po-

laritons, slight drifts of system parameters between experiments, or because the polaritons with angular momentum $l = 3$ and 9 are insufficiently photon-like.

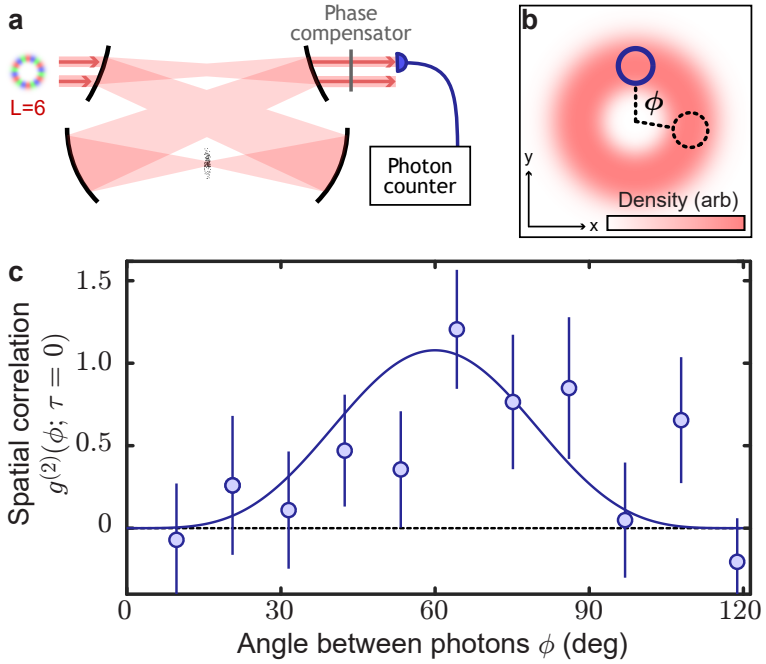

Figure 5.7: **Correlations in real space.** **a,** A single-mode fiber (purple) admits only photons at its location, enabling us to filter photons by their real-space position. A mode-dependent phase compensator counteracts the phase difference between polaritons and photons imprinted by our Floquet scheme. **b,** The average density of photons forms a smooth annulus with no angular structure. We place the fiber off-center (solid circle) at the radius with the highest density and measure correlations as a function of the angle ϕ to a second location (dashed circle) around the annulus. **c,** The measured angular correlations (circles) for zero time delay exhibit a periodic structure. The minimum of correlation near $\phi = 0$ reveals that photons avoid being in the same location. The solid curve is a fit to the function $g^{(2)}_{\text{fit}}(\phi) = g_0 + g_1 \sin^4(3\phi/2)$ (see text). Error bars indicate standard error. Figure taken from [44].

We next test for the remaining essential physical feature of Laughlin states: that the photons avoid each other in real space. As a bonus, such spatial correlations directly quantify the off-diagonal elements of the pair-state density matrix. To measure in real-space we filter the photons exiting the cavity with a single-mode optical fiber (Figure 5.7a) that only admits photons at the location of its tip. Thus, to count photons at a particular position, we simply place the fiber tip there. Since the average density in a state composed of $|39\rangle$ and

$|66\rangle$ forms a smooth annulus, we translate the fiber to the radius with the highest density (Figure 5.7b). A natural method for measuring angular correlations $g^{(2)}(\phi, \tau = 0)$ between photons separated by the angle ϕ around the annulus would be to use two fibers at different positions; our Floquet scheme enables an equivalent measurement using a single fiber, whilst inducing a mode-dependent phase shift between polaritons and photons that we compensate with linear optics before the fiber.

Although the average density of our pairs exhibits no angular structure, we find that two photons rarely occupy the same location (Figure 5.7c). The spatial correlations in the Laughlin state should take the form $g^{(2)}_{\mathrm{L}}(\phi) \propto |\psi_{\mathrm{L}}(z_2 = e^{i\phi} z_1)|^2 \propto \sin^4(3\phi/2)$, which oscillates with the angle ϕ between the photons with a periodicity of 120° because only every third angular momentum state is accessible. Motivated by this expected form, we fit the observed correlations with $g^{(2)}_{\mathrm{fit}}(\phi) = g_0 + g_1 \sin^4(3\phi/2)$ allowing for an offset g_0 from perfect spatial anti-bunching and a reduction of the oscillation amplitude g_1 due to imperfect state fidelity or detection. The fit yields a small offset $g_0 = 0.11(19)$ and an oscillation amplitude $g_1 = 0.77(36)$ with a significance of 2.1 standard deviations corresponding to a probability of 0.02 to arise from statistical fluctuations in a system with no dependence of correlation on angle. Additional data taken without phase compensation further reduces this probability to 10^{-5}.

In sum: the detected pair-populations in angular momentum space suggest Laughlin physics, but are insensitive to the phase and even the purity of the superposition between $|39\rangle$ and $|66\rangle$. The observed spatial anti-correlation, on the other hand, only occurs for a coherent superposition with a minus sign. Combined, these data indicate that the photon pairs, in a virtual image plane at the twisted cavity mode waist, have 76(18)% overlap with a pure Laughlin state. This fidelity is limited primarily by our conservative assumptions about the unmeasured momentum-non-conserving pair populations.

This work establishes quantum many-body optics in strongly interacting gases of topo-

logical polaritons as a critical route to breakthroughs in quantum materials. We bring to bear the unique microscopic control of our photonic platform, providing highly tunable system parameters, energy- and space- resolved particle injection, and the ability to measure correlations in almost any basis using simple linear optics. The present performance, combined with a cavity that can be made precisely degenerate in lieu of the Floquet scheme should directly support polaritonic Laughlin states. Looking ahead, novel state-preparation schemes [100, 101] such as dissipative stabilization [102, 103, 104, 105, 106] will enable the formation of larger topologically ordered states. Interestingly, the Laughlin state that we have assembled in this work already contains a quasi-hole at its center, a precursor to directly measuring statistical phases of anyons [107, 108, 109, 110, 111] or even non-Abelian braiding in the Moore-Read state [112].

5.3 Understanding and improving cavity performance

The contents of the previous section described the creation of a 2-particle Laughlin state made of light using Rydberg polaritons and a twisted optical cavity. However, the maximum size of such a quantum material scales with the number of degenerate modes of the cavity. Thus, this section describe our efforts to create a highly degenerate multimode twisted cavity compatible with the Rydberg gas, enabling us to explore bigger and more robust topologically-ordered Laughlin states with multiple polaritons.

5.3.1 Optical aberrations

Optical resonators have become an indispensable tool in optical and atomic physics. They are typically understood and utilized in the paraxial, quadratic limit, where the transverse mode structure and spectrum are derived [28]. For common cavities, this results in the familiar Hermite-Gauss (HG) or Laguerre-Gauss (LG) families of eigenmodes, whose evenly-spaced resonance frequencies are set by the Gouy phase. Usually this description is entirely

adequate, as deviations from this approximation are typically small when the resonator mode waist w is much larger than the wavelength λ. Additionally, most applications use only the fundamental resonator mode.

As degenerate cavities have become more prevalent in quantum science experiments [113, 79, 69, 114, 115], the atomic physics community has begun to probe the limits of the aforementioned approximations by pursuing high-finesse, small waist resonators for their enhanced light-matter coupling [116, 117, 118]. Degenerate cavities in particular are alarmingly sensitive to small deviations from the uniformly-spaced energy spectrum of the quadratic approximation. For the n^{th} degenerate mode to overlap within a resonator linewidth, the spacing must be uniform to about one part in n times the finesse. Optical resonators often have finesses in the range of 10^3 to 10^5, so achieving degeneracy requires extreme uniformity of the spectrum.

A number of attempts have been made to predict resonator spectra beyond the paraxial, quadratic limit. One might anticipate that finite-element or boundary-element approaches would provide quantitatively accurate results, but the fact that the resonators are many thousands of λ across makes discretization a substantial computational challenge. Instead, the authors of Reference [119] make closed-form predictions for mode energies by expanding the mode functions of two mirror resonators in spheroidal coordinates. References [120, 121] take a different approach, computing order-of-magnitude estimates of the impact of perturbations to the the paraxial resonator modes. Reference [122] analyzed nonparaxial eigenmodes of a half-symmetric two-mirror cavity using a perturbative expansion in a basis of HG modes.

The work of Reference [47] pursues a more general treatment of aberrations using a novel perturbative expansion of the round-trip propagation operator in the basis of the paraxial quadratic eigenmodes, and finds that this perturbative approach accurately captures observed mode-mixing [79, 115] arising from aberration terms near degeneracy. This sub-

section will briefly review several main results of this work and place them in the context of twisted cavity development for the purpose of creating topologically ordered quantum materials made of light.

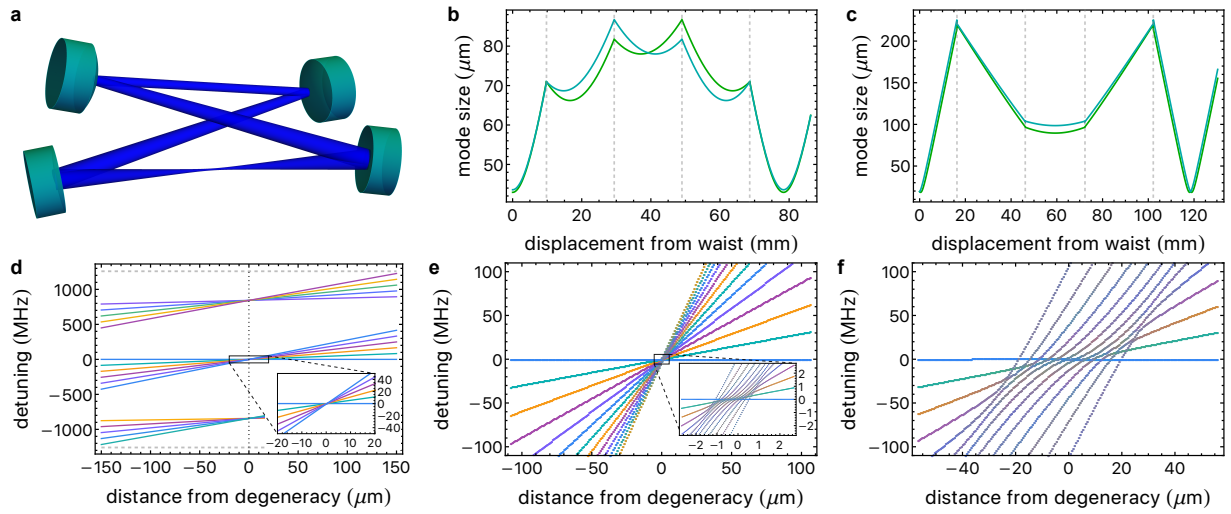

Figure 5.8: **Aberrations in past Simon Lab cavities.** Two non-planar cavities are described: the cavity from Reference [79] (the Landau cavity) and the Original Twister [44]. **a,** Non-planar cavity geometry. The Original Twister is shown, but the Landau cavity is nearly identical. **b** and **c,** Mode size over a cavity round trip for the Landau cavity and the Original Twister, respectively, for $\lambda = 780$ nm. Mirror positions are indicated by the dashed vertical lines. Colors indicate the two semi-axes. Small discontinuities are due to a change of semi-axis basis arising from the astigmatism plus rotation after reflection into a new plane. **d,** Paraxially-expected spectrum, with target degeneracy inset. **e** and **f,** Aberrated theory spectra for the Landau cavity and the Original Twister, respectively. Each point's color is a blend of the color scheme in **d**, with weightings given by the paraxial eigenmode contributions to the point's corresponding eigenvector. Level repulsion and mode mixing due to cubic astigmatism can be seen, which is much stronger in the Original Twister. Figure taken from [47].

To demonstrate the utility of this perturbative approach to understanding aberrations, Reference [47] calculates the aberrations of a resonator whose degeneracy is broken, at lowest order, by cubic astigmatism. The cavity from [79] (the Landau cavity) and the Original Twister were specifically designed to suppress the impact of *quadratic* astigmatism [79, 114]. In each case, the Landau level is formed by a set of degenerate orbital angular momentum (OAM) modes. The first of the two cavities, with a larger waist, exhibited no observable

avoided crossing near degeneracy [79]; the second, with a $\sim 2\times$ reduced mode waist size, presented clear avoided crossings as degeneracy was approached [44]. In short, these cavities provide a clear and simple testbed for beyond-quadratic resonator aberrations.

The cavities in question use a non-planar twist to generate a synthetic magnetic field for light [79, 123, 114]. The non-planar twist necessitated off-axis incidence on curved mirrors, and thus exhibited quadratic astigmatism that couples every *second* OAM mode due to the different effective radii of curvature for the sagittal and tangential axes [124]. To avoid this destabilization due to quadratic astigmatism, in Reference [79], it was found that by ensuring that the twist generated a Gouy phase of $2\pi/3$, a conical Landau level could be realized, consisting of only every third OAM mode $l = 0, 3, 6, ...$, thereby suppressing the impact of quadratic astigmatism. Unfortunately, this simply pushed the problem to slightly higher order: Non-normal incidence on a spherical surface *also* introduces cubic astigmatism.

The basic resonator configuration is shown in Figure 5.8a. Four mirrors are arranged in a tetrahedral configuration, providing the non-planarity. The Original Twister was designed for a smaller waist (to allow for Rydberg-mediated interactions between the photons) relative to the Landau cavity, which dramatically increases the effect of aberrations.

The expected spectrum calculated under the paraxial, quadratic assumptions is shown in Figure 5.8d. Only the modes of interest, angular momentum modes with Laguerre-Gauss indices $(\ell, p) = (\ell, 0)$ are shown. As the Gouy phase varies with mirror spacing, a degeneracy is approached when the mirror spacing sets the total round trip Gouy phase to be $\frac{2\pi}{3}$. The expanded inset in Figure 5.8d shows the expected degeneracy of angular momentum modes $\ell = 0, 3, 6, ...$

Figures 5.8e,f shows the calculated perturbed spectra of Landau cavity and the Original Twister, respectively. The cubic aberration is evident as the level repulsion around the expected degeneracy. Incomplete level repulsion of the highest-order modes shown is a finite basis effect (edge basis states do not have higher levels to couple to). In reality, high-order

modes also see increasing loss, as larger modes run off the edge of the mirror, or encounter mirror imperfections within their larger surface area. For strong mixing, even "low-order" modes become lossy, as they acquire a significant contribution of high-order unperturbed modes. In fact, this mixing was strong enough to destabilize even the lowest-order mode in the Original Twister as degeneracy was reached.

Apparently, the modest reduction in waist size in the Original Twister comes with a dramatic increase in the cubic aberration. This can also be seen in the round trip mode-size plots (Figures 5.8a,b) as the extra "work" done by each curved mirror surface in the aberrated geometry. The zoomed inset of Figure 5.8e shows a similar level structure to that of Figure 5.8f, though with much weaker mixing. Throughout Figure 5.8, we include only the cubic perturbation (i.e., we ignore quartic and higher non-paraxial propagation and spherical aberration terms). Our perturbative approach is limited by commutator ambiguities [125] when combining terms of different orders, but we can ignore higher-order terms for these cavities, which are dominated by resonant cubic terms.

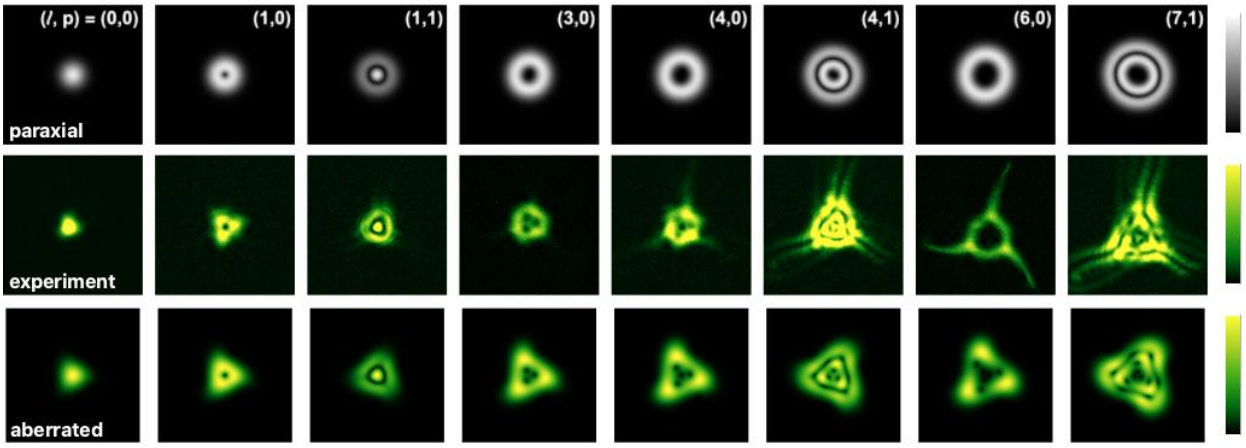

Figure 5.9: **Aberrated mode profiles.** Mode profiles are shown for the Landau cavity near the degeneracy point shown in Figure 5.8d. Profiles are shown for (**top row**) paraxial expectation (near-Laguerre-Gauss modes, with mode indices indicated), (**middle row**) experimentally measured profiles, and (**bottom row**) aberrated calculation. Color bars at right scale between zero and peak intensity of each image. Figure taken from [47].

Our calculation method enables construction of the mode profiles (eigenvectors), in addition to the mode energies (eigenvalues) from U_{rt}. For example, the mixed-modes of Landau cavity near the degeneracy point in Figure 5.8d are shown in Figure 5.9. The resonant cubic astigmatism leads to a clear three-fold symmetry, as modes separated by 3 OAM quanta are coupled by cubic terms.

While the resemblance between the various modes in Figure 5.9 is clear, the experimental modes show a more dramatic deviation from the paraxial expectation than even the aberrated predictions. This could be due to further effects, such as (a) mixing that is strong enough to be non-perturbative, (b) interaction between cubic terms and higher-order terms (e.g., resonant 6th-order astigmatism [as indicated by the six-fold symmetry in some modes], non-paraxial propagation, spherical aberration), or (c) mode-dependent loss. High-order modes are clearly involved, as seen by the long tails extending out to large radii in the last few columns of Figure 5.9.

Motivated by the goal of achieving a large-scale degeneracy of photonic modes to build topologically ordered quantum materials, Reference [47] proposes and builds a twisted cavity consisting of flat mirrors and two intracavity lenses. Flat mirrors allow for the non-planar twist without introducing astigmatism via non-normal incidence, while the on-axis intracavity lenses provide the transverse confinement necessary for a stable cavity. This arrangement enables a non-astigmatic cavity without relying on hard-to-manufacture elliptical or off-axis parabolic mirrors.

Spectra at a range of lens splittings near degeneracy points can be seen in Figure 5.10. Figure 5.10a shows $s = 1$ (involving every mode), Figure 5.10b shows $s = 3$ (involving every third mode), and Figure 5.10c shows $s = 3$ for lenses oriented backwards. This backwards configuration significantly worsens the observed aberrations, in agreement with our theory. Importantly, this effect does *not* appear when modeling the lens as a position-dependent phase plate (as in References [122, 120, 121], with mirrors). The slope-dependent

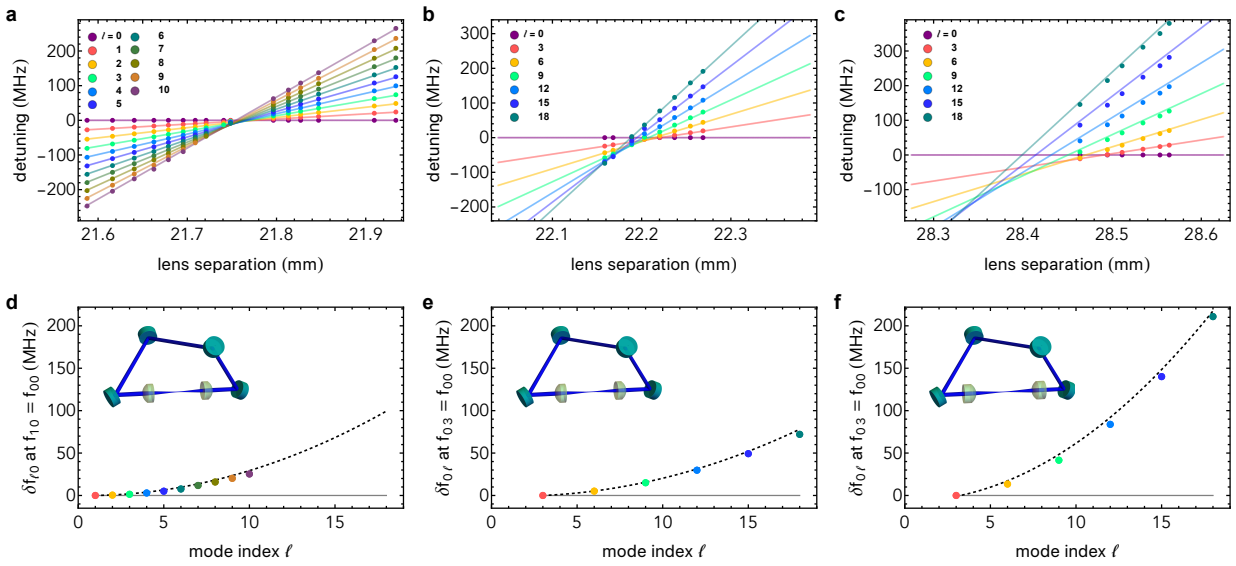

Figure 5.10: **Measured spectra of the twisted lens cavity. a,** near the $s = 1$ point. **b,** near the $s = 3$ point. **c,** near the $s = 3$ point with backwards lenses. **a-c** have the same vertical and horizontal spans. Data positions along the horizontal axis are inferred from the splitting between the fundamental mode and the lowest-excited mode in the degenerate manifold. Markers indicate measured data points, while the lines indicate the perturbative prediction with no free parameters. **d-f,** Missed-degeneracy due to aberrations for the $s = 1$, $s = 3$ point, and $s = 3$ point with backwards lenses, respectively. Mode energies relative to the fundamental mode are plotted against angular momentum ℓ at the lens separation where the fundamental and $\ell = s$ modes are degenerate. Without aberrations, these modes would all be degenerate at the same lens separation, so this quantity would be zero (solid line). Data is shown in colored points, obtained by linear fits to the data of **a-c**. Our perturbative calculation, with no free parameters, is shown by the dashed line (shown as continuous, for ease of comparison to the data). **d-f** have the same vertical and horizontal spans. Note that the aberration contribution to the spectrum is $\propto \ell^2$, as expected for a quartic perturbation. Figure taken from [47].

perturbation terms must be included to accurately reproduce the spectra.

Remarkably, the $s = 1$ point supports stable modes. From a purely paraxial standpoint, this cavity should be unstable: the ABCD matrix is singular, akin to an exactly-confocal cavity [124]. Quadratic astigmatism resonantly couples modes in this configuration, so the cavity lenses must be aligned very precisely. Curved lens surfaces must be centered / un-tilted with respect to the cavity axis to within $\delta x \lesssim 10\,\mu$m (and/or equivalent tilt $\sim \frac{\delta x}{R} \approx 0.1°$; in practice the positioning is a more stringent constraint). Without this level of alignment,

quadratic astigmatism mixes the modes near degeneracy, leading to level repulsion (as seen in, e.g., Figure 5.8 for the cubic case). A quartic term breaks this degeneracy, confining the light to within a finite radius of the cavity axis in the presence of small but finite misalignment.

The $s = 3$ point enjoys protection against quadratic astigmatism (it is off-resonant), and is thus significantly less sensitive to alignment. However, only 1/3 of the number of modes lie within a given frequency window, as compared to $s = 1$. Eventually the quartic term breaks this degeneracy, leaving only a few modes within several MHz in the "degenerate" manifold.

Flipping the lenses such that the curved side faces the cavity waist worsens the aberrations, increasing their effect on the spectrum. This can be seen from the wider spread in zero-crossings of the modes in Figure 5.10c compared to Figure 5.10b, as well as the stronger quadratic contribution to mode energies in Figure 5.10f than in Figure 5.10e. Due to technical aspects of our alignment procedure, the backwards lens-cavity was more ambiguous to align. And while the quadratic astigmatism of misaligned lenses does not affect the stability of the $s = 3$ manifold, it can affect the size of the splittings. For the model in Figure 5.10f, we have included a single lens tilt of 2.5°. In reality, both lenses could be tilted / displaced in an arbitrary transverse direction. This would be difficult and not so informative to disambiguate.

In conclusion, the perturbative approach presented in Reference [47] quantitatively predicts the spectra of aberrated optical cavities and proposes a twisted lens cavity to minimize such aberrations. While the Original Twister did not achieve a large-scale degeneracy of photonic modes, Lluna—our next-generation twisted lens cavity mentioned in Chapter 4—shows promise for increasing the number of degenerate cavity modes, enabling us to create few-body Laughlin states made of light.

5.3.2 Backscatter suppression

High-finesse optical cavities are broadly useful across quantum optics, enabling efficient interfaces of individual photons to quantum emitters such as atoms and ions [126], quantum dots [127, 128], rare-earth ions [129, 130], and defect centers [131, 132]. Intracavity optics, such as lenses or modulators, can radically expand the capabilities of such optical resonators. While refractive elements are used extensively in free space optics, they have thus far remained largely absent from moderate- to high- finesse optical cavities. Concerns about backscatter and loss have typically been presumed to preclude intracavity changes of refractive index, even if anti-reflection (AR) coatings are employed. If these concerns could be addressed, intracavity optics would be transformative, enabling new capabilities for light-matter interaction.

Backscattering has been studied across the electromagnetic spectrum, from microwave to optical frequencies. It is of practical importance for applications in ring lasers [133, 134] and gyroscopes [135, 136], and is fundamentally connected to topological systems [137]. In particular, backscatter immunity is a defining characteristic of topologically protected edge channels, even in the presence of disorder [138, 139, 77, 140]. Elimination of undesired optical backreflections, however, has so far been limited to active [141] or passive [142] cancellation.

The work of Reference [48] presents a quantitative and experimental assessment of backreflections in cavities. This subsection will briefly review several main results of this work and place them in the context of backreflection suppression in our current twisted cavity, Lluna (as presented in Chapter 4). Reference [48] identifies three main sectors contributing the the total amount of backreflection: polarization, mode envelope and transverse mode profile—each of which can be optimized to suppress backreflections. These approaches amount to either suppression of the back-coupling matrix element or reduction of the available density of states for backscattering. Backscattering can be suppressed nearly one million-fold in a twisted optical cavity, allowing for effective reflectivities below 1 part per billion (ppb).

Engineering the polarization eigenstates of the cavity is the essential tool for achieving this performance. Additionally, beams carrying orbital angular momentum (OAM) exhibit even stronger suppression of backreflections due to a topological protection arising from their phase winding.

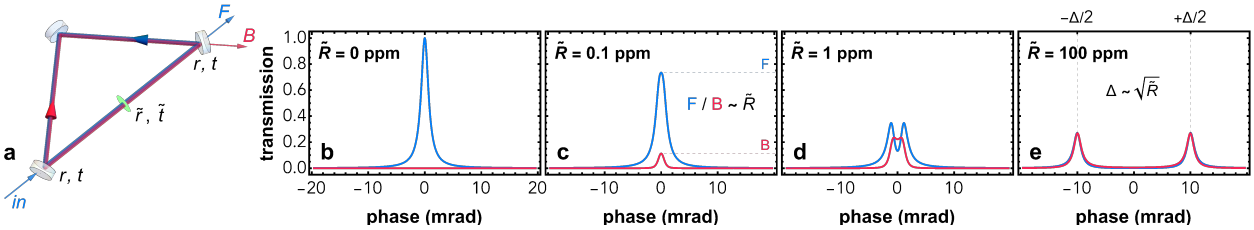

Figure 5.11: **Model of intracavity backscattering. a,** We consider a planar running wave cavity with a single intracavity reflector. Input and output mirrors have amplitude reflection (transmission) coefficient r (t). The third mirror is a perfect reflector. The intracavity reflector (green) has amplitude reflection (transmission) coefficient $\tilde{r}$ ($\tilde{t}$). Output paths of the forward- and backward- modes from the input mirror are omitted. **b-e.** Cavity transmission for different values of $\tilde{R} = |\tilde{r}|^2$. For $\tilde{R} = 0$, we see the expected Lorentzian lineshape. The cavity finesse has been set to 4000 via r and t with no loss. The blue (red) curve shows the forward-traveling mode F (backward-traveling mode B) transmission. As $\tilde{R}$ increases, we see coupling of the injected forward-traveling light into the backward-traveling mode. For sufficiently small $\tilde{R}$, the forward and backward responses are both approximately Lorentzian with peak ratio $\propto \tilde{R}$. For larger $\tilde{R}$, the forward and backward modes hybridize, splitting into two spectrally-separated peaks with near-equal participation of both F and B. The splitting of these peaks Δ is $\propto \sqrt{\tilde{R}} = |\tilde{r}|$, and is directly analogous to the classical coupling of two harmonic oscillators. The analysis in this figure assumes perfect mode- and impedance-matching of the coupling between the forward and backward modes. Figure taken from [48].

To begin, Reference [48] considers a running wave optical cavity consisting of three mirrors as shown in Figure 5.11a. The two input/output mirrors have amplitude reflection (transmission) coefficients r (t), while the third mirror is a perfect reflector. An intracavity reflector with amplitude reflection (transmission) coefficient $\tilde{r}$ ($\tilde{t}$) can couple a forward-traveling mode to a backward-traveling mode. Indeed, even in cavities without an explicit reflector, the mirror imperfections in high-finesse ring cavities can be sufficient to induce detrimental backscattering [141].

Using standard input/output field relations [124], the intracavity and output fields for

both the forward- and backward-traveling modes may be computed, as shown in Figures 5.11(b-e) for various values of $\tilde{R} = |\tilde{r}|^2$. As the intracavity reflectivity $\tilde{R}$ increases, the forward and backward modes hybridize until they are fully mixed. Note that the highest reflectivity shown, $\tilde{R} = 100$ parts per million (ppm), corresponds approximately to the best (lowest-reflectivity) commercially-available AR coatings. Thus, even at the modest finesse of 4000 shown in Figures 5.11(b-e), any optic within the cavity would fully hybridize the forward and backward modes. Note that unlike the case of a standing wave cavity [143], sub-wavelength changes of the single reflector's longitudinal position do not impact the amount of backreflection for the running wave case.

Note that, in general, coupled modes *split*. Examples of this concept are vacuum Rabi splitting (VRS), coupled cavities, and photonic modes coupled via an intracavity reflector as in Figure 5.11. The suppression of backscattering, and thereby the coupling, should thus manifest as a reduction in the observed mode splitting.

A powerful tool to break the forward-backward symmetry is a non-planar cavity geometry, which provides a round-trip image/polarization rotation [144, 145] (an example of a Pancharatnam-Berry phase [146, 147]). Combined with the Faraday effect, this rotation allows introduction of loss for one polarization state via Brewster reflection and thus unidirectional lasing of an active gain medium within such a cavity [148, 149]. For a resonator without gain, this approach fails, making both modes lossy for a large enough coupling between them. Our approach is to instead make the reflection-induced coupling between forward and backward modes vanishingly small, achieved by ensuring that the backward-propagating mode at the same energy has at least the opposite polarization, and potentially also the opposite angular momentum. Traversing a non-planar cavity in the opposite direction reverses the image rotation, breaking inversion symmetry of the system and thus making it helical: the two polarization states of the cavity are split out in frequency, while forward- and backward-traveling modes of the same helicity remain degenerate [150].

The total effect of backscattering can be described as a product of matrix elements in three sectors: (i) polarization; (ii) mode envelope; and (iii) transverse mode profile. We find that sectors (i) and (iii) benefit from non-planarity.

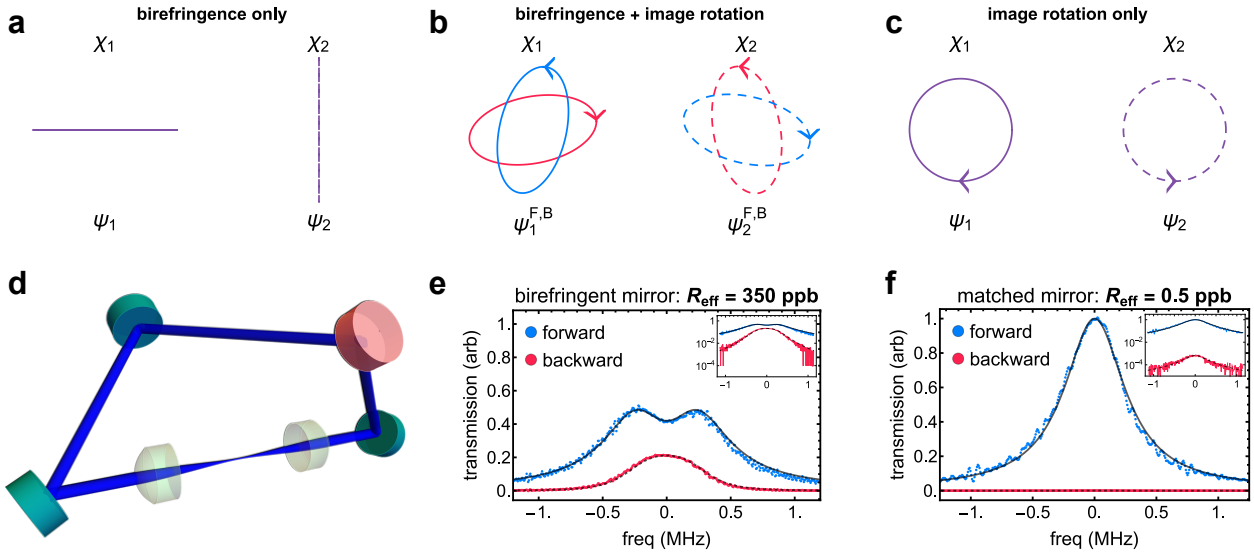

Figure 5.12: **Polarization suppression of backscattering.** Cavity polarization eigenstates labeled by their eigenvalues χ_i and eigenvectors ψ_i are shown in (**a-c**). **a.** A cavity with only birefringence has linearly polarized eigenstates (along the birefringent axes). **c.** A non-planar cavity with image rotation has circularly polarized eigenstates. **b.** In a cavity with both image rotation and birefringence, the modes are in general elliptically polarized. The forward (blue) and backward (red) polarization modes are shown for each eigenvalue χ_i, though they overlap exactly in **a** and **c**. **d.** Cavity arrangement. The pink mirror is switched between a birefringent mirror and a non-birefringent mirror; see main text for details. Measured cavity transmission for the forward (blue) and backward (red) modes are shown in **e** birefringent and **f** non-birefringent configurations. Simultaneous fits (black) to the forward and backward data extract the effective reflectivity R_{eff}. The same data is shown on a logarithmic scale in the insets. Much lower excitation of the backward mode is evident in the birefringence-canceled case. Figure taken from [48].

For the case of birefringent phase shifts arising from non-normal incidence on dielectrics in a planar resonator (Figure 5.12a), the forward and backward matrices are the same. The resulting polarization eigenstates are linear, oriented along the birefringence axes.

For the case of an image rotation only (Figure 5.12c), the backwards-traveling mode image-rotates in the opposite direction. But, the z-direction inverts as well, so the forward and backward matrices are again the same. The resulting eigen-polarizations are circular.

However, these matrices are associated with two different eigenvalues, and thus for circular polarization states in a twisted cavity, *backreflections are energetically forbidden.* Intuitively, this can be seen from the polarization frequency splitting arising from the circular polarization vector rotating either with or against the image rotation. When a reflection occurs, the image rotation changes sign, but the polarization rotation (i.e., spin angular momentum, not helicity) does not.

To summarize, backreflection of linear polarization states is allowed: light resonant in the forward direction is also resonant in the backward direction. Circularly polarized eigenmodes of a twisted cavity, however, are protected against backreflections. Light of a given polarization mode finds no density of states to backscatter into. In the general case of both birefringence and rotations, the cavity polarization modes are elliptical (Figure 5.12b).

Reference [48] discusses the measurement of backreflections in a cavity whose schematic is shown in Figure 5.12d. We employ a non-planar cavity with two intracavity plano-convex lenses that act as reflectors. The lenses are super-polished for low surface roughness (< 2 Å rms) and are AR-coated to $R_{\mathrm{AR}} \approx 250$ ppm at 780 nm (as measured by the manufacturer). All measurements reported in this work use a wavelength of 780 nm. The lower input/output mirrors are designed for zero birefringent phase shift between s and p polarization at their 28° angle of incidence (AOI). Minimizing this phase difference δ_{sp} is critical; we found that a coating with $\delta_{sp} = 0 \pm 1°$ specification performed notably better than a different coating with $\delta_{sp} = 0 \pm 3°$. The upper mirrors have a spatial rotation of 89° between their respective s and p axes. Thus, if these two mirrors have the same coating, any residual birefringence nearly cancels after reflection off both mirrors, as s-polarization for the first mirror very nearly becomes p-polarization for the second mirror. We can vary the birefringence by using two upper mirrors from the same coating run (thus canceling birefringence), or by using mirrors from different coating runs, leaving a residual birefringent phase shift. The finesse of this cavity is $\mathcal{F} \approx 3900$, set primarily by the input/output mirror

transmission. This geometry gives a waist of 18 μm between the lenses, whose planar surfaces are separated by about 22 mm.

The results for backreflections of the fundamental cavity mode are shown in Figure 5.12. For the birefringent case (Figure 5.12e), the forward mode begins to hybridize with the backward mode. Even in this case, the effective reflectivity ($R_{\text{eff}}^{\text{biref}} = 350$ ppb) is about 700 times lower than the bare reflectivity of the AR-coated lens ($R_{\text{AR}} = 250$ ppm). Furthermore, the above analysis assumes a single reflector, while in reality, this cavity has reflections at 4 lens surfaces. This $> 700\times$ reduction in reflectivity from the free-space value primarily results from the round-trip image rotation still dominating over the un-canceled birefringence, meaning that the resulting polarization states are still nearly circular. From the measured birefringence of the mirrors, we only expect the magnitude squared of the matrix element $|\alpha_{\text{pol}}|^2 \sim 6\%$ overlap between the forward and backward cavity polarization modes with the same eigenvalue. There is also another mechanism of backreflection suppression at work related to the spatial mode profile of the cavity mode.

For the non-birefringent case, we use mirrors designed for $\delta_{sp} = 0 \pm 10^\circ$ at the 45° AOI of the upper mirrors. Since both upper mirrors come from the same coating run in this case, the 89° spatial rotation between these mirrors cancels much of any residual birefringence of this coating. As shown in Figure 5.12f, we see a *further* 700-fold reduction in backreflections, plunging the effective reflectivity below 1 ppb. This is almost 1 million times lower reflectivity than the best-achievable AR-coatings in free space, and results in a negligibly-perturbed forward-propagating mode. Despite having four changes of refractive index per cavity round trip, the cavity polarization state is sufficiently circular that backreflections are almost entirely forbidden.

In addition to the polarization sector, the spatial mode profile matrix element between the initial and target state must be nonzero to allow backreflection to occur.

Consider how the cavity mode profiles transform under a reflection for LG modes. The

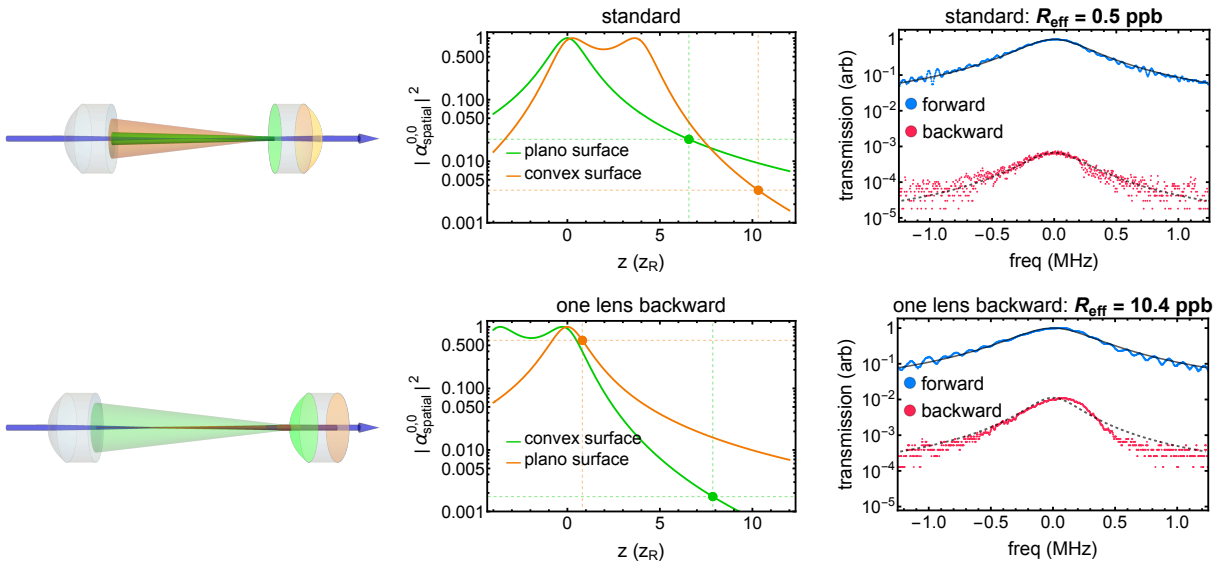

Figure 5.13: **Spatial mode-matching suppression of backscattering.** Standard (backward) orientation of the rightmost lens is shown in the top (bottom) row. Left column: lenses are shown, along with the cavity mode (blue; propagating left-to-right) and backreflected beam profiles from the first and second surfaces (green and orange, respectively) of the rightmost lens, in order of incidence. We ignore here reflections from the leftmost lens. The lenses have an outer diameter of 7.75 mm, with clear aperture $\geq 75\%$. The tubes indicating the mode size have radius equal to 1.92 times the local beam waist; that is, 99.94% of the beam's power is contained within the tube, and losing all power outside of this tube would limit the finesse to 10^4. Note that the reflection off of the second surface of the backwards lens is best mode-matched to the backward-traveling fundamental mode. Middle column: The matrix elements of reflection in the spatial profile sector between forward- and backward-traveling modes are plotted for the lens surfaces, showing the spatial overlap integral vs. position parameterization for each reflecting surface. The reflecting surfaces in our cavities are indicated by the points along the curves. Note that the backwards-orientation plano surface has substantially higher $|\alpha^{0,0}_{\text{spatial}}|$ than any of the other surfaces. Right column: Experimental backreflection data. Due to the improved mode matching, the effective reflectivity coefficient R_{eff} in the backwards-lens case is about $20\times$ greater than in the standard configuration (top right is the same data as in Figure 5.12f). The standard configuration is thus more favorable for reducing backscatter. Figure taken from [48].

radial coordinate r remains unchanged, while $\phi \to -\phi$. Since the sign of ℓ only matters in the phase winding term, the reflection thus has the effect of taking $\ell \to -\ell$. That is, the forward-propagating mode with angular momentum ℓ has the same phase profile as the backward-propagating mode with angular momentum $-\ell$. Furthermore, the backward-propagating mode at a given plane has the opposite sign wavefront curvature R as the

forward-propagating mode: if the forward mode has a diverging wavefront at a given plane, the backward mode is converging.

A reflection should be well-mode-matched into the backwards traveling mode in order to occur. This is visualized in the left column of Figure 5.13. This mode-matching can be increased by turning one lens to be backwards, such that the cavity mode encounters the lens' flat surface when it is large and less-divergent. This gives better mode-matching of the reflection into the backward mode, and thus a 20× increase in the effective reflectivity R_{eff} (right column of Figure 5.13).

For the standard lens orientation, we see from Figure 5.13 that the magnitude squared of the matrix element $|\alpha_{\text{spatial}}|^2 \sim 0.02$, which provides a factor of 50 suppression of backreflections compared to the free space value. This factor of 50 due to mode mismatch accounts for the rest of the $\sim 700\times$ reduction of the free space reflectivity R_{AR} to the birefringent value $R_{\text{eff}}^{\text{biref}}$ in Fig. 5.12f.

Additionally, LG modes with nonzero angular momentum cannot backreflect into themselves. To experimentally probe this, we increase cavity backreflections by using the birefringent mirror configuration of Figure 5.12e, and reversing the orientation of one of the lenses (Figure 5.13, bottom row). Using holographic beam-shaping with a digital micromirror device [151], we inject a desired LG ring mode (i.e., $p = 0$) into the cavity and observe its backreflection behavior. While $\ell = 0$ shows substantial backscatter, we see backreflection suppression by one to four orders of magnitude for nonzero angular momentum. In fact, by observing both the forward and backward modes on CCD cameras, we find that this backreflection suppression is limited entirely by the availability of other modes to backscatter into.

In the lowest backreflection configuration (non-birefringent, standard lens orientation as in Figure 5.12f), backreflections of higher-angular momentum states are unobservably small. The suppression quantified for $\ell > 0$ modes in the higher-backreflection configuration

(birefringent, one lens backward) indicates that beams carrying orbital angular momentum experience effective reflectivities in the lowest backreflection configuration as low as sub-part-per-*trillion*.

In conclusion, Reference [48] demonstrated the ability to incorporate optics inside of high-finesse optical cavities. Lenses and modulators could dramatically expand the capabilities of such resonators, as they do for free space optics. By engineering the polarization properties of the cavity eigenmodes, we suppress the effect of intracavity backreflections by six orders of magnitude, resulting in sub-part-per-billion effective reflectivities. Beams carrying orbital angular momentum provide even greater suppression due to their phase winding, limited only by the available density of states for mode conversion, and yielding effective reflectivities at the part-per-trillion level. We have explored the effects on backreflection of both polarization and spatial mode profile in these non-planar cavities. In general, harnessing this backreflection suppression yields a more robust degenerate manifold of photonic states in our most recent optical cavity, Lluna, for the purpose of creating photonic Laughlin states.

CHAPTER 6

PHOTONIC MODE CONVERSION

This chapter is based off of reference [152]:

Optical mode conversion via spatiotemporally modulated atomic susceptibility.
C. Baum, M. Jaffe, L. Palm, A. Kumar, and J. Simon, *arXiv preprint*, (2022).

6.1 Motivation

Efficient control over photonic degrees of freedom, including frequency, polarization, and spatial mode, has widespread applications in information and communication. Put simply: the more degrees of freedom one can manipulate, the more information one can encode in a single channel of light. This idea is utilized regularly in both classical and quantum communication, where light has been multiplexed in arrival time [153, 154, 155], frequency [156, 153, 154, 155], polarization [155], quadrature [155], and most recently space [157, 155, 158, 159, 160, 161, 162, 161, 163, 164] to substantially increase information transfer over a fiber [165, 166, 167] and free-space link [168]. Spatial information may be conveniently encoded within families of propagation eigenmodes; the Hermite-Gaussian (HG) and Laguerre-Gaussian (LG) families are appealing for their orthogonality and infinite-dimensionality, supporting the exploration of higher-dimensional Hilbert spaces for quantum computing [169, 170], formation of orbital angular momentum qudits [170, 171, 172, 159, 173, 174, 175], improved quantum key distribution [171, 176, 159, 175, 177, 178, 179], lower-crosstalk quantum communication [180, 181, 177], and distribution of quantum information to multiple users in a quantum network [173].

High-dimensional optical information encoding requires the ability to *manipulate* the various photonic degrees of freedom through "mode conversion" [182, 183, 184, 185, 186, 187, 188, 189, 190, 191, 164]. Frequency and polarization mode conversion can be achieved

quite flexibly at near-unit efficiency using electro-optic modulators [192] and waveplates. However, efficient spatial mode conversion is more challenging. In general, spatial mode conversion requires a spatially-dependent phase and amplitude modification of a photon's electric field. While phase can be modified losslessly by a phase-imprinting device, amplitude modification occurs only through propagation or discarding amplitude via a physical barrier, limiting the efficiency with which spatial mode conversion can occur. For instance, devices such as spatial light modulators, digital micromirror devices, vortex plates, and liquid crystal q-plates [193, 194, 195, 196, 197] are excellent devices for generating modes with orbital angular momentum (OAM) by imprinting incident light with a spiral phase. While the resulting mode has the correct phase winding to be purely LG, its amplitude distribution does not. Rather, the resulting mode can be expressed as an expansion of the LG radial modes for a given OAM, illustrating that a phase imprint alone is insufficient for highly efficient spatial mode conversion to a *single* LG mode [198, 177]. Thus, mode-converting devices have been designed to modify light in environments such as waveguides, cavities, and photonic crystals that limit the occupiable spatial modes to enhance conversion to a single target mode. Among these devices are a HG$\leftrightarrow$LG mode converter using an astigmatic microcavity [199], an arbitrary HG mode-order converter utilizing the impedance mismatches between coupled Fabry-Pérot resonators [200], design-by-specification converters based on computational methods [201], and an assortment of silicon photonic converters that harness refractive index variation to smoothly modify a propagating spatial mode [202, 203, 204, 205, 206, 207, 208, 209, 210, 211, 212, 213, 214].

In this chapter, we explore a new method in which spatial and frequency mode conversion occur simultaneously in a single system with high efficiency. In effect, we create a rapidly sculptable, rotating optic inside of an optical cavity that converts photons between cavity modes. In practice, we modulate [46], in both space and time, the optical susceptibility of a stationary atomic sample at the waist of a twisted optical cavity using a strong auxiliary

beam, inducing a coupling between cavity modes. This auxiliary beam Stark shifts the energy levels of the atomic sample to create a spatiotemporally-varying optical susceptibility across the atomic sample akin to a rotating optic. Photons that are incident on the atomic sample accrue a position-dependent phase that couples the incident mode to other modes of the cavity, which enables repeated light-atom interactions and preferentially enhances the emission of light into supported, resonant spatial modes. We measure the efficiency of this conversion process for increasing atom number and modulation beam intensity. We find a parameter regime in which the internal conversion efficiency saturates near unity.

6.2 Experimental methods

We demonstrate conversion between LG modes of orbital angular momenta $l = 3 \rightarrow l = 0$ (i.e. $\mathrm{LG}_{30} \rightarrow \mathrm{LG}_{00}$). Our optical cavity is a four-mirror twisted cavity, meaning one mirror lies outside of the plane formed by the remaining three [215]. As the eigenmodes of this cavity are non-degenerate LG modes, cavity photons require a change in both their spatial and frequency degrees of freedom to undergo mode conversion. This change can be accomplished by passage through the an atomic sample whose optical susceptibility varies in time and space. Provided the variation occurs at the frequency difference between $l = 0$ and $l = 3$ and imprints a phase on $l = 0(3)$ such that the resulting spatial mode has non-zero overlap with $l = 3(0)$, a coupling will be engineered between the $l = 0$ and $l = 3$ cavity modes.

Fig. 6.1a illustrates our mode conversion scheme. A ^{87}Rb atomic sample resides at the waist of our twisted optical cavity, which hosts modes at 780 nm (near the $5\mathrm{S}_{1/2} \leftrightarrow 5\mathrm{P}_{3/2}$ transition of ^{87}Rb) and at 1529 nm (near the $5\mathrm{P}_{3/2} \leftrightarrow 4\mathrm{D}_{5/2}$ transition of ^{87}Rb). The $5\mathrm{P}_{3/2} \leftrightarrow 4\mathrm{D}_{5/2}$ transition of the atomic sample is energetically modulated by a time-varying, spatially-dependent optical Stark shift generated by an auxiliary 'modulation' beam at 1529 nm whose intensity distribution is illustrated in Fig. 6.1b. This pattern is achieved by overlapping 1529 nm $l = 0$ and $l = 3$ modes, forming an intensity profile with three

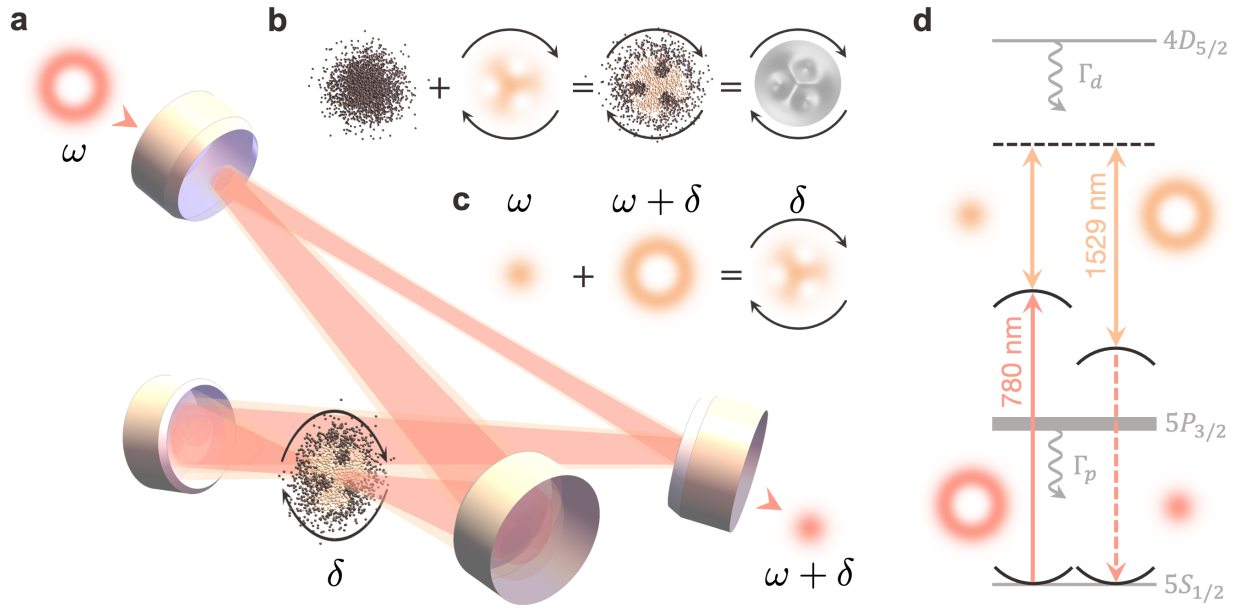

Figure 6.1: **Modulated atomic samples as sculptable optics.** This work demonstrates the conversion of photons between two Laguerre-Gaussian modes of orbital angular momenta $l = 0$ and $l = 3$. These modes are the non-degenerate eigenmodes of the twisted cavity depicted in **a**, which hosts 780 nm probe modes (red) and slightly larger, copropagating 1529 nm modulation modes (orange). We inject $l = 3$ probe photons which are converted to $l = 0$ via coupling to an atomic sample of ^{87}Rb atoms at the waist of the cavity. **b,** The optical susceptibility of this sample is modulated in space and time by the 1529 nm modulation beam, effectively sculpting a rotating, mode-coupling optic from the atomic cloud with a spatiotemporally-varying refractive index. This coupling arises from the spatial profile used modulate the atomic sample, which is comprised of both $l = 0$ and $l = 3$ modes as illustrated in **c**. When an $l = 0$ mode of frequency ω is spatially overlapped with an $l = 3$ mode of frequency $\omega+\delta$, the resulting interference profile is a three-holed pattern that rotates at the frequency difference between the two modes. When the atomic sample is illumated with this rotating profile, the optical susceptibility of the sample is modulated according to the profile of the modulation beam, effectively sculpting the stationary sample into a rotating, three-fold symmetric optic. The relevant atomic levels for this mode conversion process are illustrated in **d**. We inject 780 nm, $l = 3$ probe photons in the dispersive regime, 130 MHz detuned from the $5S_{1/2} \rightarrow 5P_{3/2}$ atomic resonance. These photons are coupled by the far-detuned 1529 nm modulation beam to the $l = 0$ cavity mode at 780 nm. If mode conversion is successful, $l = 0$ photons will emerge from the cavity at a frequency 65 MHz lower than that of the injected $l = 3$ photons as a result of the frequency difference between non-degenerate cavity eigenmodes. The optical susceptibility of the atomic cloud is modulated via the time-varying, spatially-dependent optical Stark shift of the $5P_{3/2}$ energy, which periodically shifts the $5S_{1/2} \rightarrow 5P_{3/2}$ atomic resonance further from the cavity resonances.

'holes' that rotates at the frequency difference (≈ 65 MHz) between the modes. Illuminating the atomic sample with this profile changes the resonance condition of individual atoms with intracavity 780 nm photons, creating a spatiotemporally-varying optical susceptibility across the sample that adopts the modulation beam profile (Fig. 6.1c). As the modulation beam profile is comprised of both the $l = 0$ and $l = 3$ modes, a coupling is engineered between the $l = 0$ and $l = 3$ modes at 780 nm. Note that the atomic sample is stationary whereas the modulation profile rotates, enabling far faster temporal modulation of incident probe light than that which can be achieved by a real, rotating optic. We utilize the atomic level scheme illustrated in Fig. 6.1d, which may be understood as a near-resonant four-wave mixing process.

We begin our experimental sequence by transporting a sample of laser-cooled ^{87}Rb into the waist of our twisted optical cavity from a magneto-optical trap. The modulation beam and weak probe beam co-propagate through the cavity and illuminate the atomic sample for a probe time of 10 ms. Probe photons are injected into the $l = 3$ cavity eigenmode. These photons pass through the modulated atomic sample and the resulting photons are collected on the cavity output during the probe time. See Appendix A for additional details about the experimental setup.

6.3 Experimental results

We search for $l = 3 \rightarrow l = 0$ mode conversion for several different combinations of modulation beam intensity and atom number by collecting only $l = 0$ light from the cavity using a single mode fiber as a filter (Fig. 6.2a). For each of these combinations, we scan the frequency of the probe beam about a point in the dispersive regime, where the $l = 0$ and $l = 3$ cavity resonances are detuned from the atomic $5P_{3/2}$ state as illustrated in Fig. 6.1d. This scan generates the $l = 0$ spectra in Fig. 6.2b. We observe an increase in the $l = 3 \rightarrow l = 0$ internal conversion efficiency, $\mathcal{E}_{3\rightarrow 0}$, for increasing Ω and $N\eta$, in effect the modulation beam

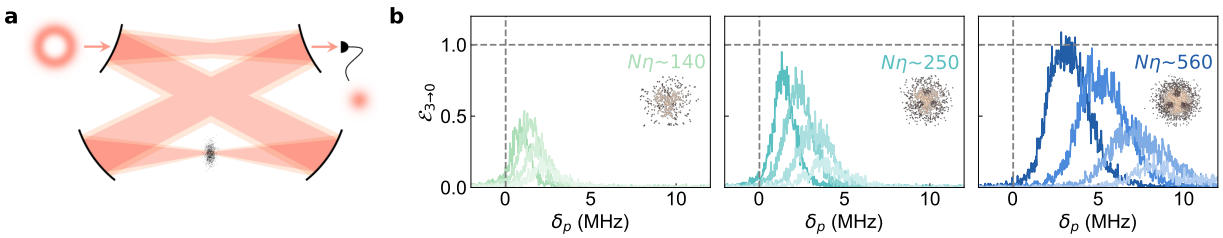

Figure 6.2: **Conversion in the cavity spectra.** We inject $l = 3$ probe photons into the twisted cavity and read out only on $l = 0$ using a single mode fiber as illustrated in **a**. For various combinations of Ω and $N\eta$, corresponding with the modulation beam intensity and atom number, respectively, we observe the $l = 0$ transmission spectrum by scanning the frequency of the probe laser frequency, δ_p, about the bare $l = 3$ transmission frequency ($\delta_p = 0$ MHz). In **b**, we plot the $l = 0$ transmission spectrum (normalized as an internal conversion efficiency) at $\Omega/(2\pi) = (0.7, 1.3, 2.1, 3.5)$ GHz (light to dark) for each value of $N\eta = (140, 250, 560)$. The $l = 3 \to l = 0$ conversion efficiency, $\mathcal{E}_{3\to0}$, increases for increasing Ω and $N\eta$, reaching near unity for the highest values of Ω and $N\eta$. Intuitively, $\mathcal{E}_{3\to0}$ should increase for increasing modulation beam intensity and atom number, akin to increasing the refractive index variation and density of our effective, intracavity optic from zero. The $l = 0$ transmission curves shift toward lower frequencies with increasing Ω due to the increasing Stark shift of the $5P_{3/2}$ resonance with higher modulation beam intensity, which lessens the dispersive shift of the $l = 0$ transmission curves away from the bare $l = 3$ transmission frequency.

intensity and resonant optical density, respectively. See Appendix A for additional details about $\mathcal{E}_{3\to0}$. Here, $N\eta$ is the collective cooperativity [117] where N is the atom number and η is the single atom cooperativity. This quantity can be generally interpreted as the number of times a photon is lensed by the atomic sample before it leaks out of the cavity. See Appendix A for additional details about $N\eta$ and Ω, respectively. As Ω increases, we observe the $l = 0$ cavity transmissions collapse leftward toward the location of the bare $l = 3$ transmission at $\delta_p = 0$. This behavior is a result of the $5P_{3/2}$ state energetically shifting away from the $l = 0$ and $l = 3$ cavity resonances at higher modulation beam intensities, reducing the dispersive shift of the resonances.

To verify photons are indeed converted into the $l = 0$ mode of the cavity, we perform a spatial and frequency analysis of the cavity output. In principle, the modulated atomic sample induces a coupling between the $l = 3$ mode and many other spatial modes. However,

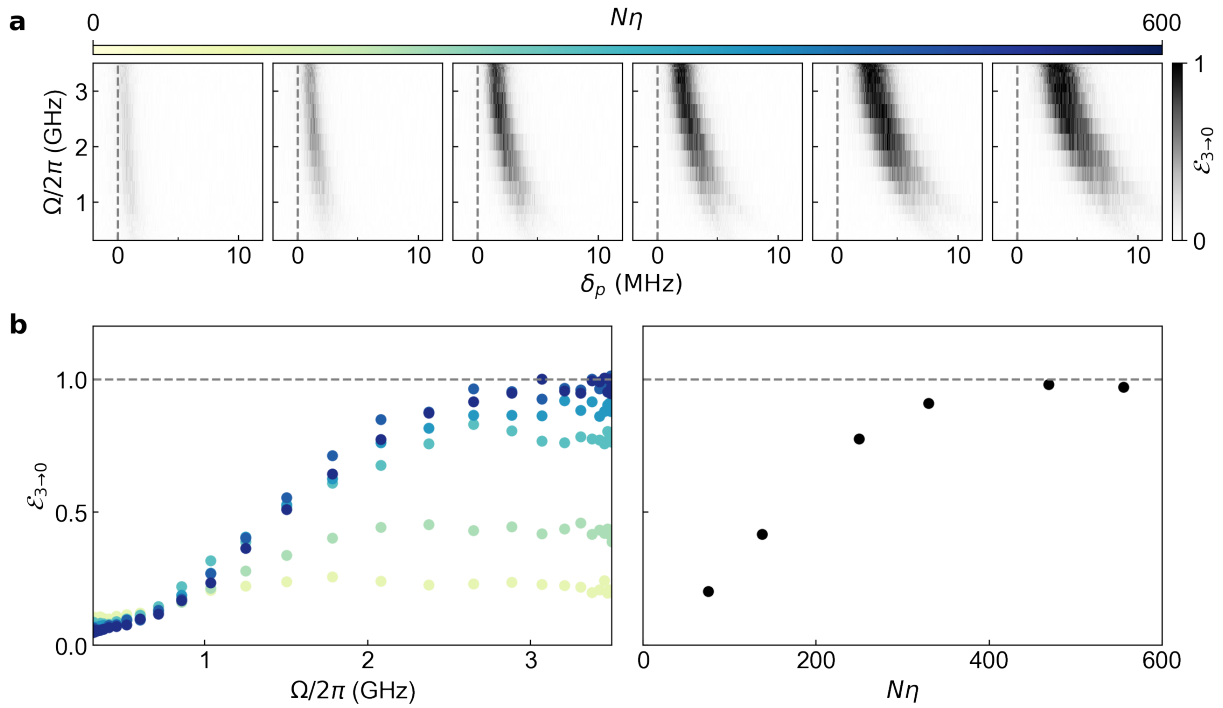

Figure 6.3: **Saturation in conversion efficiency.** We further examine $l = 3 \rightarrow l = 0$ conversion in two-dimensional sweeps over δ_p and Ω for additional values of $N\eta$. In **a**, $\mathcal{E}_{3\rightarrow0}$ increases for increasing Ω and $N\eta$. Plotting the numerical values of $\mathcal{E}_{3\rightarrow0}$ in **b** at each slice of Ω for all $N\eta$ **(left)** and for each $N\eta$ at maximum Ω **(right)** elucidates both the attainment and *saturation* of conversion near $\mathcal{E}_{3\rightarrow0}$=1. This internal efficiency corresponds to a maximum external efficiency of 25% due to the double-ended nature of our cavity. In general, light is fully transmitted through a double-ended cavity when the reflected light cancels with the light that leaks out of the cavity. This idea assumes the two cavity ends, or mirrors, have equal transmission coefficients and light drives the cavity from one side. Even though the two ends of our twisted cavity have equal transmission coefficients, the conversion of light from the injected mode to another mode acts as loss which breaks the cavity impedance matching that enables full transmission. See SI A.1.2 and A.1.5 for more details. Points are larger than their error bars of one standard deviation.

with the exception of the $l = 6$ mode, these modes are Purcell suppressed because they are non-resonant. Despite a potential $3 \leftrightarrow 6$ coupling, we do not observe $l = 6$ light on the cavity output, likely because the $l = 6$ mode is further detuned from the $5S_{1/2} \leftrightarrow 5P_{3/2}$ atomic resonance compared to $l = 3$ and $l = 0$ modes (see Appendix A). Thus, in general, the non-degenerate mode structure of the cavity improves the isolation of a target mode by frequency discrimination.

The increase of $\mathcal{E}_{3\to0}$ with Ω and $N\eta$ can be interpreted intuitively in the context of sculpting an effective optic from the atomic sample. For $\Omega = 0$, there is no modulation of the atomic sample. Probe photons pass through an effective optic that imparts an almost completely flat phase, providing essentially no coupling between the $l = 3$ and $l = 0$ modes. For $N\eta = 0$, no atoms are present; there is no effective optic. Thus, $\mathcal{E}_{3\to0}$ regardless of Ω. For $\Omega > 0$ and $N\eta > 0$, we begin to observe $l = 3$ to $l = 0$ conversion as the effective optic acquires density and a spatially-dependent optical susceptibility.

Fig. 6.3 is a more in-depth investigation of $\mathcal{E}_{3\to0}$ as a function of Ω and $N\eta$. $\mathcal{E}_{3\to0}$ increases for increasing Ω and $N\eta$ and *saturates* near unity. In a double-ended cavity like ours, where light can leak out one of two cavity mirrors, $\mathcal{E}_{3\to0}$=1 corresponds to a maximum *external* efficiency of 25% for lossless mirrors. For a general double-ended cavity comprised of two equally-transmissive cavity mirrors, incident light can be fully transmitted as the cavity is impedance matched. If a mode-converting element is placed within the cavity, this impedance matching condition is broken, limiting the amount of light, both converted and unconverted, that exits the cavity through the output mirror. In a single-ended cavity, the maximum external efficiency increases to 100% (see Appendix A).

6.4 Conclusion

We have demonstrated a highly efficient method to simultaneously manipulate photonic degrees of freedom by spatiotemporally modulating the optical susceptibility of an atomic sample. In our twisted optical cavity, we observe $l = 3 \to l = 0$ conversion at an internal efficiency near unity. Extending this method to a low loss, single-ended cavity will provide conversion near 100% efficiency for both internal and external efficiencies. This method is additionally extendable to other atomic species, arbitrary cavity geometries, different propagation eigenmodes, polarization conversion (see Appendix A), and the coherent conversion of single photons [216]. Mode conversion via optical susceptibility modulation might also

find applications in quantum state preparation, quantum information, and development as a tabletop device. One might use this method to grow topological few-body states of light by controllably adding orbital angular momentum to intracavity photons [217], convert within mode pairs for mode-division multiplexed transmission [177], or create a miniaturized device based on intracavity electro-optic elements whose refractive indices are modulated in space and time.

CHAPTER 7

OUTLOOK

Using the platform of atoms in cavities to induce effective interactions between photons in a synthetic gauge field, we have demonstrated the formation of topologically ordered photonic quantum materials—namely, Laughlin states. Using the same platform, we have additionally demonstrated how the manipulation of atoms with light can lead to photonic mode conversion at high efficiency. Both of these research topics have room to grow.

In the scope of quantum materials made of light, our most recent twisted lens cavity shows promise in creating a large-scale degenerate manifold of photonic modes to support the formation of larger Laughlin states. With this state growth comes additional challenges—how do we reliably prepare a few-particle state, and how do we make useful measurements to assess the state we've created? The answers to these questions may lie in dissipative state preparation, Rydberg-enhanced detection, and spatial correlation measurements via imaging as full quantum state tomography becomes impractical for high particle number.

In the scope of multimode photonics, the idea of mode conversion via spatiotemporally modulated optical susceptibility can be further streamlined in the platform of electro-optic crystals in cavities. Exploring mode conversion, and perhaps other concepts such as optical isolation, using this platform would be an interesting project for future lab members.

REFERENCES

[1] Xiao-Gang Wen. An introduction of topological orders. *URL http://web. mit. edu/physics/people/faculty/docs/wen_ intro_ topological_ orders. pdf*, 34:54, 2016.

[2] Xie Chen, Zheng-Cheng Gu, and Xiao-Gang Wen. Local unitary transformation, long-range quantum entanglement, wave function renormalization, and topological order. *Phys. Rev. B*, 82(15):155138, 2010.

[3] Chetan Nayak, Steven H. Simon, Ady Stern, Michael Freedman, and Sankar Das Sarma. Non-abelian anyons and topological quantum computation. *Rev. Mod. Phys.*, 80:1083–1159, Sep 2008.

[4] John Clai Owens, Margaret G Panetta, Brendan Saxberg, Gabrielle Roberts, Srivatsan Chakram, Ruichao Ma, Andrei Vrajitoarea, Jonathan Simon, and David I Schuster. Chiral cavity quantum electrodynamics. *Nature Physics*, 18(9):1048–1052, 2022.

[5] Kirill I Bolotin, Fereshte Ghahari, Michael D Shulman, Horst L Stormer, and Philip Kim. Observation of the fractional quantum hall effect in graphene. *Nature*, 462(7270):196, 2009.

[6] Rong-Chun Ge and Michael Kolodrubetz. Floquet engineering flat bands for bosonic fractional quantum hall with superconducting circuits. *Physical Review B*, 104(3):035427, 2021.

[7] NR Cooper. Fractional quantum hall states of bosons: Properties and prospects for experimental realization. In *Fractional Quantum Hall Effects: New Developments*, pages 487–521. World Scientific, 2020.

[8] Julian Léonard, Sooshin Kim, Joyce Kwan, Perrin Segura, Fabian Grusdt, Cécile Repellin, Nathan Goldman, and Markus Greiner. Realization of a fractional quantum hall state with ultracold atoms. *arXiv preprint arXiv:2210.10919*, 2022.

[9] Ling Lu, John D Joannopoulos, and Marin Soljačić. Topological photonics. *Nature photonics*, 8(11):821–829, 2014.

[10] Tomoki Ozawa, Hannah M Price, Alberto Amo, Nathan Goldman, Mohammad Hafezi, Ling Lu, Mikael C Rechtsman, David Schuster, Jonathan Simon, Oded Zilberberg, et al. Topological photonics. *Reviews of Modern Physics*, 91(1):015006, 2019.

[11] Christopher J Foot. *Atomic physics*, volume 7. OUP Oxford, 2004.

[12] M Marinescu, HR Sadeghpour, and A Dalgarno. Dispersion coefficients for alkali-metal dimers. *Physical Review A*, 49(2):982, 1994.

[13] Daniel A Steck. Quantum and atom optics. 2007.

[14] V Alan Kostelecký, Michael Martin Nieto, and D Rodney Truax. Fine structure and analytical quantum-defect wave functions. *Physical Review A*, 38(9):4413, 1988.

[15] Mark Saffman, Thad G Walker, and Klaus Mølmer. Quantum information with rydberg atoms. *Reviews of modern physics*, 82(3):2313, 2010.

[16] Antoine Browaeys, Daniel Barredo, and Thierry Lahaye. Experimental investigations of the dipolar interactions between single rydberg atoms. *arXiv preprint arXiv:1603.04603*, 2016.

[17] Sylvain Ravets, Henning Labuhn, Daniel Barredo, Lucas Béguin, Thierry Lahaye, and Antoine Browaeys. Coherent dipole–dipole coupling between two single rydberg atoms at an electrically-tuned förster resonance. *Nature Physics*, 10(12):914–917, 2014.

[18] Johannes Maximilian Nipper. Interacting rydberg atoms: Coherent control at förster resonances and polar homonuclear molecules. 2012.

[19] Nikola Šibalić and Charles S Adams. *Rydberg physics*. IOP Publishing, 2018.

[20] Rémy Legaie. Coherent control of rydberg atoms using sub-khz linewidth excitation lasers. 2020.

[21] Sebastian Weber, Christoph Tresp, Henri Menke, Alban Urvoy, Ofer Firstenberg, Hans Peter Büchler, and Sebastian Hofferberth. Calculation of rydberg interaction potentials. *Journal of Physics B: Atomic, Molecular and Optical Physics*, 50(13):133001, 2017.

[22] Myron L Zimmerman, Michael G Littman, Michael M Kash, and Daniel Kleppner. Stark structure of the rydberg states of alkali-metal atoms. *Physical Review A*, 20(6):2251, 1979.

[23] Benjamin L Augenbraun. *Scalar Polarizability of the Indium 6P1/2 State: Atomic Beam Stark Shift Measurements Using Two-Step Laser Spectroscopy*. PhD thesis, Citeseer, 2015.

[24] David J Griffiths and Darrell F Schroeter. *Introduction to quantum mechanics*. Cambridge university press, 2018.

[25] Daniel A Steck. Rubidium 87 d line data. 2001.

[26] Ennio Arimondo, M Inguscio, and P Violino. Experimental determinations of the hyperfine structure in the alkali atoms. *Reviews of Modern Physics*, 49(1):31, 1977.

[27] Jun Ye and Theresa W Lynn. Applications of optical cavities in modern atomic, molecular, and optical physics. In *Advances in Atomic, Molecular, and Optical Physics*, volume 49, pages 1–83. Elsevier, 2003.

[28] Anthony E Siegman. *Lasers*. University science books, 1986.

[29] Anthony A Tovar and Lee W Casperson. Generalized beam matrices: Gaussian beam propagation in misaligned complex optical systems. *JOSA A*, 12(7):1522–1533, 1995.

[30] Peter W Milonni and Joseph H Eberly. *Laser physics*. John Wiley & Sons, 2010.

[31] Wolf Weimer. Probing superfluid properties in strongly correlated fermi gases with high spatial resolution. 2014.

[32] Warren Nagourney. *Quantum electronics for atomic physics and telecommunication*. OUP Oxford, 2014.

[33] Albert Ryou. *Designing, Probing, and Stabilizing Exotic Fabry-Perot Cavities for Studying Strongly Correlated Light*. The University of Chicago, 2017.

[34] Jérôme Poirson, Fabien Bretenaker, Marc Vallet, and Albert Le Floch. Analytical and experimental study of ringing effects in a fabry–perot cavity. application to the measurement of high finesses. *JOSA B*, 14(11):2811–2817, 1997.

[35] H Mabuchi and AC Doherty. Cavity quantum electrodynamics: coherence in context. *Science*, 298(5597):1372–1377, 2002.

[36] B Keimer and JE Moore. The physics of quantum materials. *Nature Physics*, 13(11):1045–1055, 2017.

[37] Crispin W Gardiner and Matthew J Collett. Input and output in damped quantum systems: Quantum stochastic differential equations and the master equation. *Physical Review A*, 31(6):3761, 1985.

[38] Jonathan Simon. *Cavity QED with atomic ensembles*. Harvard University, 2010.

[39] Nathan Schine. *Quantum Hall Physics with Photons*. PhD thesis, University of Chicago, 2019.

[40] Aziza Suleymanzade. *Millimeter Wave Photons for Hybrid Quantum Systems*. PhD thesis, The University of Chicago, 2021.

[41] Mark Stone. *Hybrid Cavity QED with Rydberg Atoms*. PhD thesis, The University of Chicago, 2021.

[42] M.O. Scully and M.S. Zubairy. *Quantum Optics*. Cambridge University Press.

[43] Dorian Gangloff, Molu Shi, Tailin Wu, Alexei Bylinskii, Boris Braverman, Michael Gutierrez, Rosanna Nichols, Junru Li, Kai Aichholz, Marko Cetina, et al. Preventing and reversing vacuum-induced optical losses in high-finesse tantalum (v) oxide mirror coatings. *Optics express*, 23(14):18014–18028, 2015.

[44] Logan W. Clark, Nathan Schine, Claire Baum, Ningyuan Jia, and Jonathan Simon. Observation of Laughlin states made of light. *Nature 2020 582:7810*, 582(7810):41–45, 6 2020.

[45] Jean Dalibard and Claude Cohen-Tannoudji. Laser cooling below the doppler limit by polarization gradients: simple theoretical models. *JOSA B*, 6(11):2023–2045, 1989.

[46] Logan W. Clark, Ningyuan Jia, Nathan Schine, Claire Baum, Alexandros Georgakopoulos, and Jonathan Simon. Interacting Floquet polaritons. *Nature 2019 571:7766*, 571(7766):532–536, 7 2019.

[47] Matt Jaffe, Lukas Palm, Claire Baum, Lavanya Taneja, and Jonathan Simon. Aberrated optical cavities. *Physical Review A*, 104(1):013524, 2021.

[48] Matt Jaffe, Lukas Palm, Claire Baum, Lavanya Taneja, Aishwarya Kumar, and Jonathan Simon. Understanding and suppressing backscatter in optical resonators. *Optica*, 9(8):878–885, Aug 2022.

[49] M.Z. Hasan and C.L. Kane. Colloquium: Topological insulators. *Reviews of Modern Physics*, 82:3045–3067, Nov 2010.

[50] Ady Stern. Anyons and the quantum hall effect—a pedagogical review. *Annals of Physics*, 323(1):204–249, 2008.

[51] Horst L Stormer, Daniel C Tsui, and Arthur C Gossard. The fractional quantum hall effect. *Reviews of Modern Physics*, 71(2):S298, 1999.

[52] D. C. Tsui, H. L. Stormer, and A. C. Gossard. Two-dimensional magnetotransport in the extreme quantum limit. *Phys. Rev. Lett.*, 48:1559–1562, May 1982.

[53] Xu Du, Ivan Skachko, Fabian Duerr, Adina Luican, and Eva Y Andrei. Fractional quantum hall effect and insulating phase of dirac electrons in graphene. *Nature*, 462(7270):192, 2009.

[54] Cory R Dean, L Wang, P Maher, C Forsythe, Fereshte Ghahari, Y Gao, Jyoti Katoch, M Ishigami, P Moon, M Koshino, et al. Hofstadter's butterfly and the fractal quantum hall effect in moiré superlattices. *Nature*, 497(7451):598, 2013.

[55] Eric M Spanton, Alexander A Zibrov, Haoxin Zhou, Takashi Taniguchi, Kenji Watanabe, Michael P Zaletel, and Andrea F Young. Observation of fractional chern insulators in a van der waals heterostructure. *Science*, 360(6384):62–66, 2018.

[56] Immanuel Bloch, Jean Dalibard, and Wilhelm Zwerger. Many-body physics with ultracold gases. *Reviews of Modern Physics*, 80(3):885, 2008.

[57] Iacopo Carusotto and Cristiano Ciuti. Quantum fluids of light. *Reviews of Modern Physics*, 85(1):299, 2013.

[58] Tomoki Ozawa, Hannah M Price, Alberto Amo, Nathan Goldman, Mohammad Hafezi, Ling Lu, Mikael C Rechtsman, David Schuster, Jonathan Simon, Oded Zilberberg, et al. Topological photonics. *Reviews of Modern Physics*, 91(1):015006, 2019.

[59] NR Cooper, J Dalibard, and IB Spielman. Topological bands for ultracold atoms. *Reviews of Modern Physics*, 91(1):015005, 2019.

[60] Nigel R Cooper. Rapidly rotating atomic gases. *Advances in Physics*, 57(6):539–616, 2008.

[61] Nathan Gemelke, Edina Sarajlic, and Steven Chu. Rotating few-body atomic systems in the fractional quantum hall regime. *arXiv preprint arXiv:1007.2677*, 2010.

[62] André Eckardt. Colloquium: Atomic quantum gases in periodically driven optical lattices. *Reviews of Modern Physics*, 89(1):011004, 2017.

[63] M Eric Tai, Alexander Lukin, Matthew Rispoli, Robert Schittko, Tim Menke, Dan Borgnia, Philipp M Preiss, Fabian Grusdt, Adam M Kaufman, and Markus Greiner. Microscopy of the interacting harper–hofstadter model in the two-body limit. *Nature*, 546(7659):519, 2017.

[64] Sarang Gopalakrishnan, Benjamin L. Lev, and Paul M. Goldbart. Emergent crystallinity and frustration with bose–einstein condensates in multimode cavities. *Nature Physics*, 5(11):845–850, 2009.

[65] Arne Wickenbrock, Michal Hemmerling, Gordon RM Robb, Clive Emary, and Ferruccio Renzoni. Collective strong coupling in multimode cavity qed. *Physical Review A*, 87(4):043817, 2013.

[66] Helmut Ritsch, Peter Domokos, Ferdinand Brennecke, and Tilman Esslinger. Cold atoms in cavity-generated dynamical optical potentials. *Rev. Mod. Phys.*, 85:553–601, Apr 2013.

[67] James S Douglas, Hessam Habibian, C-L Hung, Alexey V Gorshkov, H Jeff Kimble, and Darrick E Chang. Quantum many-body models with cold atoms coupled to photonic crystals. *Nature Photonics*, 9(5):326, 2015.

[68] Julian Léonard, Andrea Morales, Philip Zupancic, Tilman Esslinger, and Tobias Donner. Supersolid formation in a quantum gas breaking a continuous translational symmetry. *Nature*, 543(7643):87, 2017.

[69] Varun D Vaidya, Yudan Guo, Ronen M Kroeze, Kyle E Ballantine, Alicia J Kollár, Jonathan Keeling, and Benjamin L Lev. Tunable-range, photon-mediated atomic interactions in multimode cavity qed. *Physical Review X*, 8(1):011002, 2018.

[70] Andreas Wallraff, David I Schuster, Alexandre Blais, L Frunzio, R-S Huang, J Majer, S Kumar, Steven M Girvin, and Robert J Schoelkopf. Strong coupling of a single photon to a superconducting qubit using circuit quantum electrodynamics. *Nature*, 431(7005):162–167, 2004.

[71] P. Roushan, C. Neill, A. Megrant, Y. Chen, R. Babbush, R. Barends, B. Campbell, Z. Chen, B. Chiaro, A. Dunsworth, et al. Chiral ground-state currents of interacting photons in a synthetic magnetic field. *Nature Physics*, 13(2):146–151, 2017.

[72] Kevin M Birnbaum, Andreea Boca, Russell Miller, Allen D Boozer, Tracy E Northup, and H Jeff Kimble. Photon blockade in an optical cavity with one trapped atom. *Nature*, 436(7047):87, 2005.

[73] Thibault Peyronel, Ofer Firstenberg, Qi-Yu Liang, Sebastian Hofferberth, Alexey V Gorshkov, Thomas Pohl, Mikhail D Lukin, and Vladan Vuletić. Quantum nonlinear optics with single photons enabled by strongly interacting atoms. *Nature*, 488(7409):57–60, 2012.

[74] JD Thompson, TG Tiecke, NP de Leon, J Feist, AV Akimov, M Gullans, AS Zibrov, V Vuletić, and MD Lukin. Coupling a single trapped atom to a nanoscale optical cavity. *Science*, 340(6137):1202–1205, 2013.

[75] Ningyuan Jia, Nathan Schine, Alexandros Georgakopoulos, Albert Ryou, Logan W. Clark, Ariel Sommer, and Jonathan Simon. A strongly interacting polaritonic quantum dot. *Nature Physics*, 14(6):550–554, 2018.

[76] Sabyasachi Barik, Aziz Karasahin, Christopher Flower, Tao Cai, Hirokazu Miyake, Wade DeGottardi, Mohammad Hafezi, and Edo Waks. A topological quantum optics interface. *Science*, 359(6376):666–668, 2018.

[77] Mohammad Hafezi, S Mittal, J Fan, A Migdall, and JM Taylor. Imaging topological edge states in silicon photonics. *Nature Photonics*, 7(12):1001, 2013.

[78] Mikael C Rechtsman, Julia M Zeuner, Yonatan Plotnik, Yaakov Lumer, Daniel Podolsky, Felix Dreisow, Stefan Nolte, Mordechai Segev, and Alexander Szameit. Photonic floquet topological insulators. *Nature*, 496(7444):196, 2013.

[79] Nathan Schine, Albert Ryou, Andrey Gromov, Ariel Sommer, and Jonathan Simon. Synthetic landau levels for photons. *Nature*, 534(7609):671–675, Jun 2016. Letter.

[80] Hyang-Tag Lim, Emre Togan, Martin Kroner, Javier Miguel-Sanchez, and Atac Imamoğlu. Electrically tunable artificial gauge potential for polaritons. *Nature Communications*, 8:14540, 2017.

[81] Nathan Schine, Michelle Chalupnik, Tankut Can, Andrey Gromov, and Jonathan Simon. Electromagnetic and gravitational responses of photonic landau levels. *Nature*, 565(7738):173, 2019.

[82] Michael J Hartmann, Fernando GSL Brandao, and Martin B Plenio. Strongly interacting polaritons in coupled arrays of cavities. *Nature Physics*, 2(12):849, 2006.

[83] Andrew D Greentree, Charles Tahan, Jared H Cole, and Lloyd CL Hollenberg. Quantum phase transitions of light. *Nature Physics*, 2(12):856, 2006.

[84] Dimitris G Angelakis, Marcelo Franca Santos, and Sougato Bose. Photon-blockade-induced mott transitions and x y spin models in coupled cavity arrays. *Physical Review A*, 76(3):031805, 2007.

[85] Jaeyoon Cho, Dimitris G Angelakis, and Sougato Bose. Fractional quantum hall state in coupled cavities. *Physical Review Letters*, 101(24):246809, 2008.

[86] A Nunnenkamp, Jens Koch, and SM Girvin. Synthetic gauge fields and homodyne transmission in jaynes–cummings lattices. *New Journal of Physics*, 13(9):095008, 2011.

[87] Andrew LC Hayward, Andrew M Martin, and Andrew D Greentree. Fractional quantum hall physics in jaynes-cummings-hubbard lattices. *Physical Review Letters*, 108(22):223602, 2012.

[88] Mohammad Hafezi, Mikhail D Lukin, and Jacob M Taylor. Non-equilibrium fractional quantum hall state of light. *New Journal of Physics*, (6):063001.

[89] RO Umucalılar, M Wouters, and I Carusotto. Probing few-particle laughlin states of photons via correlation measurements. *Phys. Rev. A*, 89(2):023803, 2014.

[90] M. Saffman, T. G. Walker, and K. Mølmer. Quantum information with rydberg atoms. *Rev. Mod. Phys.*, 82:2313–2363, Aug 2010.

[91] Ariel Sommer and Jonathan Simon. Engineering photonic floquet hamiltonians through fabry pérot resonators. *New Journal of Physics*, 18(3):035008, 2016.

[92] Nathan Schine, Albert Ryou, Andrey Gromov, Ariel Sommer, and Jonathan Simon. Synthetic landau levels for photons. *Nature*, 534(7609):671, 2016.

[93] Logan W Clark, Ningyuan Jia, Nathan Schine, Claire Baum, Alexandros Georgakopoulos, and Jonathan Simon. Interacting floquet polaritons. *accepted in Nature, DOI: 10.1038/s41586-019-1354-5*, 2019.

[94] Jia Ningyuan, Alexandros Georgakopoulos, Albert Ryou, Nathan Schine, Ariel Sommer, and Jonathan Simon. Observation and characterization of cavity rydberg polaritons. *Phys. Rev. A*, 93(4):041802, 2016.

[95] Ningyuan Jia, Nathan Schine, Alexandros Georgakopoulos, Albert Ryou, Logan W Clark, Ariel Sommer, and Jonathan Simon. A strongly interacting polaritonic quantum dot. *Nature Physics*, 14(6):550, 2018.

[96] Ariel Sommer, Hans Peter Büchler, and Jonathan Simon. Quantum crystals and laughlin droplets of cavity rydberg polaritons. *arXiv:1506.00341*, 2015.

[97] Jonathan D Pritchard, D Maxwell, Alexandre Gauguet, Kevin J Weatherill, MPA Jones, and Charles S Adams. Cooperative atom-light interaction in a blockaded rydberg ensemble. *Physical review letters*, 105(19):193603, 2010.

[98] Alexandros Georgakopoulos, Ariel Sommer, and Jonathan Simon. Theory of interacting cavity rydberg polaritons. *Quantum Science and Technology*, 4(1):014005, 2018.

[99] Jian-Wei Pan, Zeng-Bing Chen, Chao-Yang Lu, Harald Weinfurter, Anton Zeilinger, and Marek Żukowski. Multiphoton entanglement and interferometry. *Reviews of Modern Physics*, 84(2):777, 2012.

[100] Fabian Grusdt, Fabian Letscher, Mohammad Hafezi, and Michael Fleischhauer. Topological growing of laughlin states in synthetic gauge fields. *Phys. Rev. Lett.*, 113(15):155301, 2014.

[101] Peter A Ivanov, Fabian Letscher, Jonathan Simon, and Michael Fleischhauer. Adiabatic flux insertion and growing of laughlin states of cavity rydberg polaritons. *Phys. Rev. A*, 98(1):013847, 2018.

[102] Eliot Kapit, Mohammad Hafezi, and Steven H Simon. Induced self-stabilization in fractional quantum hall states of light. *Phys. Rev. X*, 4(3):031039, 2014.

[103] M Hafezi, P Adhikari, and JM Taylor. Chemical potential for light by parametric coupling. *Phys. Rev. B*, 92(17):174305, 2015.

[104] RO Umucalılar and I Carusotto. Generation and spectroscopic signatures of a fractional quantum hall liquid of photons in an incoherently pumped optical cavity. *Phys. Rev. A*, 96(5):053808, 2017.

[105] Alberto Biella, Florent Storme, José Lebreuilly, Davide Rossini, Rosario Fazio, Iacopo Carusotto, and Cristiano Ciuti. Phase diagram of incoherently driven strongly correlated photonic lattices. *Physical Review A*, 96(2):023839, 2017.

[106] Ruichao Ma, Brendan Saxberg, Clai Owens, Nelson Leung, Yao Lu, Jonathan Simon, and David I Schuster. A dissipatively stabilized mott insulator of photons. *Nature*, 566(7742):51, 2019.

[107] B Paredes, P Fedichev, JI Cirac, and P Zoller. 1/2-anyons in small atomic bose-einstein condensates. *Physical review letters*, 87(1):010402, 2001.

[108] RO Umucalılar and I Carusotto. Many-body braiding phases in a rotating strongly correlated photon gas. *Physics Letters A*, 377(34-36):2074–2078, 2013.

[109] Fabian Grusdt, Norman Y Yao, D Abanin, Michael Fleischhauer, and E Demler. Interferometric measurements of many-body topological invariants using mobile impurities. *Nature Communications*, 7:11994, 2016.

[110] Shovan Dutta and Erich J. Mueller. Coherent generation of photonic fractional quantum hall states in a cavity and the search for anyonic quasiparticles. *Phys. Rev. A*, 97:033825, Mar 2018.

[111] Elia Macaluso, Tommaso Comparin, Leonardo Mazza, and Iacopo Carusotto. Fusion channels of non-abelian anyons from angular-momentum and density-profile measurements. *arXiv preprint arXiv:1903.03011*, 2019.

[112] Nicolas Regnault and Th Jolicoeur. Quantum hall fractions for spinless bosons. *Phys. Rev. B*, 69(23):235309, 2004.

[113] Alicia J Kollár, Alexander T Papageorge, Kristian Baumann, Michael A Armen, and Benjamin L Lev. An adjustable-length cavity and Bose–Einstein condensate apparatus for multimode cavity QED. *New Journal of Physics*, 17(4):043012, 2015.

[114] Nathan Schine, Michelle Chalupnik, Tankut Can, Andrey Gromov, and Jonathan Simon. Electromagnetic and gravitational responses of photonic Landau levels. *Nature*, 565(7738):173–179, 2019.

[115] Logan W Clark, Nathan Schine, Claire Baum, Ningyuan Jia, and Jonathan Simon. Observation of Laughlin states made of light. *Nature*, 582(7810):41–45, 2020.

[116] David Hunger, Tilo Steinmetz, Yves Colombe, Christian Deutsch, Theodor W Hänsch, and Jakob Reichel. A fiber fabry–perot cavity with high finesse. *New Journal of Physics*, 12(6):065038, 2010.

[117] Haruka Tanji-Suzuki, Ian D Leroux, Monika H Schleier-Smith, Marko Cetina, Andrew T Grier, Jonathan Simon, and Vladan Vuletić. Interaction between atomic ensembles and optical resonators: Classical description. In *Advances in atomic, molecular, and optical physics*, volume 60, pages 201–237. Elsevier, 2011.

[118] Kadir Durak, Chi Huan Nguyen, Victor Leong, Stanislav Straupe, and Christian Kurtsiefer. Diffraction-limited Fabry–Pérot cavity in the near concentric regime. *New Journal of Physics*, 16(10):103002, 2014.

[119] Martin Zeppenfeld and Pepijn WH Pinkse. Calculating the fine structure of a Fabry-Pérot resonator using spheroidal wave functions. *Optics Express*, 18(9):9580–9591, 2010.

[120] Jorrit Visser and Gerard Nienhuis. Spectrum of an optical resonator with spherical aberration. *JOSA A*, 22(11):2490–2497, 2005.

[121] Thijs Klaassen. *Imperfect Fabry-Pérot resonators*. PhD thesis, Leiden University, 2006.

[122] Holger Laabs and Ari T. Friberg. Nonparaxial eigenmodes of stable resonators. *IEEE Journal of Quantum Electronics*, 35(2):198–207, feb 1999.

[123] Ariel Sommer and Jonathan Simon. Engineering photonic floquet hamiltonians through fabry–pérot resonators. *New Journal of Physics*, 18(3):035008, 2016.

[124] Anthony E Siegman. *Lasers*. University Science Books, 1986.

[125] Kurt Bernardo. Wolf. *Geometric optics on phase space*. Springer, 2004.

[126] Herbert Walther, Benjamin TH Varcoe, Berthold-Georg Englert, and Thomas Becker. Cavity quantum electrodynamics. *Reports on Progress in Physics*, 69(5):1325, 2006.

[127] T. Yoshle, A. Scherer, J. Hendrickson, G. Khitrova, H. M. Gibbs, G. Rupper, C. Ell, O. B. Shchekin, and D. G. Deppe. Vacuum Rabi splitting with a single quantum dot in a photonic crystal nanocavity. *Nature 2004 432:7014*, 432(7014):200–203, nov 2004.

[128] J. P. Reithmaier, G. Sęk, A. Löffler, C. Hofmann, S. Kuhn, S. Reitzenstein, L. V. Keldysh, V. D. Kulakovskii, T. L. Reinecke, and A. Forchel. Strong coupling in a single quantum dot-semiconductor microcavity system. *Nature*, 432(7014):197–200, nov 2004.

[129] Tian Zhong, Jonathan M. Kindem, John G. Bartholomew, Jake Rochman, Ioana Craiciu, Varun Verma, Sae Woo Nam, Francesco Marsili, Matthew D. Shaw, Andrew D. Beyer, and Andrei Faraon. Optically Addressing Single Rare-Earth Ions in a Nanophotonic Cavity. *Physical Review Letters*, 121(18):183603, oct 2018.

[130] Mouktik Raha, Songtao Chen, Christopher M Phenicie, Salim Ourari, Alan M Dibos, and Jeff D Thompson. Optical quantum nondemolition measurement of a single rare earth ion qubit. *Nature Communications*, 11(1):1–6, 2020.

[131] Andrei Faraon, Charles Santori, Zhihong Huang, Victor M Acosta, and Raymond G Beausoleil. Coupling of nitrogen-vacancy centers to photonic crystal cavities in monocrystalline diamond. *Physical Review Letters*, 109(3):033604, 2012.

[132] Janine Riedrich-Möller, Carsten Arend, Christoph Pauly, Frank Mucklich, Martin Fischer, Stefan Gsell, Matthias Schreck, and Christoph Becher. Deterministic coupling of a single silicon-vacancy color center to a photonic crystal cavity in diamond. *Nano Letters*, 14(9):5281–5287, 2014.

[133] Leonel N. Menegozzi and Willis E. Lamb. Theory of a ring laser. *Physical Review A*, 8(4):2103–2125, oct 1973.

[134] Hermann A. Haus, Hermann Statz, and Irl W. Smith. Frequency Locking of Modes in a Ring Laser. *IEEE Journal of Quantum Electronics*, 21(1):78–85, 1985.

[135] W. W. Chow, J. Gea-Banacloche, L. M. Pedrotti, V. E. Sanders, W. Schleich, and M. O. Scully. The ring laser gyro. *Reviews of Modern Physics*, 57(1):61–104, jan 1985.

[136] C. Etrich, Paul Mandel, R. Centeno Neelen, R. J.C. Spreeuw, and J. P. Woerdman. Dynamics of a ring-laser gyroscope with backscattering. *Physical Review A*, 46(1):525–536, jul 1992.

[137] Peter Lodahl, Sahand Mahmoodian, Søren Stobbe, Arno Rauschenbeutel, Philipp Schneeweiss, Jürgen Volz, Hannes Pichler, and Peter Zoller. Chiral quantum optics. *Nature*, 541(7638):473–480, 2017.

[138] Zheng Wang, Yidong Chong, J. D. Joannopoulos, and Marin Soljačić. Observation of unidirectional backscattering-immune topological electromagnetic states. *Nature*, 461(7265):772–775, oct 2009.

[139] Mohammad Hafezi, Eugene A. Demler, Mikhail D. Lukin, and Jacob M. Taylor. Robust optical delay lines with topological protection. *Nature Physics*, 7(11):907–912, aug 2011.

[140] Zhe Zhang, Pierre Delplace, and Romain Fleury. Superior robustness of anomalous non-reciprocal topological edge states. *Nature*, 598(7880):293–297, oct 2021.

[141] G. Krenz, S. Bux, S. Slama, C. Zimmermann, and P. W. Courteille. Controlling mode locking in optical ring cavities. *Applied Physics B: Lasers and Optics*, 87(4):643–647, may 2007.

[142] Andreas Ø Svela, Jonathan M Silver, Leonardo Del Bino, Shuangyou Zhang, Michael TM Woodley, Michael R Vanner, and Pascal Del'Haye. Coherent suppression of backscattering in optical microresonators. *Light: Science & Applications*, 9(1):1–8, 2020.

[143] A M Jayich, J C Sankey, B M Zwickl, C Yang, J D Thompson, S M Girvin, A A Clerk, F Marquardt, and J. G.E. Harris. Dispersive optomechanics: A membrane inside a cavity. *New Journal of Physics*, 10(9):095008, sep 2008.

[144] Alan C. Nilsson, Eric K. Gustafson, and Robert L. Byer. Eigenpolarization Theory of Monolithic Nonplanar Ring Oscillators. *IEEE Journal of Quantum Electronics*, 25(4):767–790, 1989.

[145] C. Yelland, J. Hong, M. J. Padgett, M. H. Dunn, and W. Sibbett. A vector approach to the geometrical dependence of polarisation rotation in a non-planar cw Nd:YAG ring laser. *Optics Communications*, 109(5-6):451–456, jul 1994.

[146] S. Pancharatnam. Generalized theory of interference, and its applications. *Proceedings of the Indian Academy of Sciences - Section A 1956 44:5*, 44(5):247–262, nov 1956.

[147] Michael V. Berry. Quantal phase factors accompanying adiabatic changes. *Proceedings of the Royal Society of London. A. Mathematical and Physical Sciences*, 392(1802):45–57, 1984.

[148] Thomas J. Kane and Robert L. Byer. Monolithic, unidirectional single-mode Nd:YAG ring laser. *Optics Letters*, 10(2):65, feb 1985.

[149] G. T. Maker, A. I. Ferguson, and G. P. A. Malcolm. Single-frequency diode-pumped Nd:YAG ring laser with no intracavity elements. *Optics Letters*, 18(21):1813, nov 1993.

[150] Ningyuan Jia, Nathan Schine, Alexandros Georgakopoulos, Albert Ryou, Ariel Sommer, and Jonathan Simon. Photons and polaritons in a broken-time-reversal nonplanar resonator. *Physical Review A*, 97(1):013802, jan 2018.

[151] Philip Zupancic, Philipp M. Preiss, Ruichao Ma, Alexander Lukin, M. Eric Tai, Matthew Rispoli, Rajibul Islam, and Markus Greiner. Ultra-precise holographic beam shaping for microscopic quantum control. *Optics Express*, 24(13):13881, jun 2016.

[152] Claire Baum, Matt Jaffe, Lukas Palm, Aishwarya Kumar, and Jonathan Simon. Optical mode conversion via spatiotemporally modulated atomic susceptibility. *arXiv preprint arXiv:2208.04478*, 2022.

[153] N Baharudin, R Alsaqour, H Shaker, O Alsaqour, and T Alahdal. Review on multiplexing techniques in bandwidth utilization. *Middle-East Journal of Scientific Research*, 18(10):1510–1516, 2013.

[154] Pedram Kheirkhah Sangdeh and Huacheng Zeng. Overview of multiplexing techniques in wireless networks. In *Multiplexing*. IntechOpen London, 2019.

[155] Peter J. Winzer. Optical Networking Beyond WDM. *IEEE Photonics Journal*, 2(4):647 – 651, 2012.

[156] Hideki Ishio, Junichiro Minowa, and Kiyoshi Nosu. Review and status of wavelength-division-multiplexing technology and its application. *Journal of lightwave technology*, 2(4):448–463, 1984.

[157] D. J. Richardson, J. M. Fini, and L. E. Nelson. Space-division multiplexing in optical fibres. *Nature Photonics 2013 7:5*, 7(5):354–362, 4 2013.

[158] Peter J. Winzer. Spatial multiplexing: The next frontier in network capacity scaling. *IET Conference Publications*, 2013(622 CP):372–374, 2013.

[159] Guilherme B. Xavier and Gustavo Lima. Quantum information processing with space-division multiplexing optical fibres. *Communications Physics 2020 3:1*, 3(1):1–11, 1 2020.

[160] Benjamin J. Puttnam, Georg Rademacher, and Ruben S. Luís. Space-division multiplexing for optical fiber communications. *Optica, Vol. 8, Issue 9, pp. 1186-1203*, 8(9):1186–1203, 9 2021.

[161] Yikai Su, Yu He, Haoshuo Chen, Xiaoying Li, and Guifang Li. Perspective on mode-division multiplexing. *Applied Physics Letters*, 118(20):200502, 5 2021.

[162] Peter J. Winzer. Making spatial multiplexing a reality. *Nature Photonics 2014 8:5*, 8(5):345–348, 4 2014.

[163] Cen Xia, Guifang Li, Neng Bai, and Ningbo Zhao. Space-division multiplexing: the next frontier in optical communication. *Advances in Optics and Photonics, Vol. 6, Issue 4, pp. 413-487*, 6(4):413–487, 12 2014.

[164] Alan E. Willner, Jiapeng Zhao, Martin P. J. Lavery, Mohammad Mirhosseini, Robert W. Boyd, Seyed Mohammad Hashemi Rafsanjani, Stone Oliver, and Yiyu Zhou. Using all transverse degrees of freedom in quantum communications based on a generic mode sorter. *Optics Express, Vol. 27, Issue 7, pp. 10383-10394*, 27(7):10383–10394, 4 2019.

[165] K. A. Patel, J. F. Dynes, M. Lucamarini, I. Choi, A. W. Sharpe, Z. L. Yuan, R. V. Penty, and A. J. Shields. Quantum key distribution for 10 Gb/s dense wavelength division multiplexing networks. *Applied Physics Letters*, 104(5):051123, 2 2014.

[166] Nenad Bozinovic, Yang Yue, Yongxiong Ren, Moshe Tur, Poul Kristensen, Hao Huang, Alan E. Willner, and Siddharth Ramachandran. Terabit-scale orbital angular momentum mode division multiplexing in fibers. *Science*, 340(6140):1545–1548, 6 2013.

[167] Jun Sakaguchi, Yoshinari Awaji, Naoya Wada, Atsushi Kanno, Tetsuya Kawanishi, Tetsuya Hayashi, Toshiki Taru, Tetsuya Kobayashi, and Masayuki Watanabe. Space division multiplexed transmission of 109-Tb/s data signals using homogeneous seven-core fiber. *Journal of Lightwave Technology*, 30(4):658–665, 2012.

[168] Jian Wang, Jeng Yuan Yang, Irfan M. Fazal, Nisar Ahmed, Yan Yan, Hao Huang, Yongxiong Ren, Yang Yue, Samuel Dolinar, Moshe Tur, and Alan E. Willner. Terabit free-space data transmission employing orbital angular momentum multiplexing. *Nature Photonics 2012 6:7*, 6(7):488–496, 6 2012.

[169] TC Ralph, KJ Resch, and Alexei Gilchrist. Efficient toffoli gates using qudits. *Physical Review A*, 75(2):022313, 2007.

[170] Dong-Xu Chen, Rui-Feng Liu, Pei Zhang, Yun-Long Wang, Hong-Rong Li, Hong Gao, and Fu-Li Li. Realization of quantum permutation algorithm in high dimensional hilbert space. *Chinese Physics B*, 26(6):060305, 2017.

[171] Gabriel Molina-Terriza, Juan P. Torres, and Lluis Torner. Twisted photons. *Nature Physics 2007 3:5*, 3(5):305–310, 2007.

[172] Sandeep K. Goyal and Thomas Konrad. Teleporting photonic qudits using multimode quantum scissors. *Scientific Reports 2013 3:1*, 3(1):1–4, 12 2013.

[173] Juan Carlos García-Escartín and Pedro Chamorro-Posada. Quantum multiplexing with the orbital angular momentum of light. *Physical Review A - Atomic, Molecular, and Optical Physics*, 78(6):062320, 12 2008.

[174] Daniele Cozzolino, Beatrice Da Lio, Davide Bacco, and Leif Katsuo Oxenløwe. High-dimensional quantum communication: benefits, progress, and future challenges. *Advanced Quantum Technologies*, 2(12):1900038, 2019.

[175] Manuel Erhard, Robert Fickler, Mario Krenn, and Anton Zeilinger. Twisted photons: new quantum perspectives in high dimensions. *Light: Science & Applications*, 7(3):17146–17146, 2018.

[176] Mohammad Mirhosseini, Omar S. Magaña-Loaiza, Malcolm N. O'Sullivan, Brandon Rodenburg, Mehul Malik, Martin P.J. Lavery, Miles J. Padgett, Daniel J. Gauthier, and Robert W. Boyd. High-dimensional quantum cryptography with twisted light. *New Journal of Physics*, 17(3):033033, 3 2015.

[177] Alan E Willner, Hao Huang, Yan Yan, Yongxiong Ren, Nisar Ahmed, Goudong Xie, Changjing Bao, L Li, Y Cao, Z Zhao, et al. Optical communications using orbital angular momentum beams. *Advances in optics and photonics*, 7(1):66–106, 2015.

[178] A. Mair, A. Vaziri, G. Weihs, and A. Zeilinger. Entanglement of the orbital angular momentum states of photons. *Nature 2001 412:6844*, 412(6844):313–316, 7 2001.

[179] Mario Krenn, Marcus Huber, Robert Fickler, Radek Lapkiewicz, Sven Ramelow, and Anton Zeilinger. Generation and confirmation of a (100 × 100)-dimensional entangled quantum system. *Proceedings of the National Academy of Sciences of the United States of America*, 111(17):6243–6247, 4 2014.

[180] Yongxiong Ren, Zhe Wang, Guodong Xie, Long Li, Yinwen Cao, Cong Liu, Peicheng Liao, Yan Yan, Nisar Ahmed, Zhe Zhao, et al. Free-space optical communications using orbital-angular-momentum multiplexing combined with mimo-based spatial multiplexing. *Optics letters*, 40(18):4210–4213, 2015.

[181] Unaiza Tariq, Hiva Shahoei, Guang Yang, and Duncan L MacFarlane. Orbital angular momentum orthogonality based crosstalk reduction. *Progress In Electromagnetics Research Letters*, 98:17–25, 2021.

[182] Donghui Shen, Tong He, Xianbin Yu, and Daomu Zhao. Mode Conversion and Transfer of Orbital Angular Momentum between Hermite-Gaussian and Laguerre-Gaussian Beams. *IEEE Photonics Journal*, 14(1), 2 2022.

[183] Guo Liang and Qing Wang. Controllable conversion between Hermite Gaussian and Laguerre Gaussian modes due to cross phase. *Optics Express*, 27(8):10684, 4 2019.

[184] Nicolas K Fontaine, Roland Ryf, Haoshuo Chen, David T Neilson, Kwangwoong Kim, and Joel Carpenter. Laguerre-gaussian mode sorter. *Nature communications*, 10(1):1–7, 2019.

[185] Yiyu Zhou, Jiapeng Zhao, Zhimin Shi, Seyed Mohammad Hashemi Rafsanjani, Mohammad Mirhosseini, Ziyi Zhu, Alan E Willner, and Robert W Boyd. Hermite–gaussian mode sorter. *Optics letters*, 43(21):5263–5266, 2018.

[186] Marco W Beijersbergen, Les Allen, HELO Van der Veen, and JP Woerdman. Astigmatic laser mode converters and transfer of orbital angular momentum. *Optics Communications*, 96(1-3):123–132, 1993.

[187] Alison M Yao and Miles J Padgett. Orbital angular momentum: origins, behavior and applications. *Advances in optics and photonics*, 3(2):161–204, 2011.

[188] Onur Danaci, Christian Rios, and Ryan T. Glasser. All-optical mode conversion via spatially multimode four-wave mixing. *New Journal of Physics*, 18(7):073032, 7 2016.

[189] Song Nie, Song Yu, Shanyong Cai, Mingying Lan, and Wanyi Gu. Multichannel mode conversion and multiplexing based on a single spatial light modulator for optical communication. *https://doi.org/10.1117/1.OE.55.7.076108*, 55(7):076108, 7 2016.

[190] Wei Guan Shen, Yuan Chen, Hui Ming Wang, and Xian Min Jin. OAM mode conversion in a photonic chip. *Optics Communications*, 507:127615, 3 2022.

[191] D. G. Pires, J. C.A. Rocha, A. J. Jesus-Silva, and E. J.S. Fonseca. Optical mode conversion through nonlinear two-wave mixing. *Physical Review A*, 100(4):043819, 10 2019.

[192] Raymond C Cumming. The serrodyne frequency translator. *Proceedings of the IRE*, 45(2):175–186, 1957.

[193] Bruno Piccirillo, Ebrahim Karimi, Enrico Santamato, and Lorenzo Marrucci. Light propagation in a birefringent plate with topological charge. *Optics Letters, Vol. 34, Issue 8, pp. 1225-1227*, 34(8):1225–1227, 4 2009.

[194] Bruno Piccirillo, Ebrahim Karimi, Enrico Santamato, Lorenzo Marrucci, and Sergei Slussarenko. Efficient generation and control of different-order orbital angular momentum states for communication links. *JOSA A, Vol. 28, Issue 1, pp. 61-65*, 28(1):61–65, 1 2011.

[195] Ebrahim Karimi, Bruno Piccirillo, Eleonora Nagali, Lorenzo Marrucci, and Enrico Santamato. Efficient generation and sorting of orbital angular momentum eigenmodes of light by thermally tuned q-plates. *Applied Physics Letters*, 94(23):231124, 6 2009.

[196] Sergei Slussarenko, Bruno Piccirillo, Vladimir Chigrinov, Lorenzo Marrucci, and Enrico Santamato. Liquid crystal spatial-mode converters for the orbital angular momentum of light. *Journal of Optics*, 15(2):025406, 2013.

[197] Ebrahim Karimi, Bruno Piccirillo, Lorenzo Marrucci, and Enrico Santamato. Light propagation in a birefringent plate with topological charge. *Optics letters*, 34(8):1225–1227, 2009.

[198] Dunzhao Wei, Yue Cheng, Rui Ni, Yong Zhang, Xiaopeng Hu, Shining Zhu, and Min Xiao. Generating controllable laguerre-gaussian laser modes through intracavity spin-orbital angular momentum conversion of light. *Physical Review Applied*, 11(1):014038, 2019.

[199] Kohki Nakagawa, Keisaku Yamane, Ryuji Morita, and Yasunori Toda. Laguerre–Gaussian vortex mode generation from astigmatic semiconductor microcavity. *Applied Physics Express*, 13(4):042001, 3 2020.

[200] Mark Stone, Aziza Suleymanzade, Lavanya Taneja, David I Schuster, and Jonathan Simon. Optical mode conversion in coupled fabry–perot resonators. *Optics Letters*, 46(1):21–24, 2021.

[201] Jesse Lu and Jelena Vučković. Nanophotonic computational design. *Optics express*, 21(11):13351–13367, 2013.

[202] Chenlei Li, Dajian Liu, and Daoxin Dai. Multimode silicon photonics. *Nanophotonics*, 8(2):227–247, 2 2018.

[203] Hongwei Wang, Yong Zhang, Yu He, Qingming Zhu, Lu Sun, Yikai Su, H Wang, Y Zhang, Y He, Q Zhu, L Sun, and Y Su. Compact Silicon Waveguide Mode Converter Employing Dielectric Metasurface Structure. *Advanced Optical Materials*, 7(4):1801191, 2 2019.

[204] Alina Karabchevsky and Yakov Greenberg. Spatial eigenmodes conversion with metasurfaces engraved in silicon ridge waveguides. *Applied Optics, Vol. 58, Issue 22, pp. F21-F25*, 58(22):F21–F25, 8 2019.

[205] Muhammad Wajih, Ullah Siddiqi, Cheng Tu, Joshua E-Y Lee, Chenxi Zhu, Yin Xu, Yue Dong, Bo Zhang, and Yi Ni. A compact silicon-based TM0-to-TM2 mode-order converter using shallowly-etched slots. *Journal of Optics*, 22(1):015802, 12 2019.

[206] Hongwei Wang, Jinlong Xiang, Kangnian Wang, Xuhan Guo, Yaotian Zhao, Yikai Su, and Yong Zhang. Ultra-compact silicon mode-order converters based on dielectric slots. *Optics Letters, Vol. 45, Issue 13, pp. 3797-3800*, 45(13):3797–3800, 7 2020.

[207] Bo Zhang, Chenxi Zhu, Xin Hu, Yi Ni, Yin Xu, and Yue Dong. On-chip silicon shallowly etched TM0-to-TM1 mode-order converter with high conversion efficiency and low modal crosstalk. *JOSA B, Vol. 37, Issue 5, pp. 1290-1297*, 37(5):1290–1297, 5 2020.

[208] Chenxi Zhu, Yin Xu, Zhe Kang, Xin Hu, Yue Dong, Bo Zhang, Yi Ni, and Peipeng Xu. Silicon-Based TM0-to-TM3 Mode-Order Converter Using On-Chip Shallowly Etched Slot Metasurface. *Photonics 2021, Vol. 8, Page 95*, 8(4):95, 3 2021.

[209] David A. B. Miller, Shanhui Fan, and Victor Liu. Ultra-compact photonic crystal waveguide spatial mode converter and its connection to the optical diode effect. *Optics Express, Vol. 20, Issue 27, pp. 28388-28397*, 20(27):28388–28397, 12 2012.

[210] Yingyan Huang, Guoyang Xu, and Seng Tiong Ho. An ultracompact optical mode order converter. *IEEE Photonics Technology Letters*, 18(21):2281–2283, 11 2006.

[211] Daoxin Dai, Yongbo Tang, John E Bowers, Y Shani, C Henry, R Kistler, K Orlowsky, and D Ackerman. Mode conversion in tapered submicron silicon ridge optical waveguides. *Optics Express, Vol. 20, Issue 12, pp. 13425-13439*, 20(12):13425–13439, 6 2012.

[212] Daoxin Dai, Jian Wang, and Sailing He. Silicon multimode photonic integrated devices for on-chip mode-division-multiplexed optical interconnects (invited review). *Progress In Electromagnetics Research*, 143:773–819, 2013.

[213] Lars H Frandsen, Yuriy Elesin, Louise F Frellsen, Miranda Mitrovic, Yunhong Ding, Ole Sigmund, Kresten Yvind, Y Ding, J Xu, F Da Ros, B Huang, H Ou, and C Peucheret. Topology optimized mode conversion in a photonic crystal waveguide fabricated in silicon-on-insulator material. *Optics Express, Vol. 22, Issue 7, pp. 8525-8532*, 22(7):8525–8532, 4 2014.

[214] Gang Chen and Jin U. Kang. Waveguide mode converter based on two-dimensional photonic crystals. *Optics Letters, Vol. 30, Issue 13, pp. 1656-1658*, 30(13):1656–1658, 7 2005.

[215] Nathan Schine, Albert Ryou, Andrey Gromov, Ariel Sommer, and Jonathan Simon. Synthetic Landau levels for photons. *Nature*, 534(7609):671–675, 2016.

[216] H Jeff Kimble. The quantum internet. *Nature*, 453(7198):1023–1030, 2008.

[217] Peter A. Ivanov, Fabian Letscher, Jonathan Simon, and Michael Fleischhauer. Adiabatic flux insertion and growing of Laughlin states of cavity Rydberg polaritons. *Physical Review A*, 98(1):013847, 7 2018.

APPENDIX A

SUPPLEMENT: PHOTONIC MODE CONVERSION

A.1 Experiment

A.1.1 Experimental setup

The main ingredients used in the work of Chapter 6 are the twisted cavity, atomic sample, 780 nm probe beam, and 1529 nm modulation beam. Probe photons were converted between eigenmodes of the twisted cavity via passage through the sample of atoms, whose energy levels were spatiotemporally modulated to create a spatiotemporally-varying optical susceptibilty akin to sculpting a phase plate out of the atomic sample.

The twisted cavity used in the work of Chapter 6 is the same as that described in [44] and [46]. The eigenmodes of this cavity are non-degenerate Laguerre-Gaussian (LG) modes at the lower cavity waist which coincides with the position of the atomic sample. In reality, paraxial astigmatism distort the LG modes at other positions along the cavity axis [47]. Thus, in order to incouple to the $l = 3$ eigenmode at the location of the atoms, 780 nm probe light is injected in the Ince-Gaussian spatial mode profile depicted in Figure A.1. The transverse mode spacing between every third orbital angular momentum mode ($l = 0, 3, 6...$) is about 65 MHz with slight variation depending on the choice of free spectral range. The free spectral range is 2.5 GHz. The four cavity mirrors were coated and supplied by LAYERTEC GmbH. As these mirrors are sufficiently reflective at both 780 nm and 1529 nm, cavity modes exist for both the probe and modulation beams where further specifications are listed in Table A.1. The lower waist size at 1529 nm is related to the lower waist size at 780 nm by a factor of $\sqrt{1529/780}$.

The work of Chapter 6 requires probe light to be coupled into the $l = 3$ cavity mode and modulation light to be coupled into both the $l = 0$ and $l = 3$ cavity modes. Due to the aforementioned astigmatism, we inject probe photons with an Ince-Gaussian spatial profile

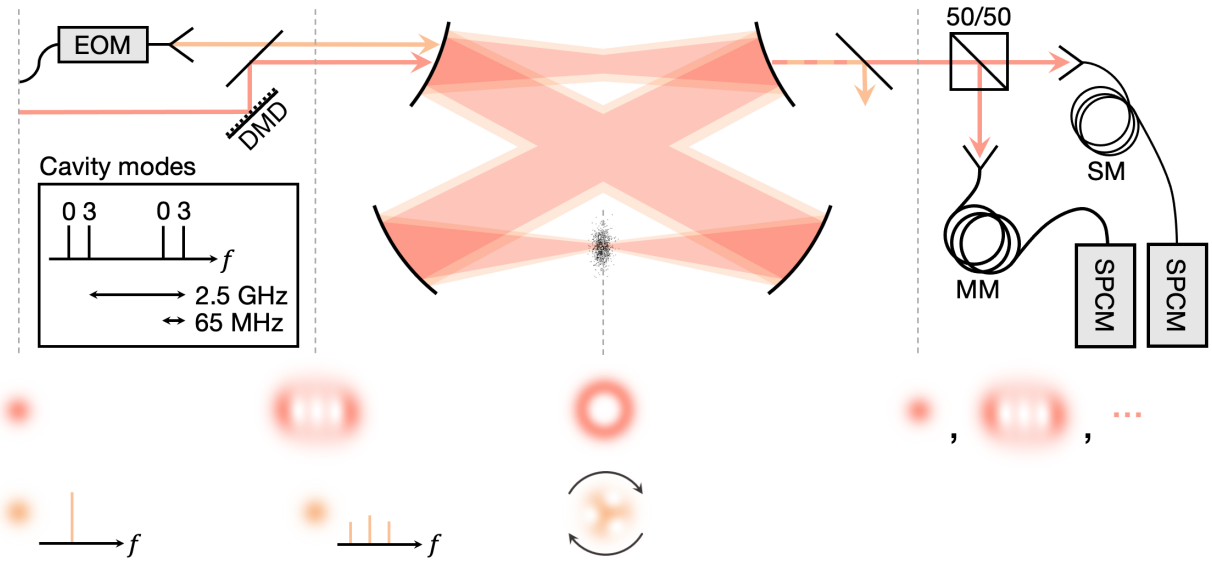

Figure A.1: **Beam preparation and measurement.** From left to right, this figure depicts the preparation of 780 nm (red) and 1529 nm light (orange) for injection into the twisted cavity, the 780 nm and 1529 nm cavity modes at the lower cavity waist, and the detection of the transmitted 780 nm light. The 780 nm light begins as a Gaussian beam which is shaped into an Ince-Gaussian mode by a digital micromirror device (DMD). Due to paraxial astigmatism, this mode evolves into an $l = 3$ LG mode at the lower cavity waist due where it couples to the atomic sample. Light eventually leaks out of the cavity and passes through a 50/50 non-polarizing beamsplitter cube, splitting the light between two paths: one through a multi-mode (MM) fiber, and one through a single mode (SM) fiber. Each fiber terminates at a single-photon counting module (SPCM). The SM path is used to detect only $l = 0$ cavity photons, whereas the MM path detects all cavity photons. The 1529 nm light also begins as a Gaussian beam. It passes through an electro-optic modulator (EOM), acquiring frequency sidebands at the frequency difference between the $l = 0$ and $l = 3$ modes (65 MHz). This light is then injected slightly off-center from the cavity axis which spatially couples the incident 1529 nm light to a forest of modes, but $l = 0$ and $l = 3$ are isolated by frequency discrimination. The superposed $l = 0$ and $l = 3$ modes form a rotating, three-holed profile at the lower cavity waist that spatiotemporally modulates the atomic sample. The 1529 nm light eventually leaks out of the cavity as well and is filtered out from the detection path.

Table A.1: **Dual-wavelength cavity specifications**.

	780 nm	1529 nm
Lower waist size	19 μm	27 μm
Top 2x mirrors	99.91%	99.82%
Bottom 2x mirrors	>99.9% (HR)	99.94%
Finesse $\mathcal{F}$	1900	1310

corresponding with $l = 3$ at the lower cavity waist. This profile is acquired by using a digital micromirror device (DMD) to shape a preliminary probe beam as depicted in Figure A.1. We use an electro-optic modulator (EOM) to inject a frequency-modulated $l = 0$ modulation beam off-center from the cavity axis to couple to the $l = 0$ and $l = 3$ cavity modes. While the off-center injection of an $l = 0$ transverse mode has spatial overlap with many other transverse modes, we couple only to the $l = 0$ and $l = 3$ cavity modes by frequency discrimination. Off-center injection is not particularly efficient, but this inefficiency was compensated by the large amount of 1529 nm power we had at our disposal (> 1 W).

In order to have simultaneous injection of the $l = 3$, 780 nm mode and $l = 0$ and $l = 3$, 1529 nm modes, we tune the lockpoint frequency of the 1529 nm laser and the cavity length using a piezoelectric actuator. We first tune the cavity length to transmit the $l = 3$, 780 nm mode, then change the lockpoint frequency of the 1529 nm laser such that the carrier and one sideband generated by the EOM are resonant with the $l = 0$ and $l = 3$ modes. The modulation depth of the EOM is controlled by a variable attenuator to sweep the relative $l = 0$ to $l = 3$ power. For given values of the collective cooperativity and cavity-atom detuning, we optimize $\mathcal{E}_{3\to0}$ through iterative fine-tuning scans of the 1529 nm lockpoint frequency, EOM modulation frequency, and EOM modulation depth.

In the work of Chapter 6, the $l = 3$, 780 nm probe beam is 130 MHz detuned from the $5S_{1/2} \leftrightarrow 5P_{3/2}$ transition (see Section A.1A.1.6) and the 1529 nm modulation beam is about 14 GHz detuned from the $5P_{3/2} \leftrightarrow 4D_{5/2}$ transition. This 14 GHz detuning was selected for several reasons. First, the $5P_{3/2} \leftrightarrow 4D_{3/2}$ transition is only 13.4 GHz higher than the

$5P_{3/2} \leftrightarrow 4D_{5/2}$ transition. We utilize only circular polarization for the probe and modulation beams in this work, isolating only the stretched states of $\left|5S_{1/2}, F = 2\right\rangle$, $\left|5P_{3/2}, F = 3\right\rangle$, and $\left|4D_{5/2}, F = 4\right\rangle$ assuming perfect polarization and optical pumping. In the event of imperfection, the relatively large detuning of 14 GHz + 13.4 GHz from the $5P_{3/2} \leftrightarrow 4D_{3/2}$ transition suppresses mixing of the $4D_{3/2}$ state that could potentially complicate the mode conversion process. Second, $\Omega/(2\pi) \ll$14 GHz for all Ω used in this work. This condition simplifies the intuition and calculations behind the mode conversion process: for Ω much less than the detuning from the $5P_{3/2} \leftrightarrow 4D_{5/2}$ transition, the $4D_{5/2}$ state remains essentially unpopulated. Thus, the modulation beam can be thought to virtually excite the $4D_{5/2}$ state to convert $l = 3$ probe photons to $l = 0$. In calculations, the $4D_{5/2}$ state can be adiabatically eliminated, reducing the coupling to the $4D_{5/2}$ state to effective couplings in the Hamiltonian (see Section A.2A.2.2). Third, 14 GHz was convenient given our available frequency sources and high power at 1529 nm.

The peak cavity-atom coupling between a single ^{87}Rb atom and $l = 0$ mode at 780 nm is the same as that in [44]: $g_{\text{single}} = 2\pi \times 0.58$ MHz. Given this information, it is possible to estimate the number of atoms from the dispersive shift of the twisted cavity transmission feature in spectra measurements for an unmodulated atomic sample. This shift depends on Ng^2_{single} where N is the atom number. In this work, we estimate an atom number of 500 for measurements with the lowest atom number ($N\eta = 70$) and 3500 for measurements with the highest atom number ($N\eta = 560$). $N\eta$ is equivalent to $4Ng^2_{\text{single}}/\kappa\Gamma$ where $\kappa = 2\pi \times 1.6$ MHz (the cavity linewidth at 780 nm) and $\Gamma = 2\pi \times 6$ MHz (the linewdith of the $5P_{3/2}$ state).

While the majority of the work of Chapter 6 focused exclusively on $l = 3 \rightarrow 0$ conversion, we briefly examined $l = 0 \rightarrow 3$ conversion. For identical parameters that yielded $l = 3 \rightarrow 0$ conversion near $\mathcal{E}_{3\rightarrow 0}$=1, we observed $l = 0 \rightarrow 3$ conversion near $\mathcal{E}_{3\rightarrow 0}$=0.5. While this behavior has yet to be understood, it may arise from the unequal detunings of the $l = 0$ and

$l = 3$ modes to the $5P_{3/2}$ state. In early exploratory measurements of this work, we also observed polarization conversion between two $l = 0$ polarization modes of the twisted cavity under a slightly different atomic modulation scheme. Instead of modulating the atoms with the $l = 0$ and $l = 3$ 1529 nm modes separated by the transverse mode splitting frequency, we modulated the atoms with the two $l = 0$ 1529 nm polarization modes separated by the polarization mode splitting frequency. The polarization conversion efficiency was not rigorously quantified, but polarization conversion is mentioned here to demonstrate proof of concept.

A.1.2 Calibration of $\mathcal{E}_{3\to0}$

As illustrated in Figure A.1, the output of the cavity is split into two paths by a 50/50 beamsplitter: one leading to a multimode fiber, and one leading to a single mode fiber. The single mode path collects only $l = 0$ light by filtering out higher order modes and the multimode path collects $l = 0$, $l = 3$, and any other modes which may be present (see Section A.1A.1.4 for why we do not see other modes). The ends of each fiber connect to separate single photon counting modules (SPCMs). Data for each SPCM is collected simultaneously, after which scale factors are applied in post-processing to account for the nonlinearity of the SPCMs and count rate imbalance due to mismatched fiber incoupling efficiencies. To acquire $\mathcal{E}_{3\to0}$, the internal conversion efficiency from $l = 3$ to $l = 0$, the post-processed $l = 0$ count rate is normalized to the post-processed $l = 3$ bare cavity count rate then scaled up by a factor of 4. This factor of 4 arises from the double-ended nature of our cavity, meaning light can leak out one of two mirrors of the cavity (see Section A.1A.1.5). In reality, the cavity is comprised of four mirrors, but two of the mirrors are high reflectors at 780 nm and so we do not consider these as significant leakage ports.

In a two-mirror cavity whose mirrors are lossless and equal reflectance, the $l = 3$ bare cavity output power is equivalent to the input power assuming perfect spatial incoupling to

the cavity. However, our cavity mirrors induce loss as a result of scattering, absorption, and imperfections on the mirror surface such as dust. An estimate of the loss can be derived from the measured finesse and mirror reflectance. The finesse of a two-mirror cavity comprised of identical mirrors with low-loss A and transmissivity T is $2\pi/(2A + 2T)$. Given the finesse and reflectance specifications at 780 nm as listed in Table A.1, we expect the loss per mirror to be about 750 ppm, which corresponds to a maximum $l = 3$ bare cavity output power of $(1 + A/T)^{-2} = 30\%$ of the input power. Thus, the external, or end-to-end, efficiency for $l = 3$ to $l = 0$ conversion is realistically $\mathcal{E}_{3\to0} \times \frac{1}{4} \times 30\% = 7.5\%$ at maximum. This calculation ignores imperfect cavity incoupling which can be corrected for externally with mode-matching optics. However, $\frac{1}{4} \to 1$ in single-ended cavities and $30\% \to\sim 100\%$ for low loss mirrors, leaving significant room to increase the external conversion efficiency to near-100% in hypothetical future variants of the method presented in this paper.

A.1.3 Definition of Ω

The 1529 nm modulation beam is comprised of an $l = 0$ component and an $l = 3$ component. In the work of Chapter 6, we use Ω to denote the Rabi frequency of the $l = 3$ component which has a direct proportionality to the $l = 0$ Rabi frequency. The numerical value of Ω is estimated through measurement of the cavity line shift in the dispersive regime due to the AC Stark shift provided by a 1529 nm $l = 0$ only. Scale factors are applied to account for differences in the $l = 0$ and $l = 3$ cavity incoupling efficiencies, spectral redistribution given by the EOM depicted in Figure A.1, and nonlinearity of the acousto-optic modulator used to control the modulation beam intensity. We estimate the $l = 3$ Rabi frequency is about 1.7 times higher than the $l = 0$ Rabi frequency. At maximum $\Omega/(2\pi)$ of 3.5 GHz, we estimate the total incoupled power is on the order of 1 mW which is then cavity enhanced by a factor of $\mathcal{F}_{1529}/\pi = 420$ where $\mathcal{F}_{1529}$ is the cavity finesse at 1529 nm.

A.1.4 Confirmation of an $l = 0$ converted output

We detect converted photons that have a Gaussian spatial profile and frequency equivalent to that of the bare cavity $l = 0$ eigenmode, thus verifying that light is indeed converted to $l = 0$. The lower left corner of Figure A.2 depicts an image of the cavity output which has been averaged over 200 experimental runs and decomposed into its $l = 0$ and $l = 3$ constituents for the maximum values of Ω and $N\eta$ used in the work of Chapter 6 ($\Omega/(2\pi) = 3.5$ GHz and $N\eta = 560$). Note that these images were captured for a singular, fixed probe frequency and the image for $l = 3$ does not appear LG. While this mode is LG at the location of the atomic sample, it emerges Ince-Gaussian due to astigmatism in the cavity (see [47] and Supplement of [44]). In order to decompose the image of the cavity output into its $l = 0$ and $l = 3$ constituents, a bare cavity $l = 3$ image was captured, scaled, then subtracted from the cavity output image. Sums were calculated for the cavity output and the bare cavity $l = 3$ images over the same small patch centered on the leftmost lobe in each image; the bare cavity $l = 3$ image was scaled by the ratio of these sums. The subtraction of the scaled bare cavity $l = 3$ image reveals a Gaussian profile expected of the $l = 0$ mode. Note that higher order cavity eigenmodes, such as $l = 6$ and those with radial nodes, are not observed in imaging. As the modulation beam plausibly induces additional couplings to these modes, we suspect they may be suppressed as a result of their higher detuning from the $5S_{1/2} \rightarrow 5P_{3/2}$ transition. We observed nonzero $l = 3$ output due to impedance matching considerations as detailed in A.1A.1.5, and quantitative comparison in imaging further supports conversion from $l = 3$ to $l = 0$ near $\mathcal{E}_{3\rightarrow 0} = 1$.

Figure A.2 also depicts the dependence of the $l = 0$ and $l = 3$ output frequencies on the modulation frequency for a singular, fixed probe frequency. To measure the frequencies of the $l = 0$ and $l = 3$ constituents, the twisted cavity output is sent through a 2-mirror filter cavity whose length is controllably scanned using a piezoelectric actuator and side-of-fringe lock to an additional laser. This 2-mirror cavity acts as a frequency ruler that could

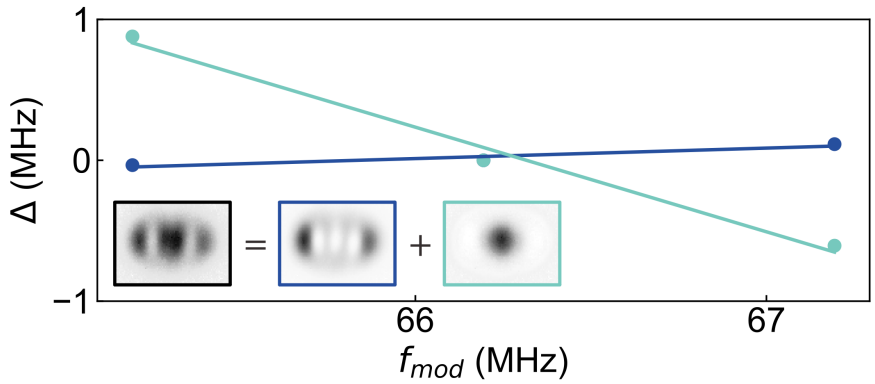

Figure A.2: **Spatial and frequency analysis of the cavity output.** Imaging the total cavity output (black) reveals both unconverted $l = 3$ light (blue) and converted $l = 0$ light (teal) with conversion efficiency numbers comparable to that of our spectra data. Here, Δ is the frequency difference between the output $l = 3(0)$ mode and the bare cavity $l = 3(0)$ mode. Both $l = 3$ and $l = 0$ light appear at their bare cavity mode frequencies for an atomic modulation frequency, f_{mod}, equal to the transverse mode splitting. If f_{mod} is varied slightly, we observe the $l = 0$ frequency vary similarly while the $l = 3$ frequency remains largely unchanged. Few values of f_{mod} were considered here as this data was collected primarily to confirm the frequencies of the $l = 3$ and $l = 0$ outputs, and variation of f_{mod} past the scale of the cavity linewidth results in very little conversion as light barely enters the cavity.

spatially discriminate between modes. For varying 1529 nm modulation frequencies (f_{mod}), we measured the frequency differences (Δ) of the converted $l = 0$ and unconverted $l = 3$ outputs relative to each of their bare twisted cavity frequencies. Not only did we observe the converted $l = 0$ and unconverted $l = 3$ to be equal to their bare twisted cavity frequencies for f_{mod} equal to the transverse mode splitting (near 66 MHz for this choice of twisted cavity free spectral range), but we observed the influence of the 1529 nm modulation on the frequency of the converted $l = 0$ output. The converted $l = 0$ output frequency changed near-linearly with f_{mod} within about one twisted cavity linewidth at 1529 nm. Measurements were not collected beyond one twisted cavity linewidth, as the conversion efficiency drops significantly here due to insufficient 1529 nm power entering the cavity resulting in poor modulation of the atomic sample.

A.1.5 Impedance matching

Reference [200] and its appendix are excellent examples of how cavity impedance matching affects the transmission and conversion of cavity modes. Here, we will follow a similar formalism to illustrate why the external conversion efficiency is limited to 25% in a double-ended cavity and how extension to a single-ended cavity should enable an external conversion efficiency of 100% for lossless cavity mirrors.

Figure A.3 depicts a reinterpreted layout of the four-mirror twisted cavity. As two of the four mirrors are highly reflective (HR), the twisted cavity is effectively reduced to a two-mirror cavity. As the cavity hosts two coupled eigenmodes in the context of this work, we can model the coupled eigenmodes as two coupled two-mirror cavities where each cavity hosts an eigenmode and the left (right) mirror reflection coefficient is the same as the bottom (top) mirror reflection coefficient r_1 (r_2). The coupling element is the modulated atomic sample which can be modeled as some partially-reflective optic that obeys the beam splitter relations and has reflection coefficient r. Assuming lossless mirrors, $r = \sqrt{1-t^2}$, $r_1 = \sqrt{1-t_1^2}$, and $r_2 = \sqrt{1-t_2^2}$ where t, t_1, and t_2 are the corresponding transmission coefficients. We now solve the following system of equations to ultimately calculate the $l = 3$ and $l = 0$ transmissions plotted in Figures A.3b and A.3c:

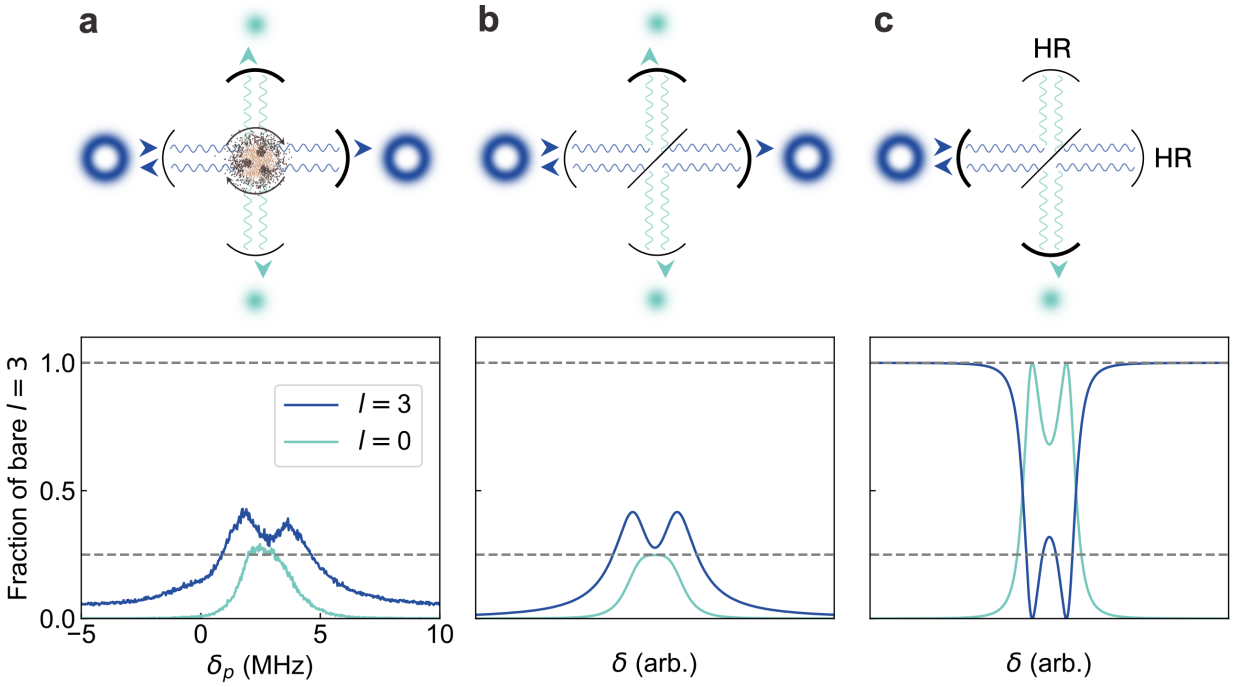

Figure A.3: **Cavity impedance matching and conversion efficiency.** This figure depicts a reinterpreted layout of the twisted cavity and its corresponding transmission spectra. Light can leak out only two of the four cavity mirrors, rendering our cavity double-ended. This work describes two cavity modes that are coupled by a modulated atomic sample, which is modeled here as two crossed, identical cavities that each host one of the spatial modes and are coupled by a coupling element. The cavities need not be visualized as crossed, but they are here for visibility and ease of considering the beam splitter relations of the coupling element. The plots of **a**, **b**, and **c** depict experimental transmissions for the highest values of Ω and $N\eta$ used in this work, simulated transmissions for a double-ended cavity (akin to the cavity used in this work), and simulated transmissions for a single-ended cavity, respectively. Transmission for $l = 3$ was acquired by subtracting the SM signal from the MM signal, including appropriate scale factors to account for coupling efficiency differences and the nonlinearity of the SPCMs (see Fig. A.1). The background level of the $l = 3$ transmission is higher than that of $l = 0$ transmission as the MM fiber lets in more ambient light. The shapes and numerical values of the transmission curves in **a** and **b** are directly comparable. The shapes are a result from the coupling between modes, where coupled modes 'split' in general, and the numerical values are a result of the double-ended nature of the cavity. If we increase the reflectivity of the coupling element in **b**, both modes 'split' further in the spectra, but the $l = 0$ transmission never exceeds 25%. **c**, If we replace one of the cavity mirrors with a high reflector while all other parameters remain constant, we alter the cavity from double-ended to single-ended and the maximum external efficiency increases from 25% to 100%.

$$
\begin{aligned}
\mathrm{E_{1AR}} &= (\mathrm{E_{1AL}}r_1 + \mathrm{E_{0A}}t_1)e^{i\delta} \\
\mathrm{E_{1AL}} &= (\mathrm{E_{2BL}}r + \mathrm{E_{2AL}}t)e^{i\delta} \\
\mathrm{E_{2AR}} &= (-\mathrm{E_{1BR}}r + \mathrm{E_{1AR}}t)e^{i\delta} \\
\mathrm{E_{2AL}} &= -\mathrm{E_{2AR}}r_2 e^{i\delta} \\
\mathrm{E_{1BR}} &= -\mathrm{E_{1BL}}r_1 e^{i\delta} \\
\mathrm{E_{1BL}} &= (-\mathrm{E_{2AL}}r + \mathrm{E_{2BL}}t)e^{i\delta} \\
\mathrm{E_{2BR}} &= (\mathrm{E_{1AR}}r + \mathrm{E_{1BR}}t)e^{i\delta} \\
\mathrm{E_{2BL}} &= \mathrm{E_{2BR}}r_2 e^{i\delta}
\end{aligned}
\tag{A.1}
$$

These eight equations describe the two counter-propagating intracavity fields in each of subsection of the cavity model formed between the coupling element and a mirror. The notation E_{ijk} denotes the field in subsection $i \in (1, 2)$ for mode $j \in (\mathrm{A}, \mathrm{B})$ of propagating direction $k \in (\mathrm{L}, \mathrm{R})$. In this work, mode A corresponds with $l = 3$ and mode B corresponds with $l = 0$. $\mathrm{E_{0A}}$ is the input field. The parameter δ is a phase factors accrued by propagation: $\delta = \mathrm{kL}$ where L is the length of each cavity subsection (which we assume to be equal) and k is the wavenumber. If we vary δ, we essentially varying the frequency of the imaginary laser probing this model cavity system. The transmitted fields are related to the intracavity fields by the transmission coefficient of the mirror through which one wishes to calculate transmission. The mirror through which we calculate the transmitted field is depicted in bold in Figure A.3 with the corresponding intensity plotted below as a function of δ. The calculated intensities are normalized to the input intensity.

For $r_1 = r_2 = \sqrt{0.9991}$ (the reflection coefficient of our top 2x cavity mirrors as listed in Table A.1) and increasing r, the $l = 0$ transmission increases from zero and saturates to 25%. For $r \sim 0.001$, the calculated $l = 0$ and $l = 3$ transmission in Figure A.3b mimics

the measured $l = 0$ and $l = 3$ transmission in Figure A.3a. In fact, the non-Lorentzian line shape of the $l = 0$ mode is a result of the $l = 0$ and $l = 3$ coupling. Increasing r couples the $l = 0$ and $l = 3$ more strongly, resulting in a vacuum Rabi-like splitting in both the $l = 0$ and $l = 3$ spectra. Thus, the non-Lorentzian line shape of $l = 0$ is indicative of nonzero $l = 0$ and $l = 3$ coupling, but not enough to fully split the $l = 0$ mode in the spectra.

For $r_1 = \sqrt{0.9991}, r_2 = 1$, and the same r as in Figure A.3b, the $l = 0$ mode is fully transmitted at 100% as depicted in Figure A.3c. This change in r_2 is equivalent to making our double-ended cavity into single-ended cavity, where light can leak out of only one cavity mirror. Thus, applying the method presented in this paper to a low loss, single-ended cavity holds promise for achieving mode conversion at an external efficiency near 100%.

A.1.6 $\mathcal{E}_{3\to0}$ versus cavity-atom detuning

In the work of Chapter 6, we operated in the dispersive regime, where the $l = 3$ cavity mode was 130 MHz detuned from the $5P_{3/2}$ state ($\Delta_{cav-atom} = 130$ MHz). For the maximum values of Ω and $N\eta$ used in this work ($\Omega/(2\pi) = 3.5$ GHz and $N\eta = 560$), we experimentally observed high $\mathcal{E}_{3\to0}$ around this detuning as illustrated in Figure A.4. For smaller and opposite sign detunings, we observed a substantial decrease in $\mathcal{E}_{3\to0}$. While the source of this decrease has not yet been identified, we hypothesize it might arise from loss due to couplings to other twisted cavity modes or hyperfine levels of the $5P_{3/2}$ state.

A.2 Theory

A.2.1 Laguerre-Gaussian modes

The normalized electric field for a Laguerre-Gaussian mode LG_{lp} at the lower cavity waist ω is,

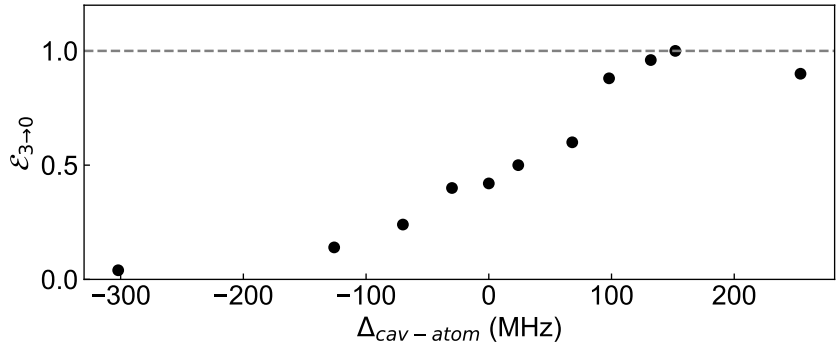

Figure A.4: **Maximum conversion efficiency versus cavity-atom detuning.** In this work, the $l = 3$ cavity mode was 130 MHz detuned from the $5S_{1/2} \to 5P_{3/2}$ atomic transition, where we experimentally observed the highest $\mathcal{E}_{3\to0}$. All data was collected for the highest values of Ω and $N\eta$ used in this work.

$$u_{lp}(r,\phi) = \frac{C_{lp}}{w}\left(\frac{r\sqrt{2}}{w}\right)^{|l|} L_p^{|l|}\left(\frac{2r^2}{w^2}\right) e^{-(r^2/w^2)} e^{-il\phi}$$

where r (ϕ) is the radial (azimuthal) coordinate. The mode index l describes the orbital angular momentum which manifests as a phase winding, whereas the mode index p describes the number of radial, intensity 'rings.' Both indices are integers with $p \geq 0$. $L_p^l(x)$ are the generalized Laguerre polynomials and the normalization constant $C_{lp} = \sqrt{\frac{2p!}{\pi(p+|l|)!}}$ to ensure $\langle u_{lp}|u_{lp}\rangle = 1$.

A.2.2 Modeling conversion

This section describes steps taken to model the conversion process in the work of Chapter 6. We write down the full, time-dependent Hamiltonian then consider a simplified version of this Hamiltonian to computationally simplify spectra simulations. While the simulated spectra lack quantitative agreement with the experimental data, likely because the simplified Hamiltonian considers only a limited state space compared to the full Hamiltonian, they qualitatively capture main features of the data and are discussed here for the interested reader. The full, time-dependent Hamiltonian for the system described in this work written

in the frame rotating with the 780 nm probe laser of frequency ω_ℓ is ($\hbar \equiv 1$),

$$\begin{aligned} H(t) = & \sum_{n}^{N_{cav}} (\omega_n - \omega_\ell - i\frac{\kappa}{2}) a_n^\dagger a_n \\ & + \sum_{m}^{N_{at}} (\omega_p - \omega_\ell - i\frac{\Gamma_p}{2}) p_m^\dagger p_m \\ & + \sum_{m}^{N_{at}} (\omega_d - \omega_\ell - i\frac{\Gamma_d}{2}) d_m^\dagger d_m \\ & + \sum_{n}^{N_{cav}} \sum_{m}^{N_{at}} (g_{mn} p_m^\dagger a_n + g_{mn}^* p_m a_n^\dagger) \\ & + \sum_{m}^{N_{at}} (\Omega_m(t) d_m^\dagger p_m + \Omega_m^*(t) d_m p_m^\dagger) \\ & + \Omega_\ell (a_3^\dagger + a_3) \end{aligned} \tag{A.2}$$

where ω_n is the energy of the n^{th} 780 nm cavity mode, ω_p is the energy of the $5P_{3/2}$ state, ω_d is the energy of the $4D_{5/2}$ state, κ is the cavity decay rate at 780 nm, Γ_p is the atomic decay rate of the $5P_{3/2}$ state, and Γ_d is the atomic decay rate of the $4D_{5/2}$ state. The operators a_n, p_m, and d_m annihilate a photon in the n^{th} 780 nm cavity mode, a P-state excitation for the m^{th} atom, and a D-state excitation for the m^{th} atom, respectively. The drive strength of the probe laser is represented by Ω_ℓ, which drives only the $l = 3$ cavity mode.

The coupling strength g_{mn}, which couples the P-state of the m^{th} atom and the n^{th} 780 nm cavity mode, can be expressed as

$$g_{mn} = g_n u^{780}_{n_l n_p}(r_m, \phi_m) \tag{A.3}$$

where g_n is the single atom-photon coupling strength of the n^{th} cavity mode and $u^{780}_{n_l n_p}(r_m, \phi_m)$ is the field of the n^{th} 780 nm cavity mode at the location of the m^{th} atom. The n^{th} 780 nm cavity mode has l index n_l and p index n_p.

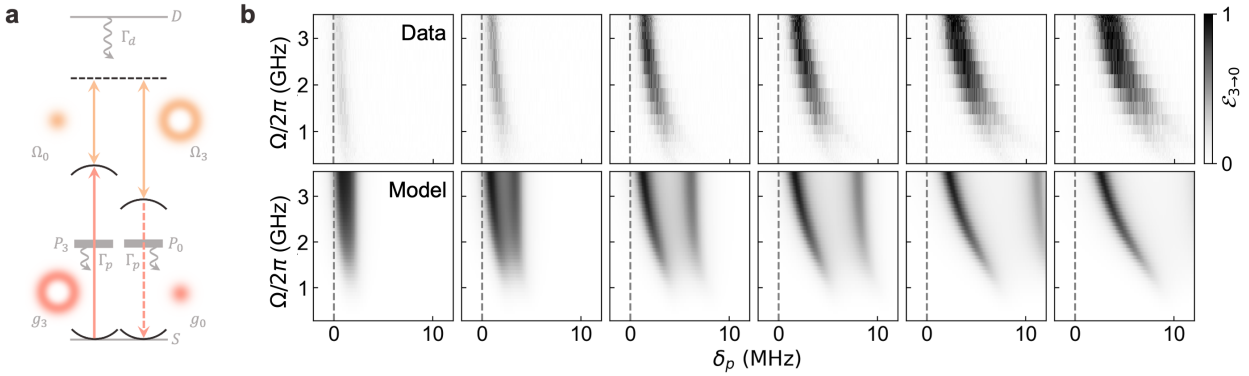

Figure A.5: **Spectra predictions of a simple model.** A simplified collective state model of the conversion process described in the work is depicted in **a**. The $l = 3$, 780 nm mode couples to the collective P_3 state with effective coupling g_3, the $l = 0$, 780 nm mode couples to the collective P_0 state with effective coupling g_0, and both collective P_3 and P_0 states couple to a collective D state with effective couplings Ω_3 and Ω_0, respectively. We solve for the expectation value of $a_0^\dagger a_0$, the transmission of the $l = 0$, 780 nm light, as a function of δ_p, Ω (the 1529 nm beam strength), and $N\eta$ using non-Hermitian perturbation theory where the drive term $\Omega_\ell(a_3 + a_3^\dagger)$ is the perturbation. The resulting, simulated spectra are plotted below the experimental spectra in **b**. All simulated parameters are identical to the experimental parameters, with the exception of $\Omega_3/\Omega_0 = 1.0$ instead of 1.7 as better agreement with the experimental data was observed. The simulated spectra has clear differences with the experimental spectra. Namely, the presence of an unobserved spectral feature and increased conversion at low $N\eta$. However, simulations at even lower $N\eta$ display an overall decrease in conversion akin to that in the data. Thus, we suspect this falloff in efficiency for lower $N\eta$ in simulations compared to experiment may be because this simple model excludes couplings to other collective states which act as loss channels. Despite the shortcomings of this model, it qualitatively predicts the saturation of $\mathcal{E}_{3\to0}$ to 1 for some minimum Ω and $N\eta$ and captures the shapes of the experimental spectra.

The time-dependent coupling strength $\Omega_m(t)$, which couples the D-state of the m^{th} atom and the P-state of the m^{th} atom, can be expressed as

$$\Omega_m(t) = \Omega_0 u_{00}^{1529}(r_m, \phi_m) \exp\left(i\omega_0^{1529} t\right) + \Omega_3 u_{30}^{1529}(r_m, \phi_m) \exp\left(i\omega_3^{1529} t\right) \tag{A.4}$$

where Ω_0 and Ω_3 are coupling strengths dependent on the field strength of the $l = 0$ component and $l = 3$ component of the 1529 nm beam, respectively. The frequencies of the $l = 0$ component and $l = 3$ component are ω_0^{1529} and ω_3^{1529}, respectively. Ordinarily, the time dependence of the Hamiltonian due to $\Omega_m(t)$ can be eliminated by a transformation, but here the presence of dual frequencies ω_0^{1529} and ω_3^{1529} prevents this elimination. Instead, the time dependence must be handled with Floquet theory or by solving for the time dynamics of the system. Additionally, coupling terms are often simplified by assuming uniformity of electric fields across the atomic sample, but here this idea does not apply. For many atoms, simulating this system with time- and space-dependent terms can by quite slow. An alternative approach to simplifying the massive state space for many atoms is to work in the collective state picture after adiabatic elimination of the $4D_{5/2}$ state, though this process comes with its own challenges such as determining the couplings between collective states and identifying which collective states are the most meaningful.

In light of these challenges, we considered a much simpler Hamiltonian to explore how well it could model the conversion spectra observed in the work of Chapter 6. Fig. A.5a depicts a modified level diagram described by the Hamiltonian,

$$
\begin{aligned}
H = &(\omega_3 - \omega_\ell - \frac{i\kappa}{2})a_3^\dagger a_3 + (\omega_0 - \omega_\ell - \delta_{03} - \frac{i\kappa}{2})a_0^\dagger a_0 \\
&+ (\omega_p - \omega_\ell - \frac{i\Gamma_p}{2})P_3^\dagger P_3 + (\omega_p - \omega_\ell - \delta_{03} - \frac{i\Gamma_p}{2})P_0^\dagger P_0 \\
&+ (\delta_{d3} - \omega_\ell - \frac{i\Gamma_d}{2})D^\dagger D \\
&+ g_0(a_0^\dagger P_0 + a_0 P_0^\dagger) + g_3(a_3^\dagger P_3 + a_3 P_3^\dagger) \\
&+ \frac{\Omega_0}{2}(D^\dagger P_0 + D P_0^\dagger) + \frac{\Omega_3}{2}(D^\dagger P_3 + D P_3^\dagger) \\
&+ \Omega_\ell(a_3 + a_3^\dagger)
\end{aligned}
\tag{A.5}
$$

which considers only $l = 0$ and $l = 3$ modes. Now, operators P_0, P_3, and D annihilate collective excitations instead of excitations of a single atom, and g_0, g_3, Ω_0, and Ω_3 are effective couplings to collective states. The collective states corresponding with the P_0 and P_3 operators adopt the orthogonality properties of the LG modes and are each coupled through one of the 1529 nm pathways to a collective D state. Detunings δ_{03} and δ_{d3} are the frequency differences $\omega_0 - \omega_3$ and $\omega_d - \omega_\ell^{1529}$, respectively, where ω_ℓ^{1529} is the frequency of the $l = 3$ component of the 1529 nm beam.

While this model falls short of quantitative agreement with the experimental data and predicts unobserved spectral features, it depicts the saturation of $\mathcal{E}_{3\to0}$ to 1 for some minimum threshold of Ω and $N\eta$ and captures the shapes of the experimental spectra (Fig. A.5b). Additional work is necessary to attain a better understanding of the minimum Ω and $N\eta$ needed to maximize the conversion efficiency and the conditions needed to suppress couplings to non-target LG modes, but the qualitative similarities between the modeled and experimental data provide some reassurance that the picture depicted in Fig. A.5a is a step in the right direction.